

# **Doping and its effect on ZnO properties**

**Tang Jie**

*(B.Eng.(Hons.), NUS)*

**A THESIS SUBMITTED**

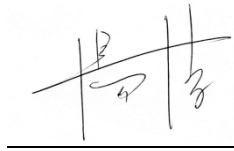
**FOR THE DEGREE OF DOCTOR OF PHILOSOPHY  
DEPARTMENT OF ELECTRICAL AND COMPUTER  
ENGINEERING  
NATIONAL UNIVERSITY OF SINGAPORE**

**2014**

## DECLARATION

I hereby declare that this thesis is my original work and it has  
been written by me in its entirety. I have duly  
acknowledged all the sources of information which have  
been used in the thesis.

This thesis has also not been submitted for any degree in any  
university previously.

A handwritten signature in black ink, consisting of stylized Chinese characters, positioned above a horizontal line.

Tang Jie  
30 September 2014

## Acknowledgements

It would not have been possible to complete this dissertation without the great help and support from the people around me.

First and foremost, my deepest gratitude and appreciation to my supervisor, Prof. Chua Soo Jin for his great guidance and cultivation from my undergraduate research opportunity program, final year project to this PhD work for the past six years. He not only supervises me to do excellent research, but also demonstrates to me how to live a balance life and the attitude is the key to success. He encourages me to achieve a little success every day and keep the momentum to achieve the final goal. His meticulousness, patience, enthusiasm and encouragement would inspire me all lifelong.

I would like to express my special gratitude to my senior Dr. Tay Chuan Beng for his guidance and suggestions to my research since the first day of my PhD life. He passed me his valuable experience on aqueous solution growth of ZnO for both experimental skills and theoretical knowledge without reservation. Special thanks also go to my seniors who are also my collaborators Dr. Deng Liyuan and Dr. Nguyen Xuan Sang for their valuable advices and help. Without their help, this work could not be done.

I would like to take this opportunity to thank the research staff from IMRE: Dr. Chai Jian wei, Dr. Liu Hong fei, Dr. Zhang Xin hai, Dr. Ke Lin, Dr. Wang Benzong and Mr. Rayson and also lab officers from COE Ms. Musni bte Hussain and Mr. Tan Beng Hwee. Thanks for your precious time and efforts to help me on various aspects of my research work.

I would like to acknowledge the financial support from NUSNNI and Prof. Venky Venkatesan for providing me such a good research environment in NUSNNI.

My sincere appreciation goes to Prof. Ding Jun and Ms. Bao Nina for allowing me to access their PLD system and train me to be a qualified user of the system.

I am also grateful for the accompany of my friends and lab mates in COE especially Dr. Gao Hongwei, Dr. Niu Jing, Dr. Huang Jian, Dr. Seetoh Peiyuan, Dr. Kwadwo, Dr. Liu Yi, Dr. Patrick Tung, Dr. Zhang Li and Dr. Zhang Chen. Thanks for making my PhD life extremely entertaining and memorable. My sincere thanks also go to my friends outside COE, Dr. Tan Xi, Ms. Pang Yi, Ms. Zhang Lu, Dr. Zhang Qiang, Ms. Nie Jing, Mr. Zhao Peng, and Ms. Bao Nina for always being around me to share my happiness and helping me out during my difficult time. I am grateful for all of you to always put up a smile on my face.

Most of all, I would like to express my profound gratitude to my parents and other family members. Thank you for your endless love, support and understanding. You are in the warmest place of my heart.

# Table of Contents

Acknowledgements.....	ii
Table of Contents.....	iv
Summary.....	vii
List of Tables.....	ix
List of Figures.....	x
List of Acronym.....	xiv
Chapter 1 Introduction.....	1
1.1 Introduction.....	1
1.2 Background.....	1
1.2.1 Crystal Structure.....	2
1.3 Doping in ZnO.....	4
1.3.1 Intrinsic doping (defects).....	4
1.3.2 n-type doping.....	8
1.3.3 p-type doping.....	9
1.4 Motivation and Objectives.....	13
1.5 Organization of the thesis.....	14
Chapter 2 Experiment techniques for growth and characterization of ZnO.....	17
2.1 Introduction.....	17

2.2 Growth of ZnO .....	17
2.2.1 Growth by aqueous solution method .....	17
2.2.2 Growth by pulsed laser deposition .....	32
2.3 Characterization of ZnO .....	38
2.3.1 Field-emission scanning electron microscopy (FESEM) .....	38
2.3.2 Photoluminescence spectroscopy (PL) .....	39
2.3.3 X-ray photoelectron spectroscopy (XPS) .....	47
2.3.4 Terahertz time-domain spectroscopy (THz-TDS) .....	50
Chapter 3 THz-TDS characterization of n-type ZnO:Ga grown by PLD .....	54
3.1 Introduction .....	54
3.2 Background .....	54
3.3 Theoretical model .....	56
3.3.1 Transmission coefficient .....	56
3.3.2 Drude model .....	58
3.4 Samples preparation and experimental details .....	59
3.5 Results and discussion .....	61
3.6 Summary .....	68
Chapter 4 Intrinsic doping of ZnO nanorods grown by solution method .....	70
4.1 Introduction .....	70
4.2 Background .....	70

4.2.1 Microwave heating and its growth mechanism .....	70
4.2.2 Effect of pH in solution growth.....	76
4.3 Sample preparation and experimental procedure .....	79
4.4 Results and discussion.....	80
4.4.1 Comparison of microwave and waterbath growth.....	80
4.5 Summary .....	91
Chapter 5 Optimized route towards stable p-type potassium doped ZnO by low temperature solution growth method .....	92
5.1 Introduction .....	92
5.2 Ionic equilibrium model of KAc-ZnAc <sub>2</sub> .....	92
5.3 Experimental procedure .....	96
5.4 Results and discussion.....	98
5.5 Effect of thermal annealing .....	104
5.5 Summary .....	110
Chapter 6 Conclusions and outlook .....	112
Bibliography .....	116
Appendices.....	132

## Summary

There has been intense research interest in ZnO due to its attributes of wide direct band gap (3.37 eV), high exciton binding energy (60 meV) and piezoelectric properties, which have made it to be an extraordinary material for many applications, especially in optoelectronic devices. As a semiconductor material, doping of ZnO is crucial in tuning the various properties of ZnO. However, the various kinds of doping (intrinsic and foreign, p-type and n-type) and their effects on ZnO are far from fully understood now but are highly desirable from the perspectives of excellent ZnO based devices.

In this thesis, we have studied the doping and its effects on the electrical and optical properties of ZnO film and nanostructures synthesized by pulsed laser deposition (PLD) and solution method (microwave and conventional water bath heating). Firstly, through the study of Ga-doped n-type ZnO films grown by PLD at different doping levels, it is found that the doping concentration has strong effect on the electron effective mass and scattering time. When the electron concentration is increased from  $5.9 \times 10^{17} \text{ cm}^{-3}$  to  $4.0 \times 10^{19} \text{ cm}^{-3}$ , the electron effective mass varies from  $0.23m_0$  to  $0.26m_0$ . The study was accomplished by a combination of THz-TDS and Hall measurement techniques for the first time, which possesses the advantages of ease of measurement, accuracy and wide accessibility. It is also noticed that the electron mobility determined by THz-TDS can be 7 times greater than that obtained by Hall measurement and explained for the first time by the effect of carrier localization.

Next, intrinsic doping in ZnO nanorods grown by solution method is studied, with the effects of pH and post annealing treatment. It is found that within the pH range of 10.3 – 10.9, the main intrinsic doping contributors are oxygen interstitials and zinc vacancies. A comparison between



the ZnO nanorods grown by traditional heated water bath method and microwave synthesis is also presented. It is found that with microwave heating, the growth introduces a lower intrinsic doping level and a more uniform spatial distribution of nanorods than that of conventional water bath method. Combined with the fast growth rate and low cost, microwave heating synthesis will benefit the manufacturing of ZnO devices with high throughput on wide variety of substrates, such as plastic, polymer, paper as well as traditional ones.

Lastly, p-type doping in ZnO by potassium is investigated. By varying the growth environment through precursor concentration, pH, annealing temperature, stable and reliable p-type ZnO film growth conditions have been optimized. The acceptor concentration obtained for as-grown ZnO is  $2.6 \times 10^{16} \text{ cm}^{-3}$ , which increases to  $3.2 \times 10^{17} \text{ cm}^{-3}$  after being annealed at  $700^\circ\text{C}$  for 30 minutes. An ionic equilibrium model is also provided, which gives an insight of the majority species present in the growth solution and the part they play in the growth. The synthesis route of K-doped p-type ZnO by low temperature aqueous solution paves the way of reliable p-type ZnO for future device applications.

## List of Tables

<b>Table 1.1</b> ZnO photoluminescence color and its associated intrinsic doping/defects. C.B. and V.B. are the acronyms of conduction band and valence band respectively [17].	6
<b>Table 1.2</b> Intrinsic doping concentration of ZnO films grown by different methods taken from reference [29].	7
<b>Table 1.3</b> Carrier concentration, growth method and ionization energy of n-type dopants of ZnO from group III (Al, Ga, In) and VII (F, Cl).	8
<b>Table 1.4</b> Values of ionic radius and ionization energy $E_i$ for each of the single element acceptor of ZnO obtained from theoretical calculations and experiment measurements and also acceptor complexes of Group VA elements and their calculated ionization energies $E_{def}$ [58].	11
<b>Table 2.1</b> Parameters of ZnO and related substrates [94].	29
<b>Table 2.2</b> The preparation of the stock solution of ZnO nanoparticles from Yang's method and Packolski's method.	30
<b>Table 3.1</b> Summary of the transport and dielectric properties of n-ZnO samples obtained from Hall and THz-TDS measurement.	67
<b>Table 5.1</b> Summary of the measured Hall carrier concentrations for samples A, B, C, D and E for various thermal annealing treatments. A positive and negative sign indicates hole and electron concentration ( $\text{cm}^{-3}$ ) respectively, while numbers in parentheses indicate the mobility ( $\text{cm}^2\text{V}^{-1}\text{s}^{-1}$ ).	108

## List of Figures

<b>Figure 1.1</b> (a) The schematic diagram of ZnO wurtzite crystal structure and (b) its common planes. ....	3
<b>Figure 1.2</b> The energy states of intrinsic doping element in ZnO reported by different groups from reference [17]. The charged deep levels are denoted by “+” and “-” sign on top of the abbreviation.....	6
<b>Figure 2.1</b> Illustration of the concept of supersaturation and solubility obtained from reference [84]......	20
<b>Figure 2.2</b> Classification of nucleation based on supersaturation and vicinity of crystal assistance.....	21
<b>Figure 2.3</b> Change of the free energy with respect to size of nucleus $r$ [87]. ....	22
<b>Figure 2.4</b> Hydrolysis of hydrated $Zn^{2+}$ ions in solution. The $Zn^{2+}$ ions with large positive charges attracts the electron from O-H bond of the water molecule, are more likely to cause the break of the O-H bond and dissociate $H^+$ ion into the solution. ....	26
<b>Figure 2.5</b> Uneven charge distribution in the opposite sides of ZnO c-plane, from reference [91]. ....	28
<b>Figure 2.6</b> ZnO nanorods grown on silicon (a) coated with a seed layer of ZnO nanoparticle (b) coated with a layer of Au catalyst from reference [93]. ....	30
<b>Figure 2.7</b> The setup of microwave heater (CEM Discover), water bath heater (PolyScience) and glass bottle. ....	31
<b>Figure 2.8</b> The schematic diagram of a PLD system [100]. ....	34
<b>Figure 2.9</b> The schematic diagram of FESEM from reference [106]. ....	39
<b>Figure 2.10</b> Schematic band structure of ZnO. ....	41
<b>Figure 2.11</b> Free and bound exciton recombination in the PL spectra of ZnO band edge emission region [107]. Selected transitions are indicated by vertical lines. The different areas mark the energy range of free excitons (FX), ionized donor bound excitons ( $D^+X$ ), neutral donor bound excitons ( $D^0X$ ), acceptor bound excitons ( $A^0X$ ), deeply bound excitons (Y), and two electron satellites (TES) of shallow and deeply bound excitons in their 2s and 2p states [109]......	42
<b>Figure 2.12</b> Exciton energy levels with respect to quantum number $n$ [111]. ....	43
<b>Figure 2.13</b> Illustration of free exciton (FX), neutral donor bound excitons ( $D^0X$ ), ionized donor bound excitons ( $D^+X$ ) and neutral acceptor bound excitons ( $A^0X$ )......	44

<b>Figure 2.14</b> Bound-excitonic region of the PL spectrum of annealed ZnO substrate measured at 10 K [112].	45
<b>Figure 2.15</b> The DLE spectrum of ZnO nanorods by solution method with 0.02 M zinc acetate, 0.6 ml ammonia and 20ml H <sub>2</sub> O at 90°C for 20 minutes.	46
<b>Figure 2.16</b> Schematic diagram showing the working principle of XPS.	48
<b>Figure 2.17</b> Main components of VG ESCA LAB-220i XL XPS setup in IMRE.	49
<b>Figure 2.18</b> Schematic diagram of THz-TDS setup, adopted from [127].	53
<b>Figure 3.1</b> Schematic diagram of the THz signal transmitted through bare sapphire substrate (reference) and sample with ZnO film on top of it.	56
<b>Figure 3.2</b> Transmitted THz signals in (a) time domain and (b) frequency domain (0.1-2 THz). The transient pulses in (a) have been shifted horizontally for easy observation.	62
<b>Figure 3.3</b> The ratio between imaginary part and real part of conductivity ( $\text{Im}(\sigma)/\text{Re}(\sigma)$ ) as a function of angular frequency $\omega$ for sample 1 (red circle), sample 2 (blue square) and sample 3 (green triangle). Fitted linear lines whose slopes reveal electron scattering time are also shown.	65
<b>Figure 3.4</b> The imaginary part of dielectric function $\epsilon_i$ as a function of angular frequency $\omega$ for sample 1 (blue), sample 2 (red) and sample 3 (green) in double log plot. Fitted linear lines by Drude model are also shown.	67
<b>Figure 4.1</b> Diagram of the electromagnetic spectrum, showing various properties across the range of frequencies and wavelengths [150].	71
<b>Figure 4.2</b> Water molecules experience the changing of electric field under microwave radiation [149].	72
<b>Figure 4.3</b> Comparison between conductive heating and microwave heating. The key features of each heating are listed.	73
<b>Figure 4.4</b> The energy change of a chemical system with respect reaction time [150].	74
<b>Figure 4.5</b> pH determines the surface charge of ZnO, adopted from reference [168].	78
<b>Figure 4.6</b> Top-view SEM images of the as-grown ZnO nanorods samples by microwave synthesizer (first row samples: M1 to M5) and heated water bath (second row samples: W1 to W5) respectively at 90°C for 20 minutes with different [NH <sub>3</sub> ] (0.255 M, 0.503 M, 0.748 M, 0.988 M and 1.222 M) and 0.02 M ZnAc <sub>2</sub> .	81
<b>Figure 4.7</b> The summary of statistical analysis of ZnO nanorods diameter and length grown by microwave synthesis and heated water bath (samples M1 to M5 and W1 to W5).	82

**Figure 4.8** The top view of the ZnO nanorods grown with (a) microwave synthesis (M4) and (b) heated water bath (W4). The inset is the high magnification of the tip of the nanorods (top right) and the statistics of the nanorods diameter for sample M4 and W4 (bottom right) respectively. 82

**Figure 4.9** (a) XPS survey spectrum of ZnO nanorods. (b) The integrated peak area of O 1s and Zn 2p for as-grown samples under different ammonia concentration. (c) The quantified percentage of O 1s in ZnO of as-grown and annealed samples grown by microwave synthesis and heated water bath..... 84

**Figure 4.10** (a) O 1s peak from XPS deconvoluted into three Gaussian-Lorentz peaks (O1, O2 and O3 assigned in the plot) for sample M1. (b) Percentage of O2 in the total O 1s peak for as-grown microwave and water bath assisted heating samples. .... 86

**Figure 4.11** Low temperature photoluminescence spectra of ZnO nanorods normalized to band edge peak at 3.37 eV at 20 K for (a) as-grown heated water bath samples (b) as-grown microwave synthesis samples (c) annealed heated water bath samples and (d) annealed microwave synthesis samples as a function of [NH3]. .... 87

**Figure 4.12** The ratio of (a) orange and (b) green emission to the band-edge emission for as-grown and annealed samples by both microwave and water bath assisted heating..... 88

**Figure 4.13** (a) The  $A_1(\text{LO})$  peak of Raman scattering for as-grown W1 measured at room temperature. (b) The actual measured (scattered) and fitted (line)  $A_1(\text{LO})$  peak position for both microwave synthesized and heated water bath samples in different [NH3]. .... 89

**Figure 4.14** The FWHM of the  $A_1(\text{LO})$  peak from Raman scattering measurement for the as-grown ZnO samples by microwave synthesis and heated water bath with different [NH3]. ..... 91

**Figure 5.1** (a) Plot of growth solution pH and  $C_{\text{Zn}}^*$  against the concentration of KAc. (b) Plot of concentration of  $\text{K}^+$ ,  $\text{Zn}^{2+}$  and the ratio of  $\text{K}^+/\text{Zn}^{2+}$  against the concentration of KAc. The concentration ratios of  $\text{K}^+/\text{Zn}^{2+}$  for samples A, B, C, D, and E, which correspond to 0, 0.03, 0.05, 0.13, and 0.18 M KAc, are marked accordingly in the plot..... 95

**Figure 5.2** SEM images showing the top and cross-sectional views of samples A, B, C, D and E which were grown in 0, 0.03, 0.08, 0.13 and 0.18 M KAc respectively. The thickness of each ZnO film is shown on the upper right corner of the cross-sectional image..... 98

**Figure 5.3** XRD spectra of as-grown samples A, B, C, D and E which were grown in 0, 0.03, 0.08, 0.13 and 0.18 M KAc respectively. .... 99

**Figure 5.4** SIMS depth profile of potassium concentrations in the as-grown samples A, B, C, D and E which are grown in 0, 0.03, 0.08, 0.13 and 0.18 M KAc respectively. Although the concentration ratio of  $\text{K}^+/\text{Zn}^{2+}$  increases from C to E, the amount of K incorporated in the ZnO lattice is relatively unchanged..... 100

**Figure 5.5** Hall effect carrier concentrations for as-grown samples A, B, C, D and E which were grown in 0, 0.03, 0.08, 0.13 and 0.18 M KAc respectively. A break at  $10^{10} \text{ cm}^{-3}$  is inserted along the vertical axis in order to improve clarity of the plot at higher carrier concentrations..... 101

**Figure 5.6** Schematic diagram of  $\text{K}_{\text{Zn}}\text{-H}_i$  complex and  $\text{K}_{\text{Zn}}\text{-K}_i$  complex in ZnO. .... 102

**Figure 5.7** (a) Room temperature resonance Raman scattering spectra and (b) plot of peak positions of  $\text{A}_1(\text{LO})$  against the concentration of KAc for as-grown samples A, B, C, D and E which are grown in 0, 0.03, 0.08, 0.13 and 0.18 M KAc respectively. The inset of (b) shows the fitted components consisting of the  $\text{A}_1(\text{LO})$  peak and its surface mode for sample C..... 103

**Figure 5.8** (a) XPS survey scan spectra of as-grown sample C (0.08 M KAc) at 25, 300 and 600°C. (b)The narrow scan of K 2p peaks at 300 and 600°C. (c) The plot of quantified atomic percentage of K from the narrow scan XPS spectra against the annealing temperature. .... 105

**Figure 5.9** Plot of peak positions of  $\text{A}_1(\text{LO})$  against various annealing temperatures for samples A, B, C, D and E. The samples were subjected to annealing temperatures of 100, 200, 300 and 700°C for 10 minutes, and a final 700°C for 30 minutes, indicated at 700-30 in the plot. The sample plotted in red was without K-doped sample. .... 106

**Figure 5.10** Plot of Hall carrier concentrations for as-grown samples A, B, C, D and E after annealing treatment. The horizontal axis indicates the heat treatment: as-grown, 300°C 10 minutes, 700°C 10 minutes and 700°C 30 minutes. .... 107

## List of Acronym

$A^0X$	neutral acceptor bound excitons
APCVD	atmospheric pressure chemical vapor deposition
$A^-X$	ionized acceptor bound excitons
C.B.	conduction band
$D^+X$	ionized donor bound excitons
$D^0X$	neutral donor bound excitons
DI	deionized
DLE	deep-level emission
EL	electroluminescence
ESCA	electron spectroscopy for chemical analysis
FESEM	field-emission scanning electron microscopy
FXs	free excitons
HMT	hexamethylenetetramine
ISB	inter-subband
LEDs	light-emitting diodes
LO	longitudinal phonon
LT-GaAs	low temperature grown GaAs
LTPL	low temperature photoluminescence
MOCVD	metal organic chemical vapor deposition
NBE	near band edge
$O_i$	oxygen interstitials
$O_v$	oxygen vacancies
$O_{zn}$	zinc antisites
PL	photoluminescence
PLD	pulsed laser deposition
PZC	point of zero charge
QCL	quantum cascade laser
RHEED	reflection high-energy electron diffraction
RT	room temperature
TES	two electron satellites
THz-TDS	Terahertz time-domain spectroscopy
UHV	ultra-high vacuum
UV	ultraviolet
V.B.	valence band
WD	working distance
XPS	X-ray Photoelectron Spectroscopy
$Zn_i$	zinc interstitials
$Zn_o$	oxygen antisites
ZnO	zinc oxide
$Zn_v$	zinc vacancies

# Chapter 1 Introduction

## 1.1 Introduction

In this chapter, a historical background and some basic properties of ZnO are introduced. An in-depth overview of the current status and challenges on the doping of ZnO for n-type, p-type and intrinsic doping will be presented. Finally, the motivation and organization of this thesis will be addressed.

## 1.2 Background

A tremendous amount of research effort and progress has been made in the field of oxide-based functional materials. Among these oxide materials, zinc oxide (ZnO) has attracted substantial attention in the scientific community since 1935 [1] due to its availability of a variety of growth methods, a diverse configurations of nanostructures [2], relatively biosafe and biocompatible [3], radiation hard, amenable to wet chemical etching and hence low processing cost which appeals to commercialization and industry applications [4]. Although ZnO has been a research focus for many years, the resurgent interest in ZnO from mid-1990s onwards is fueled by its potential for photonic and electronic applications, such as light-emitting diodes (LEDs), laser diodes, solar cells, photodetectors, field effect transistors, piezoelectric nanogenerators and gas and chemical sensors [5, 6]. Together with the availability of single crystal ZnO substrates, thin films and a variety of novel nanostructures, ZnO is an ideal candidate to be used for integrated high density multi-functional devices. However, as many of these devices require both donor and acceptor doping above  $10^{17} \text{ cm}^{-3}$  to form a p-n junction, widespread development of ZnO-based devices has been inhibited due to the difficulty in achieving reproducible and stable p-type ZnO. The



difficulty of p-doping does not stop the research passion and interest in ZnO, but encourage researchers to explore more in ZnO. In order to overcome the bottleneck of p-type doping in ZnO, the research community adopts two research strategies. One insists in obtaining homojunction ZnO devices by improving the stability and reproducibility of p-type ZnO through understanding the reaction pathways, attempting various dopants and numerous post growth treatments. The other focuses on building up heterojunction by using other substitutional p-type materials, such as p-GaN, p-SiC, and polymers [7]. Even some exotic devices which can get rid of junction, such as quantum cascade laser, are also proposed. However, for these heterojunction or junction-free devices, the requirement of the n-type doping ZnO layer is demanding in terms of doping level, conductivity as well as crystal quality. On top of that, no matter which strategy is taken, minimizing the intrinsic doping level is desired for the precise control of carrier concentration and crystal quality. Several exhaustive reviews on the recent progress of ZnO have been published [1, 8, 9].

### 1.2.1 Crystal Structure

Before going deep into the defects, a review of the crystal structure of ZnO is beneficial. ZnO, II-VI binary compound semiconductor, with a direct wide band gap of 3.37 eV and a large exciton binding energy of 60 meV at 300 K, typically crystallizes in a wurtzite crystal structure which is a thermodynamically stable phase under ambient conditions. The wurtzite structure has a hexagonal unit cell with two lattice parameters  $a$  and  $c$  in the ratio of  $c/a = 1.633$ , where  $a = 3.2495 \text{ \AA}$  and  $c = 5.2069 \text{ \AA}$ . The density of ZnO is  $5.605 \text{ g}\cdot\text{cm}^{-3}$  [10]. A schematic diagram of the wurtzite ZnO structure is shown in **Figure 1.1(a)**.

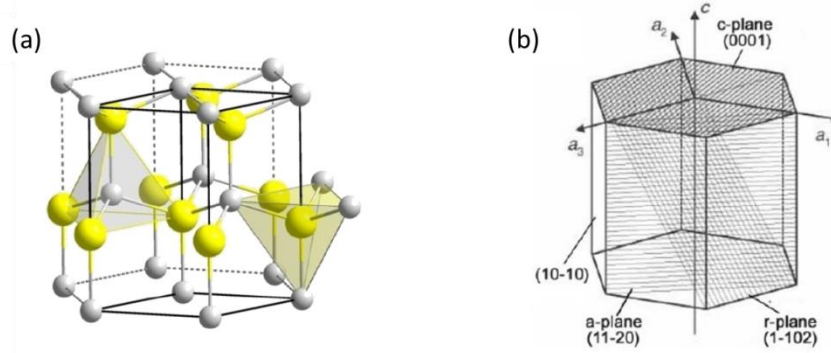


**Figure 1.1** (a) The schematic diagram of ZnO wurtzite crystal structure and (b) its common planes.

In the wurtzite structure, each  $\text{Zn}^{2+}$  is surrounded tetrahedral by four  $\text{O}^{2-}$  and vice versa. This tetrahedral coordination characterizes covalent bonds with  $sp^3$  hybridization. It is known that when moving from the group IV to the III-V and from II-VI to the I-VII semiconductors, the ionic bonding becomes stronger. Thus, ZnO shows a substantial amount of ionic bonding (61.6%) [11]. The bottom of the conduction band is formed essentially from the  $4s$  levels of  $\text{Zn}^{2+}$  and the top of the valence band from the  $2p$  levels of  $\text{O}^{2-}$  [12]. In addition, the tetrahedral coordination gives a polar symmetry along the  $c$ -axis. This polarity is responsible for its piezoelectricity, spontaneous polarization, anisotropic crystal growth habit, etching behavior and defect generation.

The common polar and non-polar planes in the wurtzite structure are shown in Figure 1.1(b). Common polar face terminations of wurtzite ZnO are the Zn-terminated (0001) and O-terminated  $(000\bar{1})$  faces which are both  $c$ -axis oriented. The common non-polar faces are  $(11\bar{2}0)$  which are  $a$ -axis oriented. Both  $(10\bar{1}0)$  and  $(1\bar{1}02)$  faces both have equal number of Zn and O atoms.

## 1.3 Doping in ZnO

In order to realize the full range of applications of ZnO, it is desired to have a low level of intrinsic doping (defects) and a high and stable n- and p-type doping concentration (above  $10^{17}$   $\text{cm}^{-3}$ ). Doping is very critical to a semiconductor material as it can tune its properties, such as structural phase transition [13], electrical conductivity, optical emission and magnetic properties [14]. Thus, it is important to understand the doping issue from both the material and device perspectives. In this section, we will give a brief introduction of the doping mechanism, dopant energy levels, state-of-the-art achievements and remaining challenges for n- and p-type doping as well as intrinsic doping, which will help the readers to gain an insight into understanding Chapters 3, 4 and 5 of this thesis.

### 1.3.1 Intrinsic doping (defects)

Intrinsic dopants in oxide materials usually refer to defects with a break in the periodicity of a crystalline lattice. It extensively exists in crystalline materials in different forms, such as point defects (vacancies, interstitial atoms, off-center ions and antisite defects), line defects (dislocations), planar defects (grain boundaries and stacking faults), and even bulk defects (voids or impurity clusters). ZnO has predominantly ionic bonds and is prone to a variety of cationic and anionic point defects.

Generally, intrinsic doping in ZnO is contributed by the following three causes:

**Vacancies:** absence of atoms in the lattice, such as oxygen vacancies ( $\text{O}_v$ ), zinc vacancies ( $\text{Zn}_v$ ).

**Interstitials:** additional atoms occupy the space in between the regular atoms in the lattice, such as oxygen interstitials ( $O_i$ ) and zinc interstitials ( $Zn_i$ ).

**Antisites:** an oxygen atom replaced by zinc atom in the lattice or vice versa, such as oxygen antisites ( $Zn_o$ ) and zinc antisites ( $O_{zn}$ ).

Besides the doping of oxygen and zinc, hydrogen is easily incorporated into ZnO as a donor in all the synthesis methods and because of its high mobility, it is easy to diffuse into ZnO. Usually, it is tightly bounded to oxygen to form an OH bond at a bond length of 1 Å and a formation energy of 1.56 eV [15]. Hydrogen also exists in p-type ZnO. In fact, the incorporation of hydrogen can suppress the defects arising from compensation and increase the acceptor solubility by forming H-acceptor complexes, such as  $H_i-Li_{Zn}$ ,  $H_i-Na_{Zn}$  and  $H_i-K_{Zn}$  [16]. By post-annealing, H atoms are easily dissociated with the complex and the acceptors are reactivated for p-type conductivity. Addition to single element dopants, the clusters of intrinsic doping are also formed by the combination of two point defects or one intrinsic point defect and one extrinsic element, such as  $V_oZn_i$  cluster consisting of  $Zn_i$  and  $V_o$  [17].

The dependence of intrinsic doping densities on their formation energies can be obtained through density-functional calculations based on the following equation (1.1), which is valid at the thermodynamic equilibrium and in diluted cases (defects isolation) [18]:

$$c = N_{sites} \exp\left(\frac{-E^f}{k_B T}\right), \quad (1.1)$$

where  $c$  is the intrinsic doping concentration,  $N_{sites}$  is the number of available sites the defects can occupy,  $E_f$  is the formation energy which depends on the growth environment and the annealing

condition,  $k_B$  is the Boltzmann constant and  $T$  is the temperature in Kelvin [19]. The energy level of each intrinsic dopant reported by different groups is depicted in **Figure 1.2** [17]. It is noticed that the energy levels of these intrinsic dopants reside in the forbidden gap, which are the origin of the deep-level emission bands in the photoluminescence spectrum of ZnO. Different reports have assigned intrinsic dopants to different energy levels with different emission origins.

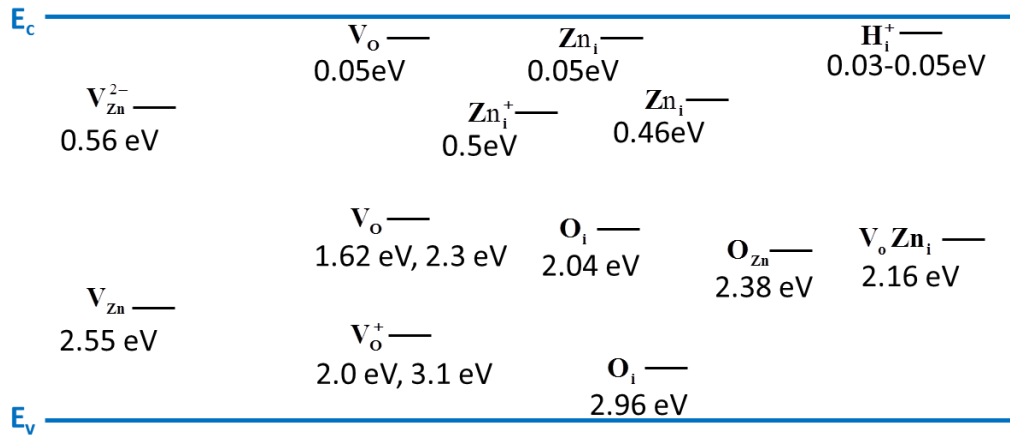


**Figure 1.2** The energy states of intrinsic doping element in ZnO reported by different groups from reference [17]. The charged deep levels are denoted by “+” and “-” sign on top of the abbreviation.

**Table 1.1** ZnO photoluminescence color and its associated intrinsic doping/defects. C.B. and V.B. are the acronyms of conduction band and valence band, respectively [17].

Emission color (nm)	Proposed deep level transition
Violet	$Zn_i$ to V.B. [20]
Blue	$Zn_i$ to $V_{zn}$ or C.B. to $V_{zn}$ [20], [21]
Green	C.B. to $V_o$ , or to $V_{zn}$ , or C.B. to both $V_o$ and $V_{zn}$ [22],[23],[24]
Yellow	C.B. to $Li$ , or C.B. to $O_i$ [25], [26], [27]
Orange	C.B. to $O_i$ or $Zn_i$ to $O_i$ [20]
Red	Lattice disorder along the c-axis (i.e. due to $Zn_i$ ) [28]

**Table 1.1** above summarizes the most thoroughly investigated defects and their well accepted assignments of the energy levels from photoluminescence measurements, although some of them are still under debate. The detail of the photoluminescence characterization will be discussed in section 2.3.2.

ZnO naturally exhibits n-type conductivity due to the presence of unintentional intrinsic doping by constituent elements in various synthesis methods. **Table 1.2** summarizes the intrinsic doping concentration of ZnO films using different methods on different substrates.

**Table 1.2** Intrinsic doping concentration of ZnO films grown by different methods taken from reference [29].

Type of film	Growth method	Intrinsic electron conc. (cm <sup>-3</sup> )	Substrate	Ref.
Polycrystalline	Magnetron sputtering	10 <sup>19</sup>	glass and sapphire	[30]
Polycrystalline	MOCVD	10 <sup>17</sup> -10 <sup>18</sup>	sapphire	[31]
Polycrystalline	Aqueous solution	10 <sup>19</sup>	MgAl <sub>2</sub> O <sub>4</sub> (111)	[32]
Single crystal	Hydrothermal at 300-400°C	10 <sup>13</sup> -10 <sup>14</sup>	ZnO seed	[33]
Single crystal	PLD	10 <sup>15</sup> -10 <sup>16</sup>	sapphire	[34]

It is noticed that compared to polycrystalline ZnO, single crystal ZnO has a lower intrinsic doping density applicable to various methods. In addition, the solution method can achieve a comparable intrinsic doping level as the vapor phase methods. Recently, a novel approach of solution phase growth, using microwave heating, can assist ZnO to grow even faster, with greater uniformity, and saving energy compared to conventional thermal heating. However, the microwave heating has not been fully explored, especially in term of the intrinsic doping into ZnO synthesized by it. The advantages of microwave heating provide strong impetus for the

investigation of the differences between the microwave and conventional water bath heating methods, regarding the intrinsic doping properties. The results will be presented in **Chapter 4**.

### 1.3.2 n-type doping

Compared to unintentionally doped ZnO by intrinsic elements, extrinsic n-type doping of ZnO is favored due to their stability and controllability for a specific doping concentration. Up-to-date, n-type doping from Group-III elements (B, Al, Ga and In) substituted on the Zn sites as shallow donors in ZnO are well established. At the same time, elements from group-VII (F, Cl, Br) substituted on the O sites also demonstrated a high n-type conductivity [35]. The n-type doping with group III and VII elements have been investigated by many groups and the ionization energy of some elements have also been well studied. The results are compiled in **Table 1.3**.

**Table 1.3** Carrier concentration, growth method and ionization energy of n-type dopants of ZnO from group III (Al, Ga, In) and VII (F, Cl).

Dopant	Electron conc.(cm <sup>-3</sup> )	Growth method	Ionization energy
Al	3×10 <sup>19</sup>	RF magnetron sputtering [36]	51 meV [37]
	1.5×10 <sup>21</sup>	Photo-assisted MOCVD [40] PLD [41]	53 meV [38] 55 meV [39]
Ga	1.1~3×10 <sup>20</sup>	MBE[42] CVD[43]	54.6 meV[42] 54.5 meV[38]
	5×10 <sup>20</sup>	RF magnetron sputtering [36]	
In	1.7×10 <sup>19</sup>	RF magnetron sputtering [44]	63.2 meV[45]
F	5×10 <sup>20</sup>	Atmospheric pressure chemical vapor deposition (APCVD)[46]	80 meV[47]
Cl	~10 <sup>20</sup>	MOCVD [48]	

Group VII element has relatively lower solubility than that of group III element (7%) due to the lower vapor pressures of Group III compared to Group VII [49]. In addition, another issue with Group VII element doping is that after using Cl and iodine from Group VII under low-pressure deposition environment, the concentration of residual electron remains at a high level known as the memory effect [42]. E. Chikoidze achieved a maximum doping level of  $4 \times 10^{20} \text{ cm}^{-3}$  using MOCVD under chlorine pressure of 84 Pa which almost reach the solubility of Cl. Among Group III elements, the oxidation of Al source is a severe issue in MBE growth but Ga and In have lower reactivities with oxygen compared to Al [50]. Mercedes Gabás found that the Ga cation has a higher doping efficiency than Al. Their experiment proved the hypothesis that Ga behaves as perfect a substitutional dopant but Al cation has the chance of occupying the interstitial sites [36]. Ko et al. proved that due to the large ionic radius of In, the bond length of In-O (2.1 Å) easily causes the deformation of ZnO (1.97 Å) lattice, the same case as Zn-Cl bonds (2.3 Å) [42]. Fortunately, the bond length of Ga-O (1.92 Å) is more suitable to fit into the ZnO lattice and only results in small deformation. Therefore, Ga is the optimum candidate for high concentration of n-type doping without sacrificing the crystal quality.

Besides group III and group VII elements, rare earth metals from group IIIB (Sc and Y) [50], group IV (Si [51], Ge [52] and Sn [53]) also have been attempted as n-type dopants but have not been widely adopted.

### **1.3.3 p-type doping**

Compared to n-type ZnO, the stable and reproducible p-type ZnO has been proven difficult to be achieved, which inhibited the development of ZnO based junction devices [54]. One of the main reasons was the strong self-compensation effect due to the inherent intrinsic n-doping



characteristics and hydrogen impurities as discussed in section 1.3.1. In addition, the solubility of p-type dopants in ZnO are relative low and even those potential acceptors inside ZnO have a very high chance to form deep impurity levels instead of shallow acceptor levels [50, 51].

Such a doping asymmetry problem is also seen in other wide-bandgap materials, such as GaN, and other II-VI semiconductors, such as ZnS, ZnSe and ZnTe. Researchers have put enormous and continuous effort in improving p-type ZnO and come up with many promising strategies to overcome the p-type doping difficulty after numerous experiments and theoretical studies conducted since 1997. Primarily, three different approaches have been proposed for pursuing p-type ZnO with high acceptor concentration, shallow ionization energies and minimal compensation: (1) Group IA elements (Li, Na, K) and Group IB elements (Cu, Ag, Au) substituting on Zn atoms; (2) Group VA elements (N, P, As, Sb) substituting on O atoms; (3) co-doping of dual acceptors or donor-acceptor pairs. **Table 1.4** gives an overview of the ionic radius and defects energy levels of some representative ZnO dopants from group IA, IB and group VA, obtained by theoretical calculation and experiment [57]. It is noticed that Li and N have the most closed ionic radius to the bond length of ZnO (1.93 Å). In addition, Group IA elements exhibit shallower ionic energies compared to those of group IB and group VA elements. Thus, from a theoretical point of view, group IA elements, especially Li, would be the most ideal p-type dopant.

However, the experimental results turn out to be the other way around. Due to the high diffusivity and self-compensation of group IA elements, they prefer to occupy interstitial positions, instead of substitution sites and contribute to donors other than acceptors [38]. On the other hand, Group VA elements, particularly, N is the most promising element for acceptors as

its creation of an acceptor level of 0.167 eV, obtained experimentally, is much lower than the theoretical prediction of 0.4 eV. In addition, its ionic radius (1.68 Å) is the closest to Zn-O bond length compared to other group VA impurities, although it has the issues of insufficient incorporation into the ZnO lattice sites and the formation of molecular N<sub>2</sub> centers on O sites as donors.

**Table 1.4** Values of ionic radius and ionization energy  $E_i$  for each of the single element acceptor of ZnO obtained from theoretical calculations and experiment measurements and also acceptor complexes of Group VA elements and their calculated ionization energies  $E_{def}$ [58].

Group	Element	Ionic Radius (Å)	Ionization energy $E_i$ (eV)		Proposed acceptor center and calculated ionization energy $E_{def}$ (eV)
			Theory	Experiment	
Group IA	Li	2.03	0.09[59]	0.150/0.250[60]	
	Na	2.10	0.17[59]	0.164[61]	
	K	2.42	0.32[59]		
Group IB	Cu	-	0.74[62]	3.2[63]	
	Ag	-	0.40[62]		
	Au	-	0.50[62]		
Group VA	N	1.68	0.40[59]	0.165[64]	
	P	2.12	0.93[59]	0.18[65]	$P_{zn}-2V_{zn}$ (0.18)[66]
	As	2.23	1.15[59]	0.12[67]	$As_{zn}-2V_{zn}$ (0.15)[68]
	Sb	2.45	1.10[69]	0.14[70]	$Sb_{zn}-2V_{zn}$ (0.16)[68]

As mentioned before, the co-doping is also an alternative to enhance the incorporation of acceptors in p-type ZnO. Its ionization energy is lower than the single element. Yamamoto and Hiroshi initiated N codoped with Al, Ga or In to improve p-type ZnO carrier concentration [55]. Other researchers adopted the same concept but implemented through different doping sources. J. Wu proposed K-N dual-acceptor codoping for p-ZnO with an acceptor shallow level at 0.24 eV based on first-principle study [71].

Although many controversies of p-type ZnO have been raised and some researchers still doubt the real existence of p-type in ZnO, convincing results have been accumulated in establishing p-type ZnO. In 2007, Ryu et al. obtained an electrically pumped UV lasing in ZnO laser diodes [72]. In 2010, K. Nakahara et al. demonstrated  $\text{Mg}_x\text{Zn}_{1-x}\text{O}/\text{ZnO}$  single heterostructure ultraviolet light-emitting diodes on ZnO substrates by nitrogen doping [73]. In 2012, Chua's group reported room temperature (RT) UV electroluminescence (EL) in ZnO coaxial nanorods p-n homojunction LED fabricated by aqueous solution method by K-doping [74]. All these recent progresses corroborate the existence of p-type conductivity in ZnO. Currently, the most difficult task is to have a more robust and stable p-type ZnO. In terms of stability, Li doping gives a comparable or better doping results than N, as there is no change in the p-type characteristics of Li doped ZnO for up to 60 days [75]. Lin et al. successfully demonstrated stable p-type conductivity (in the range of  $10^{16}$  to  $10^{18}$   $\text{cm}^{-3}$ ) of Na-doped ZnO film using PLD which can be maintained for 6 months. All these results together with the theoretical studies for acceptor energy levels, H-group-I-acceptor complexes show the possibility of using group I elements as stable p-dopants despite earlier difficulties.

Huang et al. proposed K as the best candidate for p-type doping compared to other nominal p-type dopants ( $\text{H}_{\text{Zn}}$ ,  $\text{Li}_{\text{Zn}}$ ,  $\text{Na}_{\text{Zn}}$ ,  $\text{K}_{\text{Zn}}$ ,  $\text{Ag}_{\text{Zn}}$ ,  $\text{N}_{\text{O}}$ ,  $\text{P}_{\text{O}}$ ,  $\text{As}_{\text{O}}$ ,  $\text{Sb}_{\text{O}}$ ,  $\text{Bi}_{\text{O}}$ ) based on their first-principle calculations and previous results [76].

Based on our previous study on K-doped p-type ZnO film and homojunction UV-LED, Chapter 5 of this dissertation gives a comprehensive thermal stability study of the K-doped p-type ZnO synthesized by aqueous solution method under different precursor concentrations and annealing temperatures.

## 1.4 Motivation and Objectives

From the above review of ZnO, doping is essential to understand the behavior of the material and to tailor its numerous physical properties and technological applications. A summary of the reasons why doping of ZnO was chosen for this study is presented below:

- A. For n-type ZnO, the reliable donors for substitution have been established which can be incorporated very well to a very high concentration and shown to be shallow donors from the strong evidence of photoluminescence (PL) spectra. However, there is still a plenty of room for n-type ZnO to improve in order to have a good control of the doping level, stoichiometry, crystal quality and interface property for advanced applications of unipolar conductivity, such as quantum cascade laser. On top of this, the understanding and measurement of the physical parameters which are important for the design and fabrication of the devices are urgently needed.
- B. Regarding intrinsic doping, it is very easily incorporated into ZnO during growth, which makes ZnO so variable in its properties. In spite of numerous experimental studies and theoretical simulations, there is still a debate on which intrinsic doping mechanism is responsible to the specific feature of ZnO. In order to have the full control of the rich intrinsic defects in ZnO, a basic physical understanding of the doping mechanism and its correlation of ZnO properties are essential. On the other hand, in some circumstances, the existence of the intrinsic doping as defects degrades the device performance and makes the doping level difficult to be controlled, especially the self-compensation issue for p-type doping. Therefore, a cheap and fast synthesis method that can decrease the intrinsic doping level without sacrificing the crystal quality is desired.

C. In the case of p-type ZnO, it is the most critical and challenging issue to resolve for living up to its potential applications in homojunction devices. Although many strategies of p-type doping have been attempted to overcome this bottleneck, a consistent, stable, and reliable high p-type conductivity ZnO is still far from being achieved and both experimental and theoretical study are required. H passivated acceptor complexes have been found can greatly enhance the solubility of acceptors and significantly reduces the self-compensated interstitials. Thus, intentional codoping with H in p-type ZnO is desired and solution method can easily incorporate H into ZnO through the careful design of the growth environment.

This thesis presents an exploratory study on understanding the doping mechanism and their effects on ZnO properties at the level of theory development, synthesis and characterization. The specific objectives are to:

- A. Develop a simple and widely accessible technique to investigate the dependence of carrier concentration of n-type ZnO films on the important parameters for device design and fabrication.
- B. Study the differences between microwave and water bath assisted ZnO growth in terms of intrinsic doping and its effects on ZnO morphology and optical properties.
- C. Explore the growth chemistry, doping mechanism and thermal stability of K doped ZnO by solution synthesis to achieve reliable p-type conductivity.

## **1.5 Organization of the thesis**

In order to target the objectives, this thesis consists of six chapters addressing the issues and challenges in ZnO doping (n-type, p-type and intrinsic) from the aspects of theoretical study,

synthesis and characterization to improve the ZnO physical properties for various applications. Besides the current chapter (Chapter 1) on ZnO background, the remaining chapters are organized in the following manner:

Chapter 2 describes the growth techniques (pulsed laser deposition and aqueous solution), growth mechanism, features and reasons of using each growth technique in this thesis. The growth procedures discussed here will be used in the rest of chapters. The working principles together with the parameters and specification of characterization tools used in the thesis are also explained in details.

Chapter 3 investigates the properties of Ga-doped n-type ZnO by employing a new and easily accessible technique to determine the carrier effective mass and carrier scattering time using THz-TDS and Hall measurement, which is believed to be vital in developing ZnO and related materials for optical devices. The physics behind the carrier concentration dependent effective mass and the discrepancy of the mobility obtained from Hall and THz-TDS are also discussed in-depth.

Chapter 4 focuses on intrinsically doped ZnO nanorods grown on Si(100) through facile microwave assisted aqueous solution method. A detailed comparison between microwave and waterbath assisted synthesized ZnO in terms of morphology, defects and optical properties across a range of pH from 10.3 to 10.9 will be carried out. The microwave route presents a better approach, leading to a more uniform distribution of nanorods with a lower native defect concentration of oxygen interstitials and zinc vacancies.

Chapter 5 proposes a theoretical model to identify the influence of growth environment chemistry on the main type and nature of potassium defects in ZnO film grown by solution method. The post growth thermal treatment effect on the doping concentration of K doped ZnO samples fabricated according to the theoretical model was presented.

Chapter 6 draws a conclusion of the thesis and provides recommendations for the future work.

## **Chapter 2 Experiment techniques for growth and characterization of ZnO**

### **2.1 Introduction**

In this chapter, the first part describes the growth methods (PLD and aqueous solution method) of ZnO film and nanorods used throughout this thesis. In the second half of this chapter, important characterization techniques for material properties studied are discussed. The specific parameters for growth condition and characterization setup and equipment models used in the work of this thesis are also addressed.

### **2.2 Growth of ZnO**

ZnO can be synthesized by various methods which can be classified into two categories: vapor phase growth and solution phase growth. Each approach has its own features and advantages. In this thesis, in order to fit the needs of different applications, aqueous solution method and pulsed laser deposition have been adopted as the main synthesis methods. The background of the techniques, equipment setup, growth mechanism and advantages of each growth method will be introduced. In addition, the reason for choosing each of the methods to meet specific objective together with growth details will be presented.

#### **2.2.1 Growth by aqueous solution method**

Since the first report from Verges's group on the successful demonstration of the aqueous solution growth of ZnO in 1990 [77], aqueous solution method has been widely adopted for ZnO



synthesis, as it is a green, low cost and non-toxic route. It can be easily scaled up and is able to achieve various novel nanostructures without the use of catalyst and high pressure. Various precursors, such as zinc nitrate and Hexamethylenetetramine (HMT) used by Vayssieres *et al.* [78], zinc acetate and ammonia demonstrated by Tay *et al.* [79], zinc nitrate, thiourea, ammonium chloride and ammonia implemented by Wang *et al.* [80], are selected as the aqueous medium to synthesize ZnO, achieving numerous morphology ranging from nanorods to nanotubes and nanosprings. Several comprehensive reviews of ZnO solution synthesis have been done by Agnieszka, Schmidt-mende, Weintraub and Heo *et al.* [78, 81, 82, 83].

One of the most attractive points of the solution synthesis is that some dopant can achieve higher doping concentration compared to that of the vapor phase method due to their higher solubility in solution, which provide the opportunities to the research community to overcome the challenge of p-type doping. Chapter 5 will explore how reliable the p-type ZnO doped by K can be obtained through the solution method. In order to further improve p-type doping, the good control of background (intrinsic) doping of ZnO is critical. This is highlighted in Chapter 4 where the solution growth assisted by microwave heating and water bath yield different intrinsic doping concentrations.

Owing to these advantages, various routes of solution phase synthesis have been attempted to obtain ZnO nanostructure and films, such as microemulsion, hydrothermal, water bath and the recent developed microwave assisted heating [82].

In order to fully utilize the advantages of the solution synthesis and achieve high quality ZnO, an understanding of the fundamental growth mechanism and chemical reaction are essential.

### 2.2.1.1 Growth mechanism

#### A. Supersaturation

Supersaturation is the state of a solution that contains more of the dissolved material than what solubility allows. It is the driving force for nucleation and growth, which is not only critical for solid phase formation but it also determines its crystal size and shape [84]. To illustrate the concept of supersaturation, we use glucose as an example. The same methodology applied to ZnO. The solubility of glucose in 100ml water at 25°C is 91 g, which is the maximum amount of glucose that can be dissolved in 100ml water. The solution is saturated at this point and its concentration is denoted as  $C^*$  [85]. If we increase the temperature to 50°C, the solubility of the glucose is increased to 244 g in 100 ml water according to the second law of thermodynamics. It is noted that the solubility is strongly dependent on temperature rather than pressure. At 50°C, 100 g of glucose dissolves in 100 ml water then the solution is unsaturated. If the mixture is cooled down to 25°C, 9 g glucose should precipitate from solution, however glucose molecules may need some time to find proper position in a solid structure before precipitating from the solution. In this case the system has a higher amount of glucose (100 g) than the solubility limit (91 g) at 25°C. As the solution dissolves more solute than the solubility limit, the solution meets the supersaturation condition as illustrated in **Figure 2.1**. Supersaturation is a measure of the difference between the actual concentration ( $C$ ) and the solubility concentration ( $C^*$ ) of solvent

at a certain temperature. The degree of supersaturation is given by  $S = \frac{C}{C^*}$ .

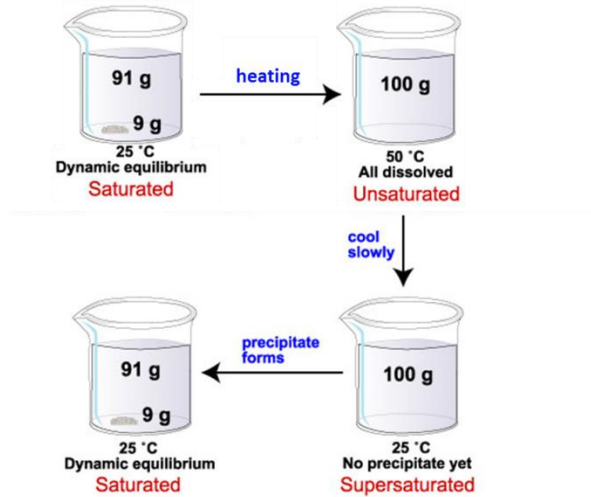


**Figure 2.1** Illustration of the concept of supersaturation and solubility obtained from reference [84].

If  $S < 1$ , the solution is unsaturated and no nucleation occurs. If  $S = 1$ , the solution reaches the solubility concentration. Once  $S$  is beyond 1, the supersaturation condition is satisfied. Several kinds of nucleation, such as homogenous nucleation, heterogeneous nucleation and secondary nucleation which will be introduced in the following section B will gradually take place depending on whether  $S$  is greater than 1 as shown in **Figure 2.2**. The concept of supersaturation and solubility applies to ZnO growth in solution method will also be explained in the section B. The nucleation of ZnO crystal starts with  $S > 1$ .

## B. Nucleation

As mentioned in the previous section, the supersaturation is a key to drive the nucleation process. Different nucleation processes can occur according to the degree of the supersaturation of the solution. Nucleation process can also be classified by whether it is assisted by the presence of the crystal of solute in the solution as illustrated in **Figure 2.2**. In fact, the nucleation is a form of

phase transformation. For the phase transformation to occur, the free energy of the new phase should be lower than that of the initial phase. The common feature for all nucleation mechanisms is that in order to form the clusters of a critical size, enabling the new solid phase (embryo) to grow spontaneously, the free energy barrier needs to be surmounted. The barrier height could be different for each nucleation process [86, 87]. Several classic books giving a very clear picture on crystallization and related topics are recommended here [84, 88].

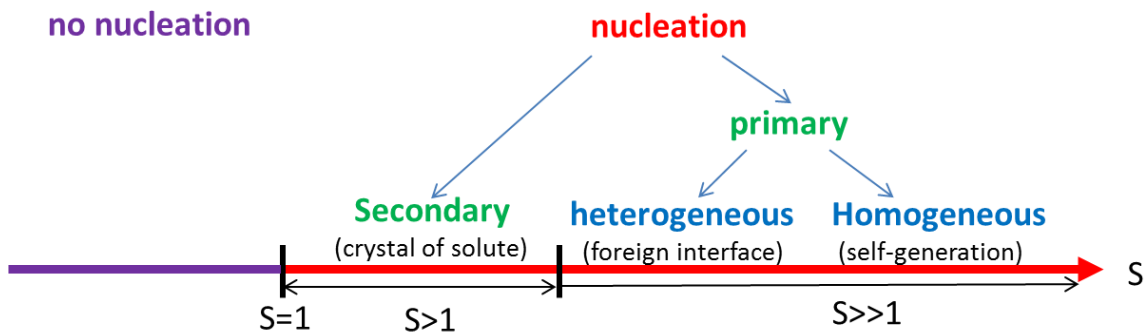


**Figure 2.2** Classification of nucleation based on supersaturation and vicinity of crystal assistance.

(a) Homogenous nucleation

Homogenous nucleation happens when there is neither the presence of a solid foreign interface nor the crystal of solute in the supersaturated solution. In solution, the collision between ions or molecules will form embryos, which are intrinsically unstable against re-dissolution. The embryos will grow by the adsorption of ions.

As the embryos are not stable, there is a probability for them to either grow into a stable nucleus or be re-dissolved, which is determined by the balance between the surface energy required to

form the embryo ( $\Delta G_s$ ) and the volume energy released when a spherical stable nucleus is formed ( $\Delta G_v$ ). Theoretically, it is expressed as:

$$\Delta G = \Delta G_s + \Delta G_v = 4\pi r^2 \gamma + \frac{4}{3} \pi r^3 \Delta G_v, \quad (2.1)$$

where  $\Delta G$  is the total excess free energy,  $r$  is the radius of the nucleus,  $\gamma$  is the surface energy per unit area, and  $\Delta G_v$  is the free energy change of the transformation per unit volume.  $\Delta G_v$  is a function of the degree of supersaturating  $S$ , given by  $\Delta G_v = -\frac{kT}{V} \ln(S)$ , where  $k$  is the

Boltzmann constant,  $T$  is the growth temperature and  $V$  is the molecular volume where  $V = \frac{4}{3} \pi r^3$ .

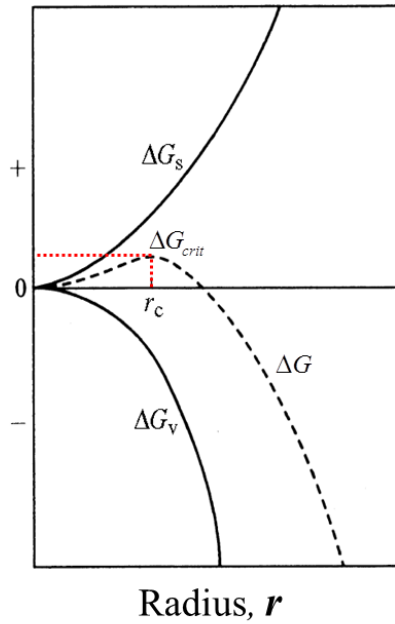


**Figure 2.3** Change of the free energy with respect to the size of nucleus  $r$  [87].

$\Delta G_s$  and  $\Delta G_v$  are competing mechanisms and have opposite signs ( $\Delta G_v$  is negative), which result from equation (2.1) giving a maximum value of  $\Delta G$  denoted by  $\Delta G_{crit}$ , and the corresponding minimum size of a stable nucleus with radius  $r_c$  shown in **Figure 2.3**, given by the

condition  $\frac{d\Delta G}{dr} = 0$

$$\Delta G_{crit} = \frac{16\pi V^2}{3k^2 T^2} \cdot \frac{\gamma^3}{(\ln S)^2}, \quad r_c = \frac{-2\gamma}{\Delta G_v}, \quad (2.2)$$

(b) Heterogeneous nucleation

It is noticed that  $\Delta G_{crit}$  is inversely proportional to  $S$ , which indicates that homogenous nucleation are more favorable to occur due to the greater value of  $S$ . Therefore, in order to prevent the precipitation of ZnO (homogenous nucleation) from taking place during ZnO growth resulting in the waste of the precursor and the contamination of the ZnO grown on the substrate and precise control of growth condition, such as temperature and  $S$ , are important according to equation (2.2) to have larger  $\Delta G_{crit}$ .

Homogeneous nucleation refers to the formation of nuclei through self-generation from ions or molecules collisions in the solution, while heterogeneous nucleation occurs when foreign interfaces are present in the supersaturated solution. It is noticed that both homogenous and heterogeneous nucleation occur without the crystal of solute and are recognized as primary nucleation classified in Figure 2.2. From the thermodynamic point of view, the understanding of homogeneous nucleation can be applied to the heterogeneous nucleation. As indicated in equation (2.2), both  $\Delta G_{crit}$  and  $r_c$  are dependent on surface energy  $\gamma$ , thus any change in  $\gamma$  leads

to a variation in the nucleation process. As the energy for nucleation between the embryo and foreign interface (heterogeneous nucleation) is less than that between the embryo and solution (homogenous nucleation), a decrease of  $\gamma$  occurs when foreign interface is involved in the nucleation process.  $\gamma$  is minimized when the best match between the foreign interface and the crystallized substance happens. This special situation is satisfied, when both foreign interface and the crystallizing substance are the same (perfect lattice match) known as the secondary nucleation.

### (c) Secondary nucleation

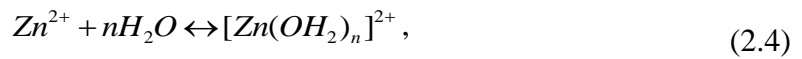
As mentioned above, the secondary nucleation is often observed when nuclei starts at a supersaturation stage  $S$  where the foreign interface and the crystallizing substance are the same material. In other words, the nucleation happens with the crystal of solute. This mechanism requires an even lower energy barrier and therefore it is much easier to nucleate at even smaller  $S$  than the case for homogenous and heterogeneous nucleation as indicated in Figure 2.2.

For the case of solution based ZnO synthesis used in this thesis, ZnO precipitates (homogeneous nucleation) as well as ZnO nucleation on the wall of vessels, sample holders (heterogeneous nucleation) need to be suppressed to avoid the waste of precursors and at the same time to promote the growth of ZnO on the substrate (heterogeneous nucleation or secondary nucleation). Depending on the substrate selected and supersaturation stage, the growth condition can be designed and controlled. In order to ease the nucleation and reduce the energy barrier, the secondary nucleation environment ( $1 < S \ll 1$ ) is favored, where the ZnO seed layer is selected as coating on the foreign substrate, such as Si(100) and sapphire(0001) before growth of ZnO in the solution. We will fully elaborate this idea in Chapters 4 and 5 of this thesis.

### 2.2.1.2 Chemical reaction

Based on the previous discussion, the growth mechanism of ZnO crystals starts with the formation of an embryo and the embryo incorporating into the crystal lattice through a dehydration reaction. ZnO crystallization can be achieved through hydrolysis of Zn salts in a base solution which can be formed using either strong or weak alkalis, such as NaOH, KOH, NH<sub>4</sub>OH. In this thesis, we use zinc acetate and ammonia as growth precursors. Zinc acetate provides the zinc ions to form embryos in the solution and ammonia, as a weak alkali, can be used to control the degree of supersaturation and the pH of the solution [89]. The main chemical reactions involved in the growth are illustrated in the following equations [90]:

Initially, cations Zn<sup>2+</sup> are dissolved in water and form the hydrated Zn<sup>2+</sup> ions:



The hydrated Zn<sup>2+</sup> ions have stronger attractive forces to the electron from the oxygen of the attached water molecules. Since oxygen is electron deficient, it starts to attract the electron in the O-H bond. This process makes the O-H bond weaken and easier to break, which is known as hydrolysis of the hydrated Zn<sup>2+</sup> ion as illustrated in **Figure 2.4**.



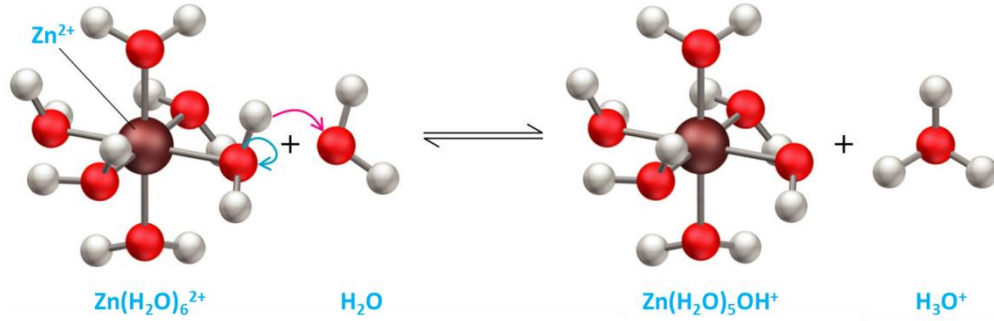
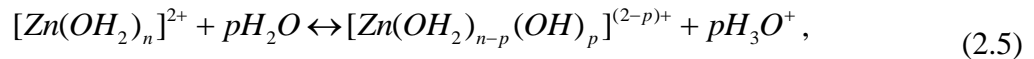
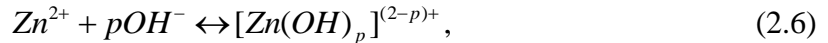


**Figure 2.4** Hydrolysis of hydrated  $Zn^{2+}$  ions in solution. The  $Zn^{2+}$  ions with large positive charges attracts the electron from O-H bond of the water molecule, are more likely to cause the break of the O-H bond and dissociate  $H^+$  ion into the solution.

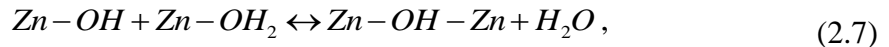
A wide range of Zinc hydroxide complexes formed through hydrolysis such as  $[Zn(OH_2)_{n-p}(OH)_p]^{(2-p)+}$  shown below:



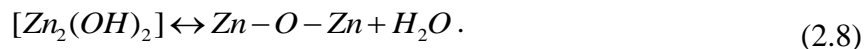
The above equation can be simplified if the water is omitted,



In order to develop into ZnO particles, condensation reactions need to take place right after hydrolysis. Olation and oxolation are the two key condensation processes being postulated. In the olation process, an “ol” bridge ( $-OH-$ ) is formed between two  $Zn^{2+}$  centers through the reaction of a hydroxo- ( $Zn-OH$ ) and aqo-species ( $Zn-OH_2$ ):



In the oxolation process, an “oxo” bridge ( $-O-$ ) is also formed between two  $Zn^{2+}$  centers is constructed through the dehydration of hydroxo-species ( $Zn_2(OH)_2$ ) shown in reaction (2.8):



In the equations (2.4) to (2.8), the ideal reaction processes of ZnO synthesis are presented. However, in the real aqueous solution, the growth environment is more complex than the simplified scenario [91]. For instance, the discussion above did not take into consideration the presence of oxygen molecules. However, Wang Zhonglin's group found that the concentration of the dissolved oxygen plays an important role in the real case, which affects the crystal quality of the ZnO [90].

Since ZnO has a wurtzite structure as shown in Chapter 1, it is hexagonal in configuration with the polar space group of P63mc. In the absence of centro-symmetric structure, it creates an uneven distribution of charge states in the opposite sides of the basal plane (c-plane) as shown in **Figure 2.5**. The c+ surface terminated with Zn dangling bond has a net positive charge, whereas the c- surface terminated with O dangling bond has a net negative charge which results in a polar surface [92]. From the thermodynamics point of view, polar surfaces are less stable and the atoms try to minimize the surface energy through rearrangement. It is easier for defects to form at these polar surfaces as their uneven charge distribution will attract the new in-coming species to grow into crystal. Dem'yanets proposes the effect of Li<sup>+</sup> ions on polar ZnO growth mechanism. Through doping Li into the (000 $\bar{1}$ ), the negative charge could be reduced and promote the growth in the [000 $\bar{1}$ ] direction [93]. In Chapter 5, we will give an insight of the growth mechanism of potassium doped ZnO and its influence on the electrical and optical properties of ZnO.

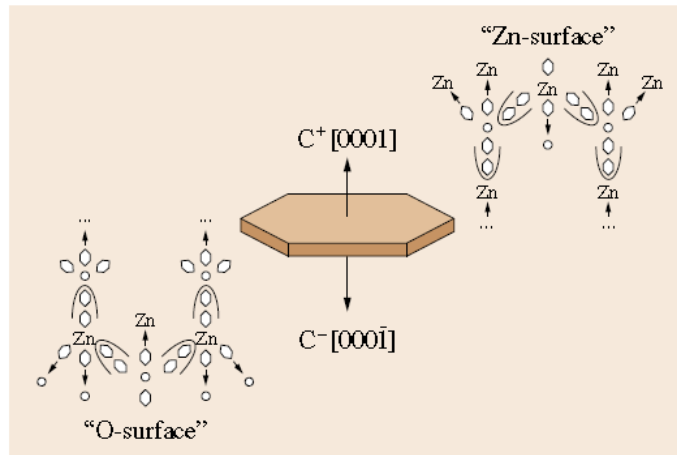


**Figure 2.5** Uneven charge distribution in the opposite sides of ZnO c-plane, from reference [91].

In addition, impurities in solutions may cause the change in molecular diffusion, atomic absorption on the surface of crystal, which will also affect the crystal growth kinetics. Since ZnO crystal is anisotropic, even very few impurities can lead to growth rate variation in some particular axis, which results in point or line defects. Due to the polarized material property of ZnO, the impurities concentration also varies in different sectors of the polar crystal, which means that the growth rate, impurity concentration and morphologies are different for the positive polar surfaces and negative polar surface. The details of the theoretical model has been suggested in the hand book of crystal growth [92]. In this thesis, Chapters 4 and 5 will give real experiment examples to investigate how the intrinsic element and potassium doping behave and affect the growth and properties of the ZnO crystals grown in aqueous solution.

### 2.2.1.3 Synthesis methodology

The growth of ZnO carried out in this thesis can be divided into four steps:

- (a) First step: ZnO seed layer

If the substrate material has a big lattice mismatch with ZnO, the pre-coating of a buffer layer on the substrate is required. As explained in section 2.2.1.1, by introducing the buffer, lattice mismatch could be eliminated, and the surface energy per unit area  $\gamma$  and the free energy for nucleation can be minimized, which will promote the growth of ZnO. **Table 2.1** shows the lattice parameters, thermal coefficient of expansion of ZnO, Si (100), and c-plane sapphire and the corresponding lattice mismatches used in this thesis.

**Table 2.1** Parameters of ZnO and related substrates [94].

Parameters of ZnO and substrates					
Material	Crystal structure	Lattice Parameters a(Å), c(Å)	Lattice Mismatch with ZnO(%)	Thermal-Expansion coefficient, (K <sup>-1</sup> ) <sub>a</sub> (10 <sup>-6</sup> ) <sub>c</sub> (10 <sup>-6</sup> )	Band Gap (eV)
ZnO	Wurtzite	3.252	0	2.9	3.37
		5.213		4.75	
c-sapphire	Wurtzite	4.758	18.4 (with 30° in-plane rotation)	5.6	9.9
		12.991		5.0	
Si	Diamond	5.431	40.1	3.59	1.12

In our experiment, the pre-coating solution consisting of 0.005 M zinc acetate dihydrate ( $\text{Zn}(\text{CH}_3\text{COO})_2 \cdot 2\text{H}_2\text{O}$ ) in ethanol is spin-coated onto the substrate at 3000 rpm for 30 sec/round. This step is repeated twice. After each round, the coated substrate is rinsed in ethanol for 10 sec and then blown dry with nitrogen. Then the coated substrate goes through the annealing process at 350°C in air for 20 mins for  $\text{ZnAc}_2$  to decompose into ZnO. This method is first introduced by Yang's group [95]. Compared to our previous growth using Pacholski's method [96], it is rather simple but has the capability to fabricate high-density vertical wire arrays free of intermediate thin films or nanoparticle layers as shown in **Table 2.2** and **Figure 2.6**.

**Table 2.2** The preparation of the stock solution of ZnO nanoparticles from Yang’s method and Pacholski’s method.

Yang Peidong’s method	Pacholski’s method
a. 0.005 M zinc acetate dehydrate in ethanol b. The stock solution was concentrated by evaporation of the solvent and heated to 350°C in air for 20 minutes to yield layers of ZnO islands with their (0001) planes parallel to the substrate.	a. 0.01 M zinc acetate dihydrate was dissolved in 125 mL methanol under vigorous stirring at about 60°C. b. 0.03 M solution of 65 mL KOH in methanol was added dropwise at 60°C. c. The reaction mixture was stirred for 2 hours at 60°C. d. The stock solution was concentrated by evaporation of the solvent and heated for different lengths of time to obtain ZnO nanoparticles.

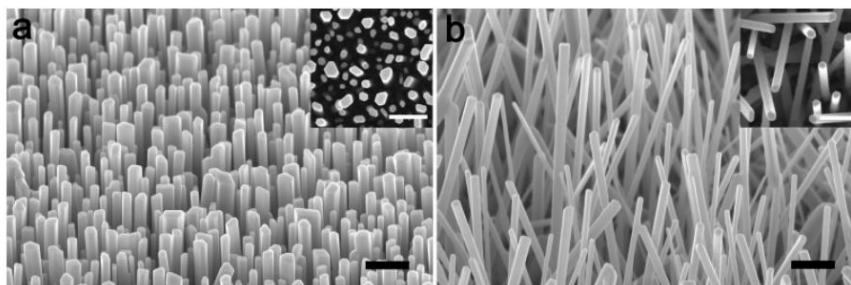


**Figure 2.6** ZnO nanorods grown on silicon (a) coated with a seed layer of ZnO nanoparticle (b) coated with a layer of Au catalyst from reference [93].

(b) Second step: growth of ZnO nanorods

The growth starts with the preparation of the growth solution. In our ZnAc<sub>2</sub>-NH<sub>3</sub> system, ZnAc<sub>2</sub> and NH<sub>3</sub> are used as precursors and dissolved in deionized water at room temperature. The exact amount of each precursor used depends on the solubility desired and are given in subsequent chapters. For the case of p-type ZnO study, potassium is also added into the growth solution. In order to have good control in the consistency of our experiment, especially for comparisons among the samples, stock solution for each of the chemical (ZnAc<sub>2</sub>, diluted ammonia, and

potassium) are prepared and later mixed with each other based on the experiment design. In this way the error within the same set of experiment is relatively small. Precaution needs to be taken to control the ammonia concentration in the solution as it is critical for determining the pH as well as Zn solubility. Ammonia evaporates very easily. Thus, the glass bottle needs to be kept closed to have a good control of the experiment. After the chemicals are fully dissolved in the solution, the substrate is placed into a Teflon sample holder at an angle of  $60^\circ$  as shown in **Figure 2.7**. Then the sample is immersed into the growth solution facing downwards and the bottle is sealed tightly. The bottle is placed into either a water bath or a microwave heater to maintain a certain growth temperature. For the case of microwave heated samples, an additional adjustable parameter is the microwave power. Without adding any surfactant, the growth is in a 3D mode in  $\text{NH}_3$  environment, resulting in the growth of ZnO rods. Therefore in Chapter 4, where the study of the properties of ZnO nanorods grown in waterbath and microwave are undertaken, the samples are grown as described above.



**Figure 2.7** The setup of microwave heater (CEM Discover), water bath heater (PolyScience) and glass bottle.

(c) Third step: ZnO films coalescence

If ZnO films instead of rods, are desired, a second round of growth is essential. It is almost the same as the first round but the only difference is that there is no  $\text{NH}_3$  in the growth solution. As  $\text{NH}_3$  makes the solution more alkaline, it can promote ZnO to grow out of the plane. Without introducing  $\text{NH}_3$ , the lateral growth will be encouraged, which leads to the coalescence of the rods to achieve a ZnO film. The detail will be discussed in Chapter 5.

(d) Fourth step: post treatment

After the growth is completed, the bottles are taken out of the water bath or microwave heater and cooled down naturally in air to room temperature. Then the samples are taken out from the bottle and rinsed with DI water several times to get rid of the ZnO nanoparticles adsorbed on the surface and blown dry with nitrogen. If necessary, the samples go through thermal annealing under different ambient and temperatures for a certain duration to investigate the intrinsic or external doping properties of ZnO, such as self-diffusion or migration.

### **2.2.2 Growth by pulsed laser deposition**

Although there are many attractive characteristics of aqueous solution methods as discussed in previous session 2.2.1, it is also noted that due to the much lower growth temperatures typically less than  $100^\circ\text{C}$  in the aqueous solution methods, growth units may not have enough kinetic energy to diffuse across the surface to obtain a smooth film. This method is not the perfect choice for applications which requires a smooth film surface or a sharp interface to form heterostructures such as for use in quantum cascade laser. To obtain sharp interfaces, pulsed laser deposition is a good candidate, as it can produce the epitaxial growth of ZnO film with a

smooth surface due to high supersaturation and high nucleation density. In the following section, we will introduce the PLD growth technique.

### **2.2.2.1 Background of PLD**

In 1965, Smith and Turner conducted the first demonstration of PLD using a ruby laser [97]. In the following 20 years, there is no much breakthrough of PLD technique until the high power lasers with sufficiently high pulse energy and short pulse length were introduced together with the successful growth of the high-temperature oxide superconductor films using this technique. In 1987, Venkatesan and Dijkamp demonstrated the superior quality of  $\text{YBa}_2\text{Cu}_3\text{O}_7$  films grown by PLD compared to those grown by other techniques, which made PLD attain its reputed fame and attract wide spread interest all over the world [98]. Up to now, PLD has become an established growth technique for many materials that are normally difficult to be deposited by other methods, especially multi-element oxides. A considerable improvement has been done to scale up the PLD to a large area and to meet industrial needs [99].

### **2.2.2.2 PLD system Setup**

Compared to many other vapor phase deposition techniques, the basic setup of a PLD system is simple as shown in **Figure 2.8**. It consists of an excimer laser source, optics, deposition chamber, load lock chamber, vacuum pumps (mechanical pump and turbo pump), heater and pressure controller.



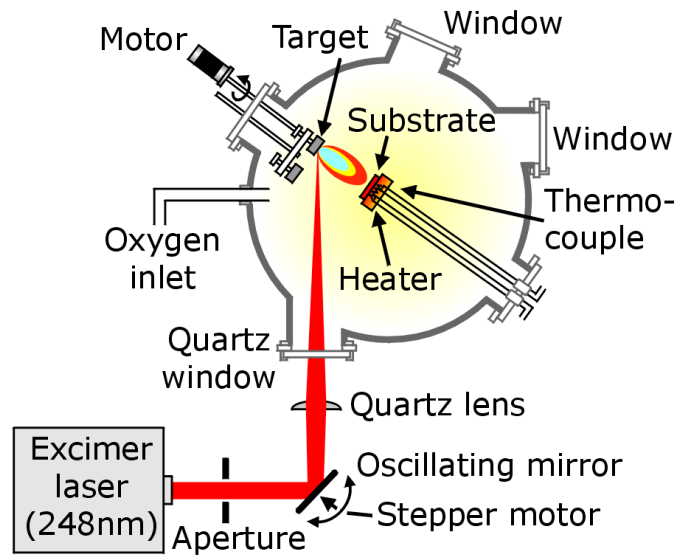


**Figure 2.8** The schematic diagram of a PLD system [100].

### 2.2.2.3 Mechanism of PLD

Compared to the simple setup of the PLD system, the deposition process is complex and involves a wide range of physical phenomena. In general, the thin film is deposited by the ablation of one or more targets irradiated by a focused pulsed-laser beam. The fundamental processes during a PLD experiment will be briefly reviewed in the following [101, 102]:

#### 1) Laser ablation (photon induced sputtering)

Upon the irradiation of the excimer laser ( $\lambda=248$  nm) with a short pulse (pulse duration of 5-40 ns), a strong electromagnetic field, created within the outmost 10nm of the target material, can break the atomic bonds and cause electrons ejected from the bulk material of the penetrated volume. Collisions of these free electrons with the atoms of the bulk material transfer energy to the lattice, which is sufficient for the surface of the target to be heated up to the evaporation temperature.

## 2) Plasma expansion

The localized high temperature at the target surface assists the plasma formation in the form of a plume. Due to the strong Coulomb repulsion from the target surface, the plume expands perpendicularly from the target surface towards a heated substrate. A variety of energetic species, including atoms, molecules, electrons, ions, clusters, particulates and also melted globules, was contained in the plume. The spatial distribution of the plume depends on the background pressure of the PLD chamber. During the expansion of the plume, higher energetic species are slowed down much faster with increment in background pressure.

## 3) Deposition

This stage is critical to the quality of the deposited film. At this stage, the high energetic species ablated from the target impinge onto the substrate surface and induce damage to the surface by sputtering off atoms from the surface. The sputtered species from the substrate and the particles emitted from the target form a collision region, which serves as a source for condensation of particles. When the condensation rate is high enough, a thermal equilibrium can be reached and the film grows on the substrate surface. Once several small clusters are formed through nucleation, subsequent coming particles can directly attach to these clusters. In the same time, there also has possibility that the particles in the clusters dissociate and re-evaporate out. The balance between the competing processes of film growth and dissolution is guided by the Gibbs free energy of the system.

During the PLD process, many growth parameters can be tuned, such as laser parameters ( laser fluence, wavelength, pulse duration and repetition rate), target surface temperature, target to substrate distance as well as background gas and pressure, which have strong impacts on the nucleation and growth of the film. During the pulse duration, the high supersaturation of the

target material occurs on the substrate, which creates a high density of nucleation. The nucleation and growth on the surface of the substrate can be described by models. Similar to other physical vapor deposition methods, three growth modes can take place: three-dimensional island (Volmer–Weber), two-dimensional full monolayer (Frank–van der Merwe), and two-dimensional monolayer growth followed by three-dimensional islands (Stranski–Krastanov) [103]. A smooth surface control of the deposited film down to a sub-monolayer is achievable with PLD depending on the growth rate per laser pulse. Suppose 2 Å per pulse, 5-10 laser pulses are required for the growth of one atomic monolayer [104].

For the study of n-type doping of the ZnO films, the targets used are made of a mixture of Ga<sub>2</sub>O<sub>3</sub> (99.999%) and ZnO (99.999%) powder purchased from Sigma-Aldrich with different atomic percentage to get different doping levels. The mixed powder goes through two cycles of grinding, pressing into 1 inch pellets and annealing in ambient atmosphere at 1250°C for 10 hours. The high-quality and high homogenous target is critical to obtain a high crystalline and smooth film.

The heart of the PLD system is a KrF excimer laser (Lamda Physik Compex 205) with wavelength centered at 248 nm, laser pulse energy of 180 mJ/cm<sup>2</sup>, pulse duration of 25 ns and pulse repetition rate ranging from 1-10 Hz. The laser beam is focused onto the target at an incident angle of 45°. Up to 6 targets can be mounted in the chamber, which can be rotated and chosen for the deposition of heterostructure. The distance between the substrate and target is 8 cm. The background pressure is 5x10<sup>-8</sup> Torr. During the deposition, the oxygen partial pressure can be controlled from 10<sup>-3</sup> to 10<sup>-5</sup> Torr. The substrate temperature can be adjusted from room temperature up to 1000°C monitored by a thermal couple.

#### 2.2.2.4 Comparison between PLD and solution method

Compared to other deposition methods, PLD has other advantages besides the simplicity of the setup. It is a versatile, reliable and fast method. The deposition rate is in the order of tens of nm per min. The thickness can be precisely controlled by the number of pulses applied and complex multi-component materials can be deposited in a wide variety of gas environment over a broad range of gas pressures. The unique ability to synthesize metastable materials and to form films from species existing only in the laser plasma is also among the advantages of PLD.

Compared to the solution method, PLD has fewer impurities involved due to the high vacuum in the chamber, high purity targets (up to 99.999%) used for accurate stoichiometry transfer and position of the energy source for ablation, which is located outside the deposition chamber. PLD is a good candidate to study the doping effect of specific elements [105].

In addition, PLD has the precise control of the doping level, alloy composition ( $x$ , as in  $Zn_xMg_{1-x}O$ ), film thickness as well as the growth modes with the assistance of reflection high-energy electron diffraction (RHEED). By utilizing the 2D growth mode of PLD, the crystal quality of the epilayer can be greatly enhanced. These properties make it suitable to serve our long term objective to grow the MgZnO/ZnO heterostructure for mid-IR quantum cascade laser.

Nevertheless, PLD allows the deposition of all kinds of different materials especially for oxide material, as it can transfer the target stoichiometry into the deposited film accurately and efficiently. Currently, in the solution phase, it is still difficult to get ZnMgO compound; however, there is no bottleneck in PLD deposition. These are the main reasons why PLD is used, instead of the solution method, for the specific piece of work described in Chapter 3, although PLD is relatively high cost as it requires high temperature and high vacuum compared to the solution method.

## 2.3 Characterization of ZnO

### 2.3.1 Field-emission scanning electron microscopy (FESEM)

FESEM is a kind of electron microscopes which provides topographical and elemental information of samples by scanning it with a focused beam of electrons. Being invented for 60 years, FESEM is a fundamental tool widely applied in scientific research nowadays. Benefited from an extremely thin and sharp tungsten needle as a cathode, FESEM is able to achieve a high spatial resolution, less electrostatically distorted images compared to convention SEM. Compared to an optical microscope, the FESEM can provide a better resolution since the electron beam has a much shorter wavelength (de Broglie wavelength) compared to that of light. The principle of FESEM is schematically illustrated in **Figure 2.9**. The electrons in the beam are accelerated from a field-emission cathode after experiencing the voltage difference between the anode and cathode (0.1 keV to 50 keV). Focused by condenser lenses and passing through pairs of scanning coils or pairs of deflector plates, the primary beam of electrons scans the surface of the sample. A large variety of signals are emitted during the electron-specimen interactions of which the important ones are back-scattered electrons, secondary electrons, characteristic X-rays, cathodoluminescence, and transmitted electrons. As low-energy (<50 eV) secondary electrons originate from sample surface and a few nanometers underneath, the angle and velocity of secondary electrons are determined by the surface structure of the sample. Thus, in the most common imaging mode, the secondary electrons are detected and utilized to construct images. As the number of backscattered electrons is related to the atomic number of the surface element, backscattered electrons are able to finger print each element.

In this work, the JEOL FESEM 6700 in Institute of Materials Research and Engineering was used to examine the surface morphology, length and diameter of ZnO nanorods and thickness of ZnO films. The resolution of the system could reach 30nm. The acceleration voltage applied is in the range of 5 to 30 kV. The working distance (WD) is set at 6 mm/8 mm by taking into consideration the attainable resolution, depth of field, sample tilt and local electric field. For non-conductive samples, surface charging effect could be minimized through lower acceleration voltage (lower contrast) or Au coatings.

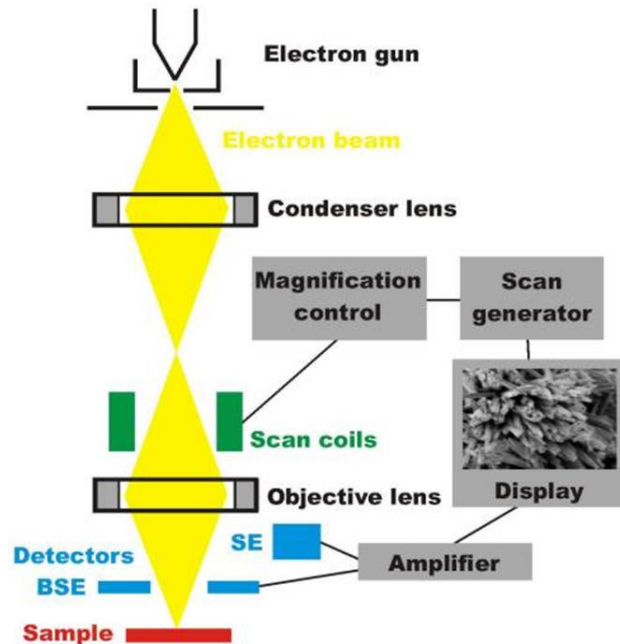


**Figure 2.9** The schematic diagram of FESEM from reference [106].

### 2.3.2 Photoluminescence spectroscopy (PL)

PL results from the spontaneous emission of photons from a material under optical excitation. The electrons are excited to a higher energy state by external light and then return to a lower energy state with the emission of a photon. The photon energy is determined by the energy

difference between the excited electron state and equilibrium state. The intensity of the peak, correlating to the number of photons re-radiated from the material, depends on the population of the states which correspond to the transitions and the efficiency of the recombination process. It is a nondestructive and sensitive fluorescent measurement. Thus, this characterization tool is intensely used in this thesis to investigate a variety of ZnO parameters, such as the identification of the impurity levels and quality of the surfaces.

Basic photoluminescence properties of ZnO are exhibited in the two main emission bands for both solution and PLD grown ZnO: the UV emission band and a visible emission band. Many possible radiative recombination mechanisms take place in these two bands. For the UV band emission, it is mainly from band-edge recombination of excitons and their phonon replicas, which is usually named as near band edge (NBE) emission. The visible band emission, which results from defects or impurities states located in the band gap of ZnO, is also referred to as deep-level emission (DLE). The maximum intensity usually occurs in the green to yellow range of the spectra.

### **2.3.2.1 Band structure of ZnO**

As shown in **Figure 2.10**, ZnO is a direct bandgap semiconductor, where the minimal-energy state in the conduction band (CB) and the maximal-energy state in the valence band (VB) hold the same crystal momentum ( $k=0$ ) located at the center of the Brillouin zone  $\Gamma$  point. At room temperature, ZnO has a bandgap ( $E_g$ ) of 3.37 eV, which is defined as the energy difference between the conduction band minimum and the valence band maximum.

The conduction band minimum is formed by the empty 4s states of  $\text{Zn}^{2+}$  or the antibonding  $sp^3$  hybrid states with an electron effective mass of  $m_e = 0.24m_0$  [107]. The valence band maximum consists of the 2p orbital or the bonding in  $sp^3$  orbitals of the  $\text{O}^{2-}$ . The valence band is split into three two-fold degenerate sub-bands, A, B and C due to the hexagonal crystal field and the spin-orbit interaction. The most well adopted valence band symmetry ordering is A- $\Gamma_7$ , B- $\Gamma_9$ , and C- $\Gamma_7$  [108]. The effective mass of holes in ZnO is  $0.59m_0$  for A and B bands, but is anisotropic in C bands with value of  $0.31m_0$  and  $0.55m_0$  for the wave vector perpendicular and parallel to the c-axis, respectively.

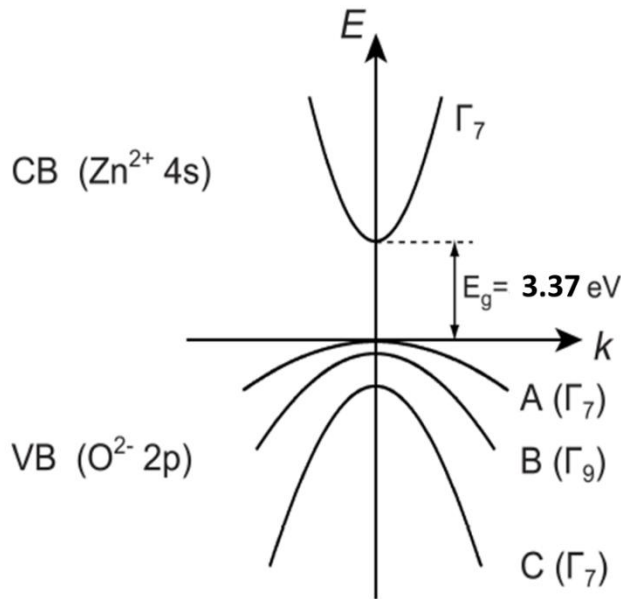


**Figure 2.10** Schematic band structure of ZnO.

An understanding of the origins of NBE and DLE are necessary to interpret the results of luminescence characteristics of ZnO presented in chapters 4 and 5.



### 2.3.2.2 Band edge emission

Free excitons (FXs), excitons bound to acceptors and donors, and their two-electron satellite states, and donor–acceptor pairs as well as phonon replicas usually participate in the band edge emission as illustrated in **Figure 2.11**. The nature of these excitons will be discussed below.

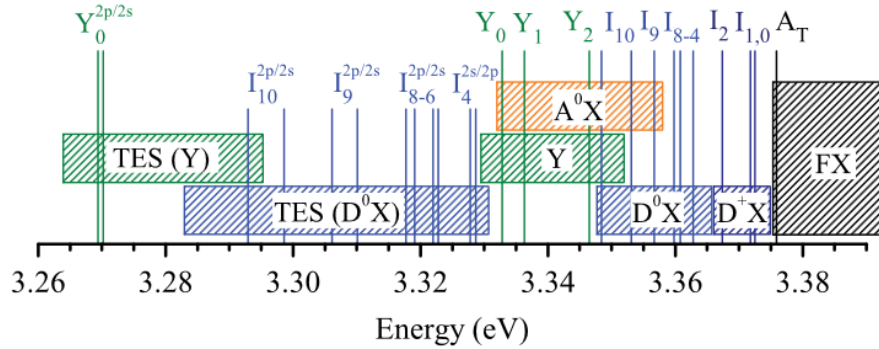


**Figure 2.11** Free and bound exciton recombination in the PL spectra of ZnO band edge emission region [107]. Selected transitions are indicated by vertical lines. The different areas mark the energy range of free excitons (FX), ionized donor bound excitons ( $D^+X$ ), neutral donor bound excitons ( $D^0X$ ), acceptor bound excitons ( $A^0X$ ), deeply bound excitons (Y), and two electron satellites (TES) of shallow and deeply bound excitons in their 2s and 2p states [109].

### 2.3.2.3 Free excitons

When ZnO is excited by a light source with photon energy higher than or equal to its band-gap energy, an electron is excited into the conduction band and a hole is left in the valence band. Due to the Coulomb attraction, this electron and hole are bound together as a pair named exciton. The free excitons are charge neutral. Energy state of exciton could be expressed by the Schrödinger equation given below [110]:

$$\left( -\frac{\hbar^2}{2m_e} \nabla_e^2 - \frac{\hbar^2}{2m_h} \nabla_h^2 - \frac{e^2}{4\pi\epsilon r_{eh}} \right) \psi_{ex} = E_{ex} \psi_{ex}, \quad (2.9)$$

where  $m_e$  and  $m_h$  are electron and hole effective mass, respectively,  $\epsilon$  is the dielectric constant of ZnO,  $r_{eh}$  is the distance between electron and hole,  $E_{ex}$  is the eigenvalue of the energy. By solving equation (2.9), the quantized energy states of the exciton can be obtained:

$$E_{ex}(n, k) = E_g - \frac{1}{n^2} \frac{\mu}{m_0 \epsilon_r^2} R_y + \frac{\hbar^2 k^2}{2m_{eh}}, \quad (2.10)$$

where  $E_g$  is the bandgap of ZnO,  $R_y$  is the Rydberg unit of energy ( $R_y=13.61$  eV),  $\mu$  is the reduced mass of excitons  $\frac{m_e m_h}{m_e + m_h}$ ,  $m_{eh}$  is the total exciton mass  $m_{eh} = m_e + m_h$ ,  $\hbar$  is the Planck constant,  $\epsilon_r$  is the relative permittivity.

As illustrated in **Figure 2.12**, the energy levels of exciton are quantized, and all fall below that of the free electron. The energy difference between unbound electron-hole pair and free excitons are known as exciton binding energy  $E_{ex}^b$ , which are given by:

$$E_{ex}^b = \frac{\mu}{m_0 \epsilon_r^2} R_y. \quad (2.11)$$

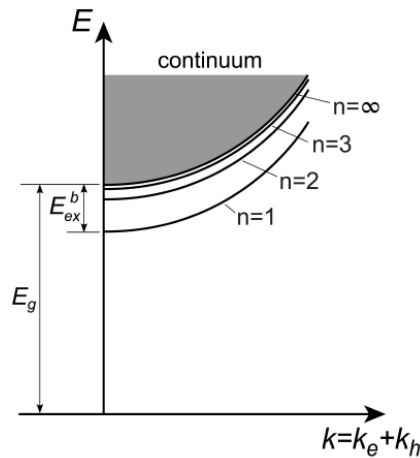


**Figure 2.12** Exciton energy levels with respect to quantum number  $n$  [111].

ZnO has a high exciton binding energy (60 meV) which is much higher than the thermal energy at room temperature (25 meV). As excitons in ZnO are stable at room temperature, ZnO has a high excitonic luminescence efficiency. The free exciton peak observed in the room temperature PL can be deduced from equation (2.10).

### 2.3.2.4 Bound excitons

Bound excitons refer to those free excitons being trapped in the defects centers, such as donor or acceptor. So it can be classified as donor bound excitons and acceptor bound excitons. Depending on the charge state of the donor or acceptor, they can form different kinds of bound exciton complexes, such as neutral donor bound excitons ( $D^0X$ ), neutral acceptor bound excitons ( $A^0X$ ), and ionized donor/acceptor bound excitons ( $D^+X/A^-X$ ), as shown in **Figure 2.13**.

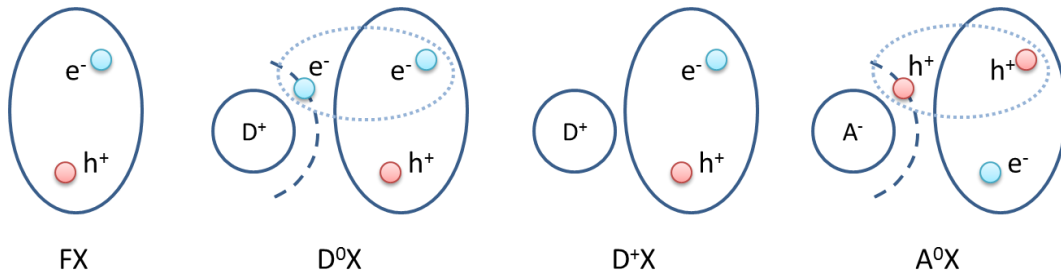


**Figure 2.13** Illustration of free exciton (FX), neutral donor bound excitons ( $D^0X$ ), ionized donor bound excitons ( $D^+X$ ) and neutral acceptor bound excitons ( $A^0X$ ).

The excitons bound to ionized acceptors are not stable in general. For the case of neutral donor bound exciton ( $D^0X$ ), sometimes during the process of recombination, the donor is possible to be excited to an ionized state, and the emitted photon energy is smaller than the normal  $D^0X$

emitted photon by the energy difference between the donor excited state and its ground state. This transition is known as two electron satellites (TES).

The emission from neutral DBE, LO phonon replicas and also TES dominate the near-band-edge emission of ZnO at low temperatures, where 11 peaks (denoted I<sub>0</sub>-I<sub>11</sub>) in Figure 2.11 could be identified. An illustration of the bound excitons peaks in the low temperature PL measurement of ZnO is shown in **Figure 2.14**. As the temperature increases, the bound excitons start to release and gradually disappear above 80K while the free exciton emission becomes the main contributor at higher temperatures.

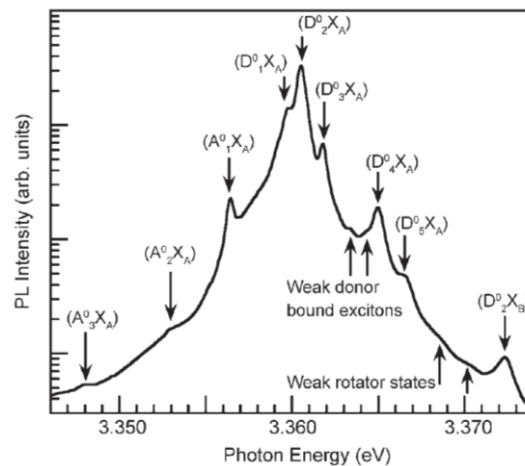


**Figure 2.14** Bound-excitonic region of the PL spectrum of annealed ZnO substrate measured at 10 K [112].

### 2.3.2.5 Deep level emission

Besides the band edge emission, the emissions of ZnO from visible and infrared spectral regions (1.6 - 2.8 eV) are often observed. They are attributed to the deep levels inside ZnO bandgap due to intentionally dopant, Li, N, Cu as well as intrinsic defects, such as oxygen and zinc interstitials

and vacancies as discussed in section 1.3. **Figure 2.15** represents a DLE spectrum of one of the ZnO samples measured at 20 K as an example. The broadness of the DLE band is due to the superposition of various deep levels emission.

Numerous assignments of the defects-related luminescence bands are reported in literature, some of which are still controversial. One example is the green emission which is the most commonly observed defect emission in ZnO thin film as well as in ZnO nanostructure. Green emission is assigned to oxygen vacancies, but other hypothesis includes antisite oxygen, zinc interstitials, copper impurities, and donor-acceptor transitions. Yellow emission due to oxygen interstitials is widely accepted, although Li impurities also have been proposed as the origin of the yellow emission in ZnO. Besides, yellow and green emissions, orange-red emissions are also observed which was attributed to oxygen interstitials as well as surface dislocations [113].

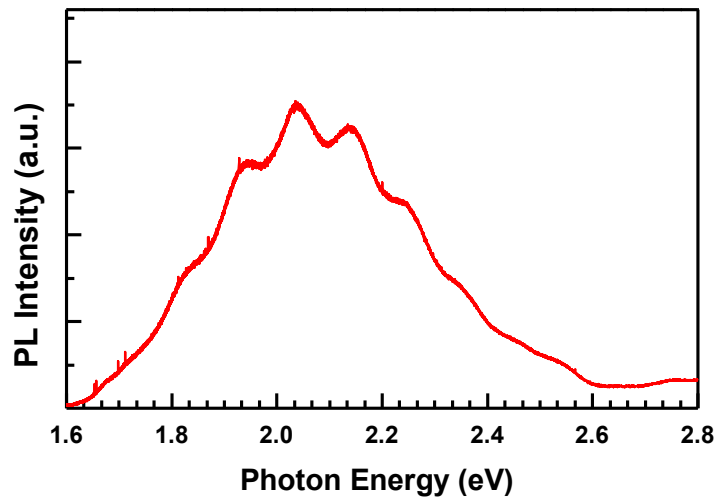


**Figure 2.15** The DLE spectrum of ZnO nanorods by solution method with 0.02 M zinc acetate, 0.6 ml ammonia and 20ml H<sub>2</sub>O at 90°C for 20 minutes.

The visible emission could be effectively controlled by performing thermal annealing. Thus, post-annealing is a good way to reduce the defects densities and improve the quality of material.

Various annealing ambient and temperatures are adopted to identify the origin of the defects emission. Chapter 4 of this thesis will focus on the study of DLE of the ZnO nanorods and the effect of thermal annealing in vacuum on the origin of the DLE.

In this project, the PL is routinely used to check the ZnO crystal quality, strain induced bandgap shift and defects. The PL system used in this work is Renishaw 2000. A helium-cadmium (He-Cd) laser centered at 325 nm (3.81 eV) is used as the excitation source which emits the photons of energy greater than ZnO bandgap. Thus, ZnO can be excited non-resonantly. The penetration depth into ZnO is around 60-70 nm [114]. The system is under back scattering configuration and the scan range of the spectrum is from 350 nm to 800 nm. A spectral resolution of 0.03 nm can be achieved. The laser spot size on the sample is 4-6  $\mu\text{m}$ . For the low temperature PL, the sample is mounted in the cryostat and attached to a cooling tube through a copper stage. An external helium gas condenser and a pump are connected to the cooling tube, which enables the cryostat to reach 15 K. A thermal couple and pressure meter are used to monitor the temperature and vacuum level inside the cryostat.

### **2.3.3 X-ray photoelectron spectroscopy (XPS)**

XPS, also named as electron spectroscopy for chemical analysis (ESCA), is a surface sensitive technique to investigate the stoichiometry of the surface. The basic working principle of the XPS is the photoelectric effect enunciated by Einstein in 1905 [115]. The ZnO sample is irradiated with monoenergetic soft x-rays which are absorbed by the outmost atomic layers (0-10 nm). The absorbed energy excites the electrons in the core levels of atom to transit to vacuum level as illustrated in **Figure 2.16**, becoming photoelectrons with a certain kinetic energy. By measuring the number of the electrons as a function of kinetic energy, a photoelectron spectrum can thus be

obtained for all the elements except H and He. The system is usually operated in an ultrahigh vacuum environment ( $P < 10^{-9}$  millibar)

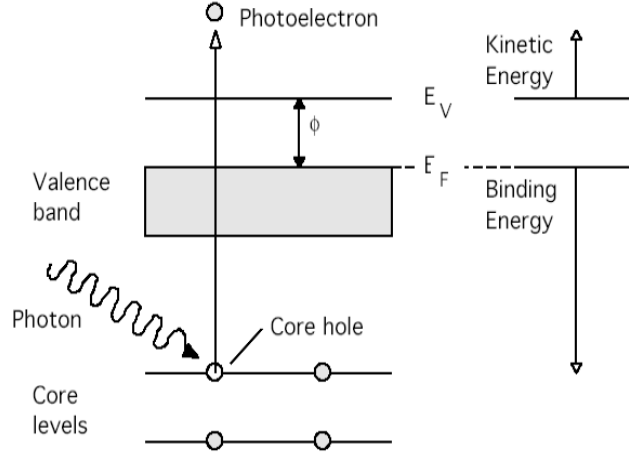


**Figure 2.16** Schematic diagram showing the working principle of XPS.

If the excitation X-rays has a photon energy of  $h\nu$ , based on the conservation of energy, the kinetic energy  $KE(e^-)$  of the photoelectron can be expressed as [116]:

$$KE(e^-) = h\nu - [E(A^+) - E(A)], \quad (2.12)$$

where  $[E(A^+) - E(A)]$  is the difference in energy between the ionized and neutral state of the atom, which is identified as the binding energy (BE) of photoelectrons.

By measuring the  $KE(e^-)$ , the BE of the photoelectron can be obtained:

$$KE(e^-) = h\nu - [E(A^+) - E(A)] - \phi + \delta, \quad (2.13)$$

where  $\phi$  is the spectrometer work function which refers to the minimum energy an electron needs to have in order to escape from the sample surface and  $\delta$  is the peak shift due to surface charging.  $\phi - \delta$  should be zero in a well calibrated system.

In this work, we used the VG ESCA LAB-220i XL XPS system in IMRE, as shown in **Figure 2.17**. It uses monochromatic aluminum  $K\alpha$  X-rays as the excitation source, which has photo-energy of 1486.6 eV and spot size of 700  $\mu\text{m}$ . The incident angle and analysis angle are 37.5 degree and 90 degree to the sample surface, respectively. The resolution for the BE can reach 0.02-0.03 eV in the range of 0 to 1000 eV. Pure Au, Ag and Cu are commonly used to calibrate the XPS BE through setting Au  $4f_{7/2}$ , Ag  $3d_{5/2}$ , and Cu  $2p_{3/2}$  at binding energies of 83.98, 368.26, and 932.67 eV, respectively [117]. It is also equipped with an in-situ annealing stage in the ultra-high vacuum (UHV) chamber and an ion beam etching stage for surface contamination removal or depth profiling. In this thesis, the XPS was mainly used to study the stoichiometry of ZnO samples as well as oxygen and zinc defects inside the ZnO nanostructures synthesized by microwave assisted heating and conventional water bath.

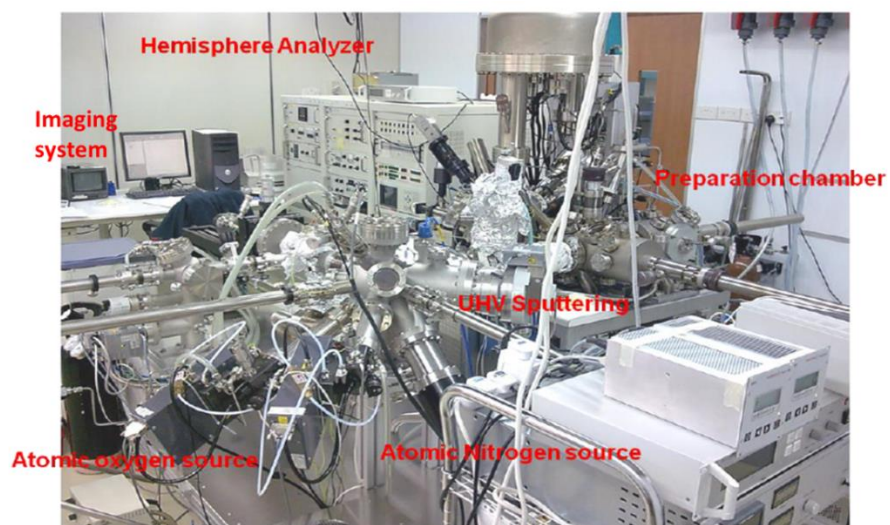


**Figure 2.17** Main components of VG ESCA LAB-220i XL XPS setup in IMRE.



The XPS chamber, with a base pressure of  $1 \times 10^{-10}$  Torr, was directly connected to a VG ESCA 220i-XL imaging XPS system, the specific place of interest in ZnO samples can be visualized and located. The chemical states of each element from the ZnO samples were analyzed through the binding energy position. If the ZnO samples are not conductive, electron emission from the surface of the sample may cause positive sample charging, known as surface charging, which results in the shift and broadening of the binding energy. In order to minimize surface charging effect, an electron-flood gun was introduced to compensate the photoemission charge on the sample surface. In this work, the criteria of optimizing the electron-flood gun setting is to maximize the peak intensity and minimize the FWHM of the peaks simultaneously [118]. Besides neutralization by electron-flood gun during the measurement, the XPS spectrum still requires to be aligned to the C 1s binding energy at 285.0 eV at the analysis stage with the help of Thermo Avantage software. In order to determine the stoichiometry of the ZnO sample, the individual integrated peak areas ( $I_i$ ) are divided by their respective atomic sensitivity factor ( $S_i$ ) and normalized to 100% to get an atomic fraction of element A,  $C_A$  by  $C_A = \frac{I_A/S_A}{\sum I_i/S_i}$  [119]. For ZnO samples, the O 1s (530 eV) and Zn 2p<sub>3/2</sub> (1022 eV) peaks are with relative sensitivity factors (RSF) of 0.66 and 4.8, respectively [120].

## **2.3.4 Terahertz time-domain spectroscopy (THz-TDS)**

### **2.3.4.1 Background of THz-TDS**

Terahertz spans the wavelength range from infrared to microwave radiation (0.3 to 20 THz), which was a mystery for researchers for several decades. With breakthroughs in materials science and engineering, modern terahertz spectroscopy systems are able to flourish. In turn,

terahertz spectroscopy has become a powerful tool for applications in a diverse range of fields such as biomedical sciences, tomographic imaging, astronomy and analytical science, characterization of semiconductors and biomolecules [121, 122].

The development of THz-TDS is spurred by ultrafast optoelectronics using low temperature GaAs and electro-optic crystals [123]. First sub-picosecond pulse triggering semiconductor switch is used to drive a dipole antenna, generating picosecond microwave pulses in free space [124]. With shorter laser pulses, higher electromagnetic radiation is achievable with smaller radiating structures made using VLSI lithography [124]. The invention of terahertz beams which can be collimated and focused as simply as light beams in a spectrometer is another big milestone in THz-TDS history. Several reviews about THz-TDS and THz technology could be found in literature [125, 126]

#### **2.3.4.2 Applications of THz-TDS**

Three decades after the invention, THz-TDS has developed into a powerful characterization technique that can give insightful information on free carriers transport and dielectric properties of semiconductor materials [127, 128]. The pivotal advantage of THz-TDS lies in the fact that the amplitude and phase of the spectral components can be obtained simultaneously. It is also noninvasive, dispensed with the need of making electrical contacts, and has a high signal-to-noise ratio benefiting from the coherent synchronous detection scheme [129]. The technique has been used to characterize transport property as well as dielectric response of various semiconducting materials, such as n-ZnO films and rods [130, 131], Si nanowires [132], InGaN film [133], GaAs [134], CdS nanobelts [135], and Bi (001) ultra-thin films [136].

### 2.3.4.3 THz-TDS setup

The schematic diagram of THz-TDS used to explain its basic working principles is shown in **Figure 2.18**. A femtosecond pulse generated from a laser source was beam split into pump pulses and gating pulses. The pump pulses were impinged onto a photoconductive antenna, which was patterned on a low temperature grown GaAs (LT-GaAs) to generate THz pulses. There is an instantaneous photo-induced current change in semiconductor materials after being illuminated by fs laser pulses. The sudden change in current results in the electromagnetic radiation. Due to the short carrier lifetime of LT-GaAs, the duration of the emitted THz pulses is only around 2 ps. This emitted short THz pulses were collimated and focused onto the sample by a pair of off-axis paraboloidal mirrors and then directed to the photoconductive detector. On the other hand, the gate pulse was used to detect the THz pulses. The working mechanism of the detector is similar to that of emitter but no bias was applied to the antenna. When gate pulses illuminated the detector, photo-carriers were generated at the surface of the semiconductor. The electric field associated with THz wave drive these photo-generated carriers to the electrodes resulting in a current flow. After the current was further amplified, it was recorded as the corresponding THz electric field. Due to the short lifetime of LT-GaAs carriers, only an extremely narrow region of the entire THz electric field signal was sampled. A delay stage was introduced to delay the gate pulse which controls the temporal overlap between the THz wave and gate pulse. By varying the delay time, which was the gating time of the detector, the real time electric field signal of the THz wave transmitted through samples was collected.

In this thesis, THz transmission spectra of ZnO films doped with different carrier concentrations were obtained from TeraView TPS3000 THz-TDS system, which contains a mode-locked Ti:sapphire laser generating ~100 fs pulses centered at 800 nm with a repetition rate of 76 MHz.

The entire experiment setup was kept in dry nitrogen ambient to eliminate noise caused by water vapor absorption. As mentioned, during the THz-TDS measurement, the THz pulse passes through the ZnO samples and the time domain electric field of the transmitted THz signal  $E(t)$  is obtained. In order to obtain transmission properties in frequency domain, Fourier transform on  $E(t)$  needs to be applied based on the equation  $E(\omega) = \frac{1}{2\pi} \int_{-\infty}^{+\infty} e^{-i\omega t} E(t) dt$ . Further discussion on the application of this technique is presented in Chapter 3.

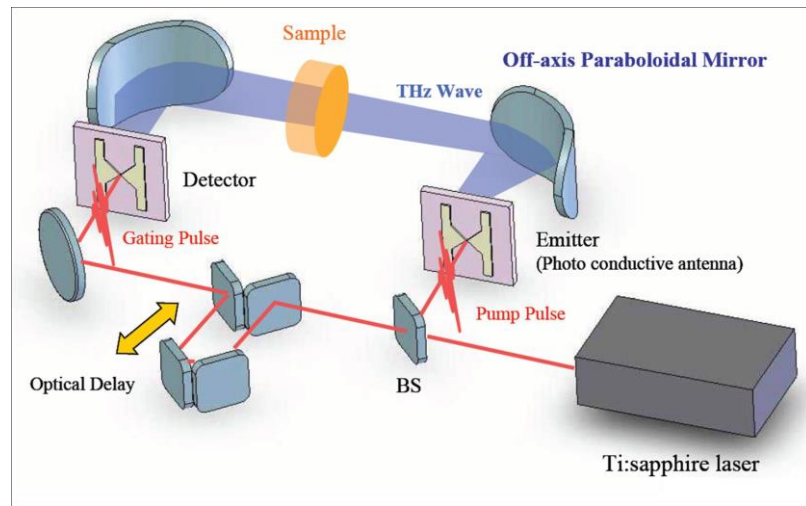


**Figure 2.18** Schematic diagram of THz-TDS setup, adopted from [137].

# **Chapter 3 THz-TDS characterization of n-type ZnO:Ga grown by PLD**

## **3.1 Introduction**

This chapter focuses on an integrated technique using THz TDS and Hall measurement to obtain the effective mass and scattering time of n-type Ga-doped ZnO film. Firstly, a theoretical background of transmission coefficient and the Drude model are given to understand the new method in deriving effective mass and scattering time. The preparation of the n-type ZnO films by PLD with different carrier concentrations and the experimental setups used in this work will be described. The results of the carrier concentration dependent effective mass, scattering time as well as mobility obtained from this new method will be presented. Lastly, the physics behind the discrepancy in the carrier mobility extracted from Hall and THz-TDS measurements will be explained.

## **3.2 Background**

Effective mass  $m^*$ , carrier concentration  $N_0$ , and scattering time  $\tau$  are important parameters to characterize the free carriers transport properties in semiconductors. Recently THz-TDS has been developed as a powerful characterization technique that can give insightful information on free carriers transport and dielectric properties of semiconductor materials as discussed in section 2.3.4. However, in the conventional THz-TDS characterizations, the carrier effective mass, which is a key parameter in extracting dielectric properties from THz transmission/reflection measurements, is assumed as a constant and its dependence on the carrier density is completely

ignored. In fact, as a fundamental parameter in semiconductor physics, the electron effective mass (which is determined by the curvature of the  $E-k$  diagram) has a substantial influence on other physical quantities, such as density of states, carrier density, current and mobility [138]. Effective mass is also crucial in devices structure design, which determines the electron/hole energy levels of heterostructure. Unfortunately, THz-TDS alone is not sufficient to determine the carrier effective mass independently as it only provides two quantities (i.e. amplitude and phase), unless an additional excitation source is introduced, such as in terahertz time-domain magneto-optical ellipsometry [139].

In this chapter, we present a new and easily accessible approach to determine carrier concentration dependent effective mass and carrier scattering time by THz-TDS. The derivation of electron effective mass for n-ZnO with different carrier concentrations is illustrated as an example and the method can be applied to other semiconductors. By utilizing the carrier concentration value obtained from Hall measurement and manipulating the parameters of carrier dynamic extracted from THz-TDS through a single-variable linear curve fitting, the electron effective masses of n-ZnO films with different carrier concentrations are obtained, which show a positive correlation with carrier concentration. The carrier concentration dependent character is attributed to the non-parabolicity of the conduction band.

### 3.3 Theoretical model

#### 3.3.1 Transmission coefficient

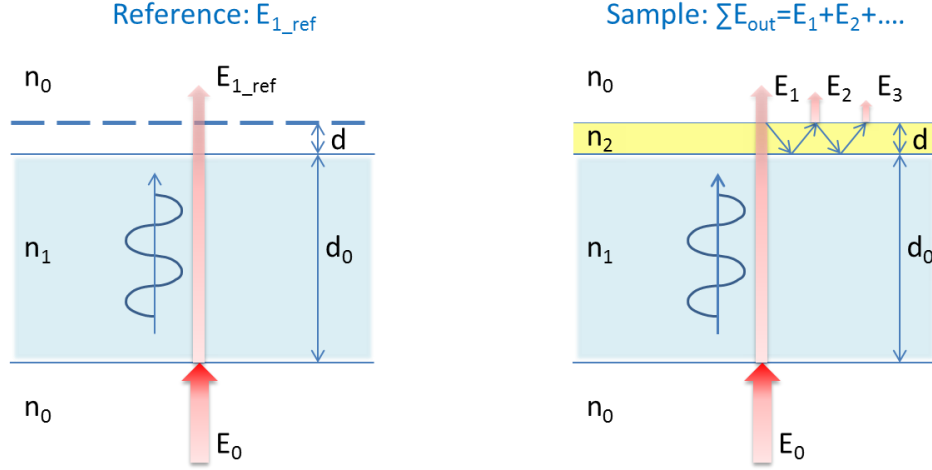


**Figure 3.1** Schematic diagram of the THz signal transmitted through bare sapphire substrate (reference) and sample with ZnO film on top of it.

As shown in **Figure 3.1**, when the THz wave is transmitted through the sapphire substrate, the transmittivity from air to sapphire and from sapphire to air is denoted as  $t_{01}$  and  $t_{10}$ ,

$$t_{01} = \frac{2n_0}{n_1 + n_0}, \quad t_{10} = \frac{2n_1}{n_1 + n_0}, \quad (3.1)$$

The electric field after passing through the bare sapphire substrate (reference) and the thickness  $d$  of air could be expressed as:

$$\vec{E}_{1\_ref} = \vec{E}_0 \times t_{01} \times t_{10} \times e^{i\omega \frac{n_1 d_0 + n_0 d}{c}}, \quad (3.2)$$

Where  $\vec{E}_0$  is the amplitude of the electromagnetic field of the incident beam. Due to the different refractive indices of ZnO film and sapphire substrate, reflection occurs at the interface. The

reflectivity at the ZnO/air interface and ZnO/sapphire interface are respectively given by  $r_{20}$  and  $r_{21}$  is:

$$r_{20} = \frac{n_2 - n_0}{n_2 + n_0}, \quad r_{21} = \frac{n_2 - n_1}{n_2 + n_1}, \quad (3.3)$$

As the electric field can be reflected at the ZnO/sapphire as well as the ZnO/air interfaces, we denote the electric field emerging from the ZnO surface after the first and successive reflections at the ZnO/sapphire interface as  $\vec{E}_1, \vec{E}_2, \vec{E}_3, \dots$ . The electric field  $\vec{E}_1$  at the top surface of the ZnO on sapphire substrate is given by:

$$\vec{E}_1 = \vec{E}_0 \times t_{01} \times t_{12} \times t_{20} \times e^{\frac{i\omega n_1 d_0 + n_2 d}{c}}, \quad (3.4)$$

The electric field  $\vec{E}_2$  at the top surface of the ZnO on sapphire substrate is given by:

$$\vec{E}_2 = \vec{E}_0 \times t_{01} \times t_{12} \times r_{20} \times r_{21} \times t_{20} \times e^{\frac{i\omega n_1 d_0 + 3n_2 d}{c}}, \quad (3.5)$$

The total electric field for the sample with ZnO film on top of sapphire substrate is the sum of the geometric progression, and thus can be expressed as:

$$\sum \vec{E}_{out} = \frac{\vec{E}_1}{1 - q} = \frac{\vec{E}_0 \times t_{01} \times t_{12} \times t_{20} \times e^{\frac{i\omega n_1 d_0 + n_2 d}{c}}}{1 - r_{20} \times r_{21} \times e^{\frac{2n_2 d}{c}}}, \quad (3.6)$$

Transmission coefficient  $t(\omega)$  is defined as the ratio of the transmitted THz electrical field through the n-ZnO film, denoted by  $E_{sam}(\omega)$  to that through the bare sapphire substrate reference  $E_{ref}(\omega)$ . The coefficient is obtained by substituting the expressions in equations (3.2) and (3.6),



$$t(\omega) = \frac{\bar{E}_{sam}(\omega)}{\bar{E}_{ref}(\omega)} = \frac{\sum \bar{E}_{out}}{\bar{E}_{1-ref}} = \frac{2n_2(n_s + 1)\exp[i\omega(n_2 - 1)d/c]}{[(1 + n_2)(n_2 + n_s) + (n_2 - 1)(n_s - n_2)\exp(2i\omega n_2 d/c)]}. \quad (3.7)$$

### 3.3.2 Drude model

Drude model is a classical model used to calculate the motion of electron and dielectric function of a material. In Drude model, the motion of electron simply follows classical mechanics, i.e., Newton's law, while all the quantum mechanics behavior of an electron is represented by the effective mass used, instead of real mass of an electron. The electrons in metal or semiconductors move under the influence of an electric field. Under the influence of an external electric field, an electron is displaced from its original place by a distance  $\bar{r}$ . Considering an electromagnetic wave  $\bar{E} = E_0 e^{-i\omega t}$  with amplitude  $E_0$  and frequency  $\omega$  impinging onto a semiconductor, the equation of motion of the electron gas as following:

$$m^* \frac{\partial^2 \bar{r}}{\partial t^2} + m^* \Gamma \frac{\partial \bar{r}}{\partial t} = eE_0 e^{-i\omega t}, \quad (3.8)$$

where  $m^*$  is the effective mass of free electrons,  $\Gamma$  is the collision coefficient of electrons resulting in the damping of the motion. Considering harmonic motion of electrons given by the expression  $\bar{r}(t) = \bar{r}_0 e^{-i\omega t}$ , the above equation yields:

$$\bar{r}_0 = \frac{e\bar{E}_0}{-m^* \omega^2 - im^* \omega \Gamma}, \quad (3.9)$$

The displacement of electron from its original position results in a dipole moment  $\mu = e\bar{r}$ . The cumulative effect of the dipole moment from all the electrons results in a polarization  $\bar{P} = n e \bar{r}$ , where  $n$  is the electron concentration. It is well known that polarization is also defined as:

$\vec{P} = \varepsilon_0 \chi_e \vec{E}$ , where  $\chi_e$  is the susceptibility of a material. As  $\vec{D} = \varepsilon_0 \varepsilon \vec{E} = \varepsilon_0 \vec{E} + \varepsilon_0 \chi_e \vec{E}$ , the dielectric function of a material  $\varepsilon = 1 + \chi_e$ . Thus,

$$\begin{aligned} \varepsilon(\omega) &= 1 + \chi_e = 1 + \frac{ne\vec{r}}{\varepsilon_0 \vec{E}} = 1 - \frac{ne^2}{\varepsilon_0 m^* (\omega^2 + i\omega\Gamma)} \\ &= 1 - \frac{\omega_p^2}{\omega^2 + i\Gamma\omega} = 1 - \frac{\omega_p^2}{\omega^2 + \Gamma^2} + i \frac{\Gamma\omega_p^2}{\omega(\omega^2 + \Gamma^2)} \end{aligned} \quad , \quad (3.10)$$

where  $\omega_p = \sqrt{ne^2 / (\varepsilon_0 m^*)}$  is the volume plasma frequency.

### 3.4 Samples preparation and experimental details

As mentioned in Chapter 1, ZnO has the large bandgap of 3.37eV at room temperature and on top of that ZnO/MgZnO heterostructures have a large band offset, thus it is a good candidate for inter-subband (ISB) devices. Especially recently ZnO has been proposed as a promising material mid-IR ISB quantum cascade laser (QCL) and photodetector operating at room temperature since the invention of GaAs/AlGaAs QCL 20 years ago. Compared with QCL in mid-infrared using GaAs/AlGaAs system, ZnO/MgZnO exhibits a weaker temperature dependence of the population inversion due to large ZnO optical phonon energy of 72 meV [140]. Comparing to III-V materials such as GaN, ZnO-based structures has a larger ionicity and results in shorter carrier lifetime and faster ISB carrier relaxation, which benefits ZnO-based ISB devices for high speed applications. Furthermore, the higher effective mass of ZnO compared to GaN ( $0.19m_0$ ) could reduce the dark current and improve the sensitivity of ISB detectors [129]. Effective mass is a fundamental parameter which determines many other physical characteristics of a material and it is also crucial in devices designing such as QCL and photodetector, since electron energy levels in ZnO/MgZnO QWs are sensitive to effective mass. From the perspectives of both

fundamental physics and device applications, it is greatly desired to know the electron effective mass of ZnO and its dependence on carrier concentration.<sup>18-20</sup> To serve this purpose, gallium doped n-ZnO films with different carrier concentrations were investigated in this work. Two ZnO films with different carrier concentrations were grown on c-plane sapphire substrate by pulsed laser deposition (PLD) as described in Chapter 2 and the specific growth condition for this work is shown below.

- A target of ceramic ZnO/Ga<sub>2</sub>O<sub>3</sub> (98/02 wt.%) with 99.99% purity.
- A 20 Hz pulsed laser with pulse energy of 300 mJ was focused onto the target and the target-substrate distance was 8 cm.
- Oxygen partial pressure varies from 4.2mTorr to 7mTorr.
- Substrate temperature changes from 300°C to 800°C.

The thicknesses of ZnO samples 1 and 2 were 490 nm and 550 nm respectively as measured from the micrographs obtained with a FESEM. The carrier transport properties of the two as-grown samples were measured by four-point probe Hall measurements (HL5500PC Hall Effect System) at room temperature using van der Pauw configuration. Ti/Au (15 nm/50 nm) was used as an ohmic contact to n-ZnO films to minimize contact resistance. The electron concentrations for samples 1 and 2 were found to be  $4.0 \times 10^{19} \text{ cm}^{-3}$  and  $4.3 \times 10^{18} \text{ cm}^{-3}$ , and their mobilities were  $20.1 \text{ cm}^2/\text{Vs}$  and  $22.8 \text{ cm}^2/\text{Vs}$ , respectively.

The THz transmission spectra of the two as-grown ZnO samples were characterized by a THz-TDS system as described in section 2.3.4.

### 3.5 Results and discussion

**Figures 3.2(a)** and (b) show the THz signals in time-domain and their corresponding Fourier-transformed frequency domain spectra, respectively, after passing through the bare sapphire substrate, samples 1 and 2. The time-domain window was truncated such that additional pulses originated from multiple reflections from sample-air interfaces were not included in analysis and the curves in time domain have been shifted horizontally for easy observation. The transmitted THz signal through the bare sapphire substrate served as a reference throughout the whole experiment. It clearly shows that the transmitted signal through the reference has the highest amplitude compared to that of ZnO samples 1 and 2, as the intrinsic substrate barely absorbs the THz energy.

It is worth to mention that as the investigated ZnO films are thin, special precautions were taken during THz-TDS characterization to minimize the systemic errors. The thickness variation of sapphire substrates is normally on the same order or larger than the thickness of ZnO films investigated, which may undermine the validity of measurement results. To eliminate this effect, the THz transmission properties of the sapphire substrates on which the ZnO were to be grown were measured first. After ZnO films deposition, THz-TDS was performed again to measure the transmittance of the same sapphire deposited with ZnO. To minimize the effect of THz-TDS system instability, which was mainly caused by the inaccuracy and non-perfect repeatability of the delay line stage, ZnO deposition and THz-TDS re-measurement, was performed within three days after the THz-TDS characterization of the bare sapphire substrates. A control sapphire sample (cut from the adjacent area to those used for growing the ZnO films) introduced to monitor the variation in the two time-separated THz-TDS measurements, indicated a relative

error of less than 5% caused by the system instability in amplitude and phase of the Fourier-transformed THz waves.

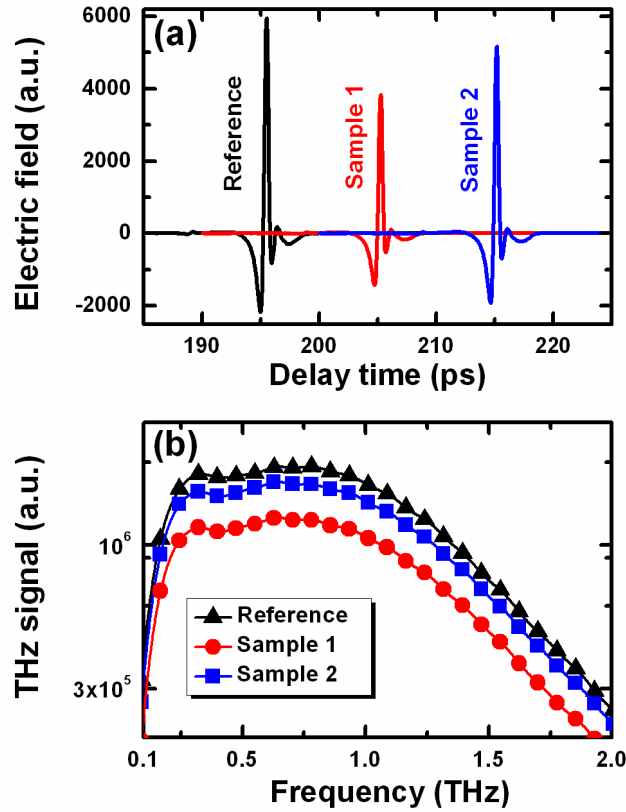


**Figure 3.2** Transmitted THz signals in (a) time domain and (b) frequency domain (0.1-2 THz). The transient pulses in (a) have been shifted horizontally for easy observation.

The analysis of carrier concentration dependent effective mass begins with the numerical computation of the complex refractive index  $n(\omega)$  of n-ZnO films from the transmission coefficient  $t(\omega)$  via the following equation derived earlier in section 3.3 [141]:

$$t(\omega) = \frac{E_{sam}(\omega)}{E_{ref}(\omega)} \cdot \frac{E_{ctrl}^1(\omega)}{E_{ctrl}^2(\omega)} = \frac{2n(n_s + 1) \exp[i\omega(n-1)d/c]}{[(1+n)(n+n_s) + (n-1)(n_s-n) \exp(2i\omega nd/c)] \cdot \exp[i \cdot (n_s - 1) \cdot \Delta d \cdot \omega / c]}, \quad (3.11)$$

where  $E_{sam}(\omega)$  and  $E_{ref}(\omega)$  are the transmitted THz electrical field through the n-ZnO film on sapphire substrate and through the bare sapphire substrate reference, respectively.  $E_{ctrl}^1(\omega)$  and  $E_{ctrl}^2(\omega)$  are the THz electrical field measured respectively for the control sample at the time the reference sample was measured and remeasured at the time when the reference sample deposited with ZnO was measured.  $n_s$  and  $n$  are the refractive indices of sapphire substrate and n-ZnO film respectively,  $d$  is the thickness of the n-ZnO film,  $c$  is the speed of light in vacuum and  $\omega$  is the angular frequency of the THz radiation. The ratio  $E_{ctrl}^1(\omega)/E_{ctrl}^2(\omega)$  provides for the correction factor due to system instability.  $\Delta d$  is introduced in case there is the thickness difference between different spots on the sapphire substrate.  $n_s$  was taken as 3.11 from the analysis of THz transmission through sapphire substrate. With  $n(\omega)$  at hand, the computation of the complex dielectric function  $\varepsilon(\omega)$  and complex conductivity  $\sigma(\omega)$  proceed easily through the well-established relationship:

$$n^2(\omega) = \varepsilon(\omega) = \varepsilon_r(\omega) + i\varepsilon_i(\omega) = \varepsilon_{DC}(\omega) + i\sigma(\omega)/\varepsilon_0\omega, \quad (3.12)$$

where  $\varepsilon_r$  and  $\varepsilon_i$  are real and imaginary parts of the dielectric function respectively,  $\varepsilon_{DC}$  is the static dielectric constant (7.46 for ZnO), and  $\varepsilon_0$  is the free space permittivity [142]. In the THz frequency range, the dielectric response of n-ZnO films is adequately described by Drude model via  $\varepsilon(\omega) = \varepsilon_{DC} - \omega_p^2 / (\omega^2 + i\gamma\omega)$ , where a gas of free electrons of concentration  $N_0$  moves against fixed positive ion cores with the motion being damped by carrier scattering occurring with the

characteristic collision frequency  $\gamma = 1/\tau$ , where  $\tau$  is the free carrier scattering time and  $\omega_p^2 = N_0 e^2 / \epsilon_0 m^*$  is the plasma frequency of n-ZnO film. It is evident that  $\tau$  and  $\omega_p$  are necessary to get  $m^*$ .

Free carrier scattering time  $\tau$  was extracted directly from the complex conductivity  $\sigma(\omega)$ , which was already obtained from equation (3.12) after knowing the value of  $n(\omega)$ . In order to verify the applicability and effectiveness of our proposed method over a wider range, the result on n-ZnO film of thickness 3.73  $\mu\text{m}$  grown by MOCVD with a lower carrier concentration of  $5.87 \times 10^{17} \text{ cm}^{-3}$  and mobility 102.0  $\text{cm}^2/\text{Vs}$  reported by Zhang *et al.* is included in the following analysis (Sample 3) [131]. By substituting the dielectric function  $\epsilon(\omega)$  from Drude model into equation (3.12), the conductivity  $\sigma(\omega)$  can be expressed as

$$\sigma(\omega) = \sigma_0 / (1 - i\omega\tau), \quad (3.13)$$

where  $\sigma_0 = N_0 e^2 \tau / m^*$  is the DC conductivity. Instead of adopting the non-linear multi-variable fitting to get  $\tau$  used previously by other groups [131, 134, 143], we introduce a single-variable linear fitting by taking the ratio of the imaginary part to real part of the conductivity in equation (3.13), resulting in:

$$\frac{\text{Im}(\sigma)}{\text{Re}(\sigma)} = \tau\omega. \quad (3.14)$$

**Figure 3.3** shows the linear relationship of the ratios  $\text{Im}(\sigma) / \text{Re}(\sigma)$  against  $\omega$  for ZnO samples, where the slope is the free carrier scattering time  $\tau$ . For  $\omega > 10^{13} \text{ rad/s}$  ( $\sim 1.6 \text{ THz}$ ), the small discrepancy of samples 2 and 3 from the expected linear behavior indicates that  $\tau$  is slightly dependent on frequency. Free electron scattering time  $\tau$  for samples 1, 2 and 3 was determined to be 8.92 fs, 23.2 fs and 68.0 fs, respectively from linear curve fitting using least squares method

as shown in **Figure 3.3**. It is worthy to note that ZnO sample 1 has the shortest free carrier scattering time, which is attributed to the more frequent scattering resulting from higher carrier concentration, as measured by Hall experiment [144].

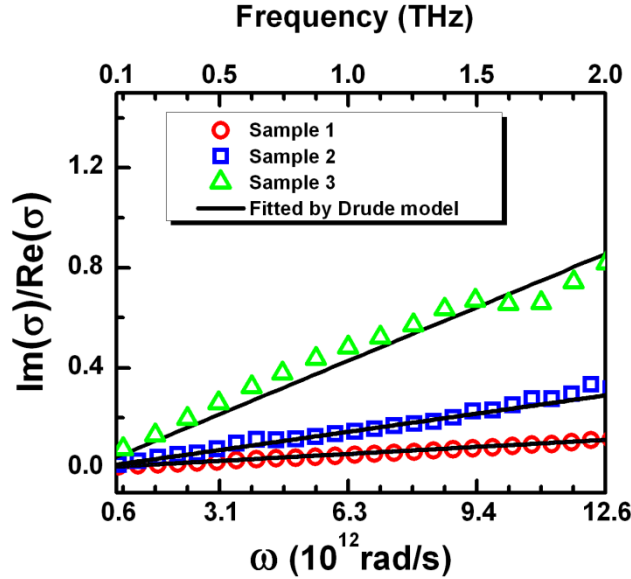


**Figure 3.3** The ratio between imaginary part and real part of conductivity ( $\text{Im}(\sigma)/\text{Re}(\sigma)$ ) as a function of angular frequency  $\omega$  for sample 1 (red circle), sample 2 (blue square) and sample 3 (green triangle). Fitted linear lines whose slopes reveal electron scattering time are also shown.

Finally, the electron effective mass was obtained via the determination of plasma frequency of ZnO film. Since the frequency of THz radiation is 2 orders of magnitude smaller than the electron collision frequency of ZnO samples ( $\omega \ll \gamma$ ), i.e.  $\sim 1$  THz compared to  $\sim 100$  THz, the imaginary part of the dielectric function  $\varepsilon_i$  in Drude model can be simplified as:

$$\varepsilon_i = \frac{\omega_p^2 \gamma}{\omega(\omega^2 + \gamma^2)} \approx \frac{\omega_p^2}{\omega \gamma}, \quad (3.15)$$

By taking the logarithm on both sides of the equation (3.15), it becomes:



$$\log(\varepsilon_i) = -\log(\omega) + \log(\omega_p^2/\gamma) . \quad (3.16)$$

Plotting  $\log(\varepsilon_i)$  against  $\log(\omega)$  as shown in **Figure 3.4**, straight lines with negative unity slope were obtained. Again, a linear-curve fitting technique based on the least squared method was applied. The plasma frequency  $\omega_p$  of ZnO samples 1, 2 and 3 determined from the vertical axis intercept was found to be  $\omega_{p1}=6.96\times 10^{14}$  rad/s,  $\omega_{p2}=2.32\times 10^{14}$  rad/s and  $\omega_{p3}=9.00\times 10^{13}$  rad/s. It can be seen that the plasma frequency of ZnO film, which lies in the infrared range of electromagnetic spectrum, reduce with the decrease of carrier concentration. By substituting the electron concentration  $N_0$  obtained from Hall measurement into the equation  $\omega_p^2 = N_0 e^2 / (m^* \varepsilon_0)$ , the electron effective masses for samples 1, 2 and 3 are calculated to be  $0.26m_0$ ,  $0.25m_0$  and  $0.23m_0$ , respectively.

Values of the dielectric and carrier transport parameters for ZnO samples 1, 2 and 3 are summarized in **Table 3.1**. It reveals that at higher electron concentrations (samples 1 and 2), the effective masses are larger than the prevalently used value  $0.24m_0$  [145]. These larger values obtained are reasonable by taking the heavier polaron into consideration, as the measurement was performed at frequencies below the highest longitudinal optical phonon frequency of ZnO ( $590 \text{ cm}^{-1}$ ) [146].

**Table 3.1** Summary of the transport and dielectric properties of n-ZnO samples obtained from Hall and THz-TDS measurement.

Sample No.	$d$	$N_0$	$\mu$	$\mu$	$\tau$	$\gamma$	$\omega_p$	$m^*/m_0$
	( $\mu\text{m}$ )	( $\text{cm}^{-3}$ )	( $\text{cm}^2/\text{Vs}$ )	( $\text{cm}^2/\text{Vs}$ )	(fs)	( $10^{14}$ rad/s)	( $10^{14}$ rad/s)	
	SEM	Hall	Hall	TDS	TDS	TDS	TDS	TDS
Sample 1 (PLD)	0.49	$4.0 \times 10^{19}$	20.1	59.5	8.92	7.04	6.96	0.26
Sample 2 (PLD)	0.55	$4.3 \times 10^{18}$	22.8	161.7	23.2	2.71	2.32	0.25
Sample 3 (MOCVD) <sup>4</sup>	3.73	$5.9 \times 10^{17}$	102.0	493.0	68.0	0.92	0.90	0.23

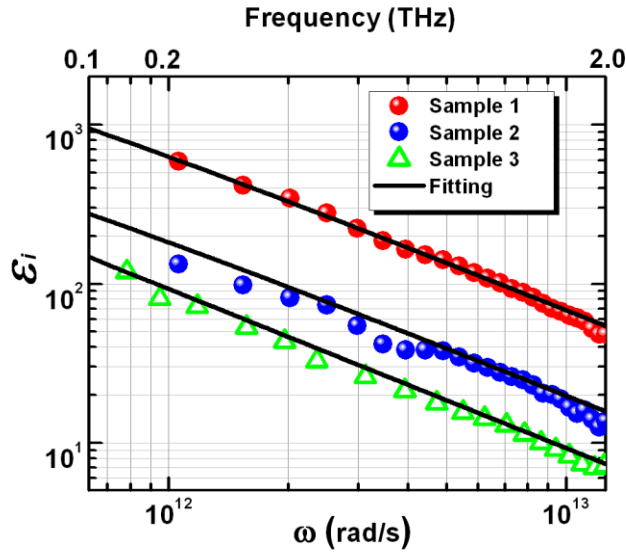


**Figure 3.4** The imaginary part of dielectric function  $\epsilon_i$  as a function of angular frequency  $\omega$  for sample 1(blue), sample 2(red) and sample 3(green) in double log plot. Fitted linear lines by Drude model are also shown.

Moreover, the electron effective masses obtained from three samples show clearly a positive correlation with carrier concentration  $N_0$ , i.e. ZnO sample with higher carrier concentration has a larger electron effective mass. This correlation agrees well with reported experimental results and theoretical calculations [139]. At higher electron concentration, the probability of higher

energy states in the conduction band being occupied by electrons increases. Since the conduction band is non-parabolic and the curvature of the  $E-k$  curve decreases with energy, a higher carrier concentration results in a higher effective mass of the conduction electrons.

In addition, it is well known that the effective mass is related to mobility and carrier scattering time by

$$\mu = e\tau/m^* . \quad (3.17)$$

By substituting the effective mass and free carrier scattering time extracted above into equation (3.17), the mobility of samples 1, 2 and 3 is obtained as 59.5, 161.7 and 493.0  $\text{cm}^2/\text{Vs}$  respectively. It is noticed that the mobility obtained through this approach follows the same trend of the dependence on carrier concentration as Hall measurement, although the agreement in absolute value with that obtained from Hall measurement is poor. This discrepancy in mobilities can be ascribed to free carrier localization. This is the first report to give an insightful study of the difference in carrier transport mechanism between Hall and THz-TDS measurement. In Hall measurement, free electrons move under the driving DC electric field. However, during the long-distance transportation of free electrons, one part of them would be trapped as a result of certain scatterings such as with grain boundaries or defects, resulting in carrier localization [147, 148]. The localized electrons cannot travel over a long distance and do not contribute to Hall mobility. Thus, the mobility measured by Hall Effect showed relatively smaller value than by THz-TDS.

### **3.6 Summary**

In summary, we have demonstrated a new and easily accessible approach to determine carrier effective mass and carrier scattering time due to free carrier and carrier localization mechanisms

by THz-TDS and Hall measurements. It is found the electron effective masses of n-ZnO films varies from  $0.23m_0$  to  $0.26m_0$  as the electron concentration changes from  $5.9 \times 10^{17} \text{ cm}^{-3}$  to  $4.0 \times 10^{19} \text{ cm}^{-3}$ , which show a positive correlation with carrier concentration. The carrier concentration dependent character is attributed to the non-parabolicity of conduction band. Free carrier scattering time measured by THz-TDS decreases with carrier concentration. The mobility obtained from Hall measurement is smaller in value than would otherwise be obtained from free carrier scattering alone due to carrier localization. THz-TDS combined with Hall measurement has been demonstrated as a simple but powerful approach to study carrier transport properties of ZnO film, which is also applicable to other semiconductor materials.

# **Chapter 4 Intrinsic doping of ZnO nanorods grown by solution method**

## **4.1 Introduction**

Synthesis and characterization of intrinsically doped ZnO nanorods are the main focuses of this chapter. The solution growth method - microwave and water bath assisted heating – introduced in Chapter 2 is described in detail here, explaining the mechanism of ultrafast microwave synthesis method with a comparison to the conventional water bath assisted synthesis. The effect of pH in the growth process will also be addressed. A comprehensive and systematic study on the fundamental difference between the water bath and microwave synthesized ZnO nanorods in terms of the intrinsic doping density, and its effect on the lattice structure and optical properties will be presented. The result of post heat treatment is also discussed as it would assist to understand the behavior of intrinsic doping.

## **4.2 Background**

### **4.2.1 Microwave heating and its growth mechanism**

Microwave heating effect was first discovered accidentally by an engineer named Percy LeBaron Spencer in 1945. During his work on microwave for radar application, he noticed that a chocolate in his pocket got melted [149]. Since then microwave has become a powerful, reliable energy source that has been adopted in various applications, such as irradiating coal to remove sulfur and other pollutants, rubber vulcanization, solvent extraction as well as home use. Microwave covers the frequency range from 300MHz to about 300GHz. Within this region, the

electromagnetic energy only affects molecular rotation instead of molecular structures as shown in **Figure 4.1**.

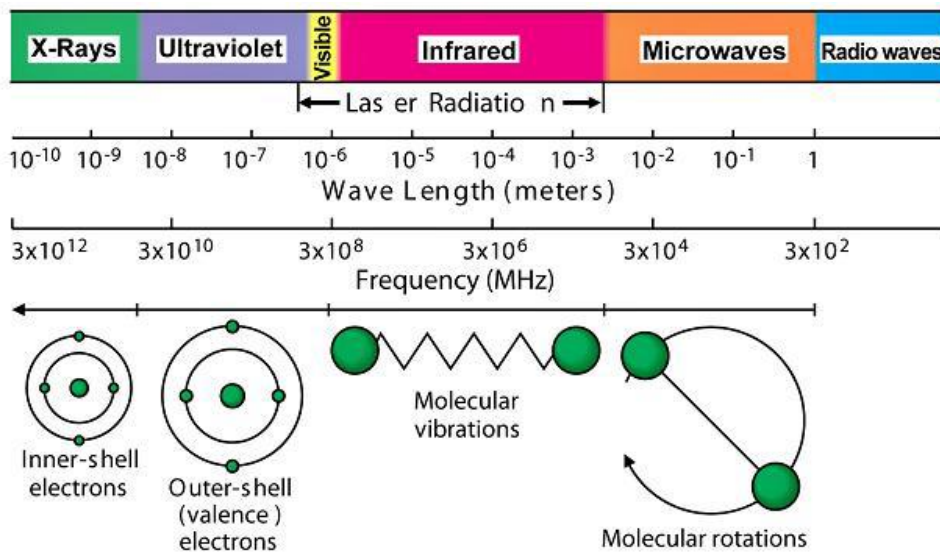


**Figure 4.1** Diagram of the electromagnetic spectrum, showing various properties across the range of frequencies and wavelengths [150].

Among the available frequencies for military, industry, scientific or medical applications, 2.45 GHz is preferred since it has the right penetration depth to interact with laboratory scale samples, and the power sources are available at this frequency to generate microwaves [150]. As the microwave photon energy at 2.45 GHz is 0.978 J/mol and the typical energy to cleave molecular bonds is 334.72 - 502.08 kJ/mol, the energy of microwave is not sufficient to break the molecular bonds. Generally, there are two heat transfer mechanisms for microwave. One is the dipole rotation where polar molecules in the solution or substrates try to align themselves with the rapidly changing electric field of the microwave. The other is the ionic conduction which takes place when free ions or ionic species are present. The electric field of microwave drives ions to move. Due to the alternating nature of the electric field, the ions change direction

periodically. During the motion, collision occurs, resulting in the local temperature heating [150, 151]. In the microwave assisted solution growth, water is one of the most popular solvents to be used. The water molecule is a dipole which responds to the microwave radiation as shown in **Figure 4.2** [149].

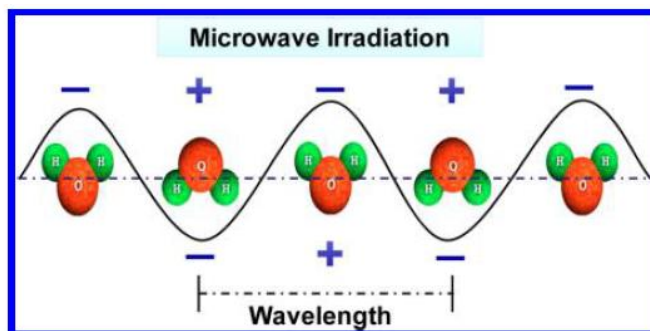


**Figure 4.2** Water molecules experience the changing of electric field under microwave radiation [149].

The ability of a certain material or solvent to convert microwave energy into heat at a specific frequency and temperature is determined by the loss tangent ( $\tan \delta$ ):

$$\tan \delta = \varepsilon'' / \varepsilon', \quad (4.1)$$

where  $\varepsilon''$  is the dielectric loss, which refers to the conversion efficiency of the electromagnetic radiation into heat, and  $\varepsilon'$  is the dielectric constant, representing the polarization of the material in the electric field [152, 153, 154]. A higher  $\tan \delta$  of a reaction medium at a specific microwave frequency means better absorption and higher efficiency in heating, which is the criterion for solvent selection. Water is one of the most commonly used solvents in solution synthesis. The loss tangent of water at 2.45 GHz is 0.123 at room temperature. The optimal frequency for water to absorb microwave energy and convert to thermal energy is at 18 GHz

which is the frequency for satellite communication. The amount of ionic salt added into the water could significantly increase its  $\tan \delta$  [154, 156].

There are several differences between microwave heating and traditional water bath heating. For the traditional water bath synthesis, it requires a heat conductive vessel and heat is introduced into the reactants through heat diffusion, which is a slow process and usually takes a long time. As a result, there is a temperature gradient across the whole system. The whole process is rather slow and inefficient, causing inhomogeneity and poor control of temperature. It is also difficult to be scaled up. On the other hand, microwave couples directly with the molecules in the reaction mixture, which leads to a rapid and homogenous temperature increase. As the process is not dependent on the thermal conductivity of the vessel materials, it allows localized instantaneous heating with better parameter control and energy saving as shown in

**Figure 4.3.**

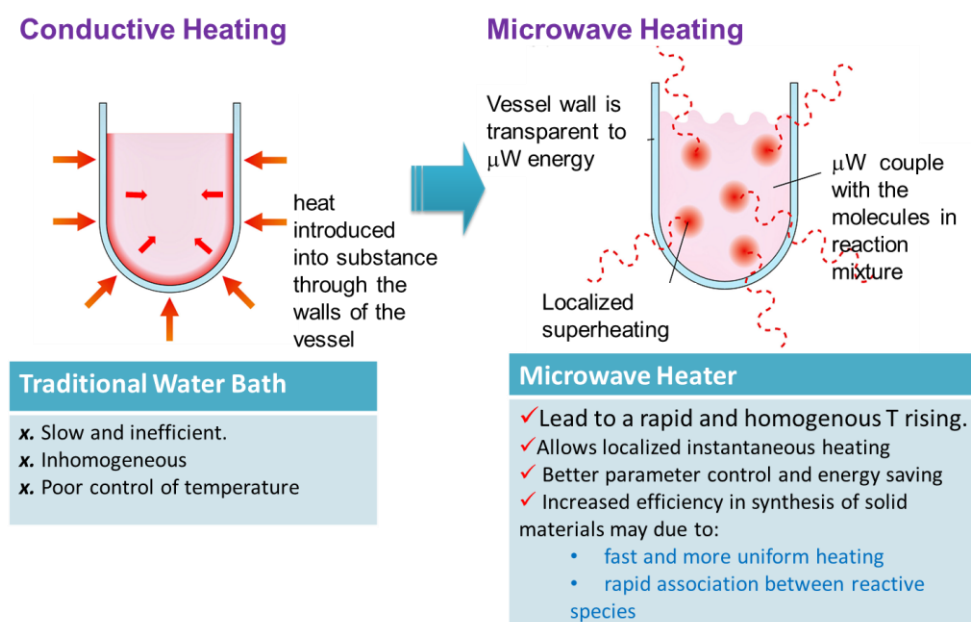


**Figure 4.3** Comparison between conductive heating and microwave heating. The key features of each heating are listed.



During the solution based synthesis, chemical reaction occurs. The energy change of a typical chemical reaction in solution with respect to the reaction time is plotted in **Figure 4.4**. In a typical reaction coordinate, the process starts with reactants A and B. In order to complete the transformation, the system must absorb energy  $E_a$  (activation energy) from the environment, which is supplied by microwave. Once enough energy is absorbed, the reactants quickly react and move to a lower energy state  $E_p$  as a final product. Microwave radiation does not change the  $E_a$ , but provides the momentum to overcome this barrier ( $E_{TS} - E_R = E_a$ ) and complete the reaction much faster with higher throughput compared to conventional heating methods. As the typical microwave energy transfer time ( $10^{-9}$  s) is much shorter than kinetic molecular relaxation time ( $10^{-5}$  s), it leads to non-equilibrium conditions and a high instantaneous temperature to enhance the reaction rate and product yield. However, there is still an intense debate regarding the nature of microwave heating on the reaction rate, whether there are non-thermal microwave effects, such as increase in collision efficiency, rotation or vibration transitions excitement and their effects on activation energy [152, 156].

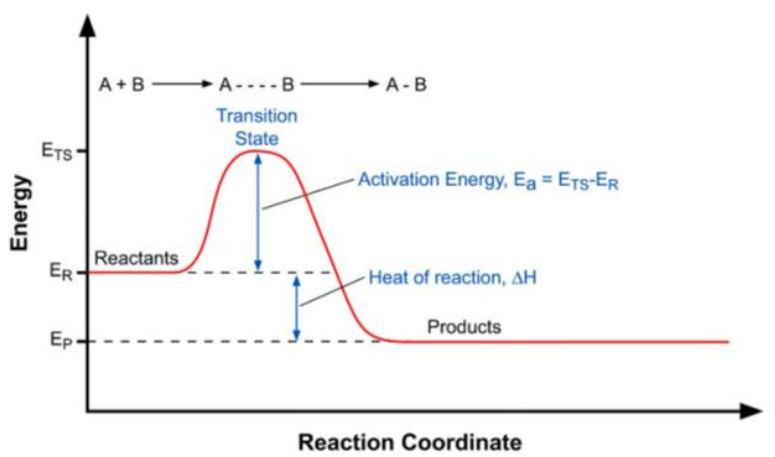


**Figure 4.4** The energy change of a chemical system with respect reaction time [150].

Microwave-assisted synthesis has been recommended as one of the environmentally friendly methods in a review article “viable methodologies for the synthesis of high-quality nanostructure” by Patete [158]. The microwave assisted synthesis has been proved to achieve an order of magnitude enhancement in reaction rate, uniformity, selectivity and energy saving as compared to the water bath synthesis. Katsuki et al. demonstrated that the conventional heating system consumed 6 times more energy than microwave heating system in the synthesis of cubic BaTiO<sub>3</sub> nanoparticles [159]. Idalia et al. explained the reason why microwave irradiation accelerated ZnO nanoparticle formation compared to conventional heating from kinetic and thermodynamic aspects using zinc acetate and benzyl alcohol solution with different temperature (120 to 180°C) and duration (0.5 to 35 minutes). They found that the rate constant of dehydration process is enhanced by 10 times and the rate constant of crystal growth is increased from 3.9 nm<sup>3</sup> /min (conventional heating) to 15.4 nm<sup>3</sup>/minute (microwave heating) [160]. Richardson et al. also investigated that the increase in nucleation and growth rate of the epitaxial ZnO films on spinel is attributed to the high heating rate of microwave assisted growth based on the classical nucleation theory [161].

While, a common concern of microwave synthesis is whether its attractive advantages come with a penalty in crystal quality and defect density of the systemized material. However, an accurate and systematic comparison on the defect and optical quality of ZnO nanostructures synthesized by both methods has yet been reported, which is highly desirable and is therefore the motivation of the work in this chapter.

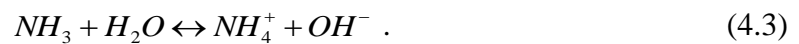
### 4.2.2 Effect of pH in solution growth

In the solution synthesis, pH is an important parameter, which controls the growth habit of ZnO through charges on the surfaces and especially affects the hydrolysis and condensation process of the solution [162]. The pH of a solution is defined as the negative logarithm of the hydrogen ion concentration in the solution:

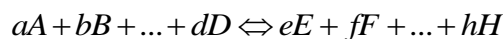
$$pH = -\log[H^+], \quad (4.2)$$

where  $[H^+]$  is the concentration of the hydrogen, the square bracket denotes the concentration which is measured in molar from here onwards. Molar is defined as the number of moles of ions per liter water. At 25°C, the ion product of water is  $[H^+][OH^-]=10^{-14}$  and  $[H^+]$  and  $[OH^-]$  have the same concentration of  $10^{-7}$  M. Thus, the pH of pure water is 7 at this temperature. The pH of a solution can be controlled by the concentration of acids and alkali, which supplies the excess of  $H^+$  or  $OH^-$ .

Ammonia was chosen to control the pH of the solution in this work. The equilibrium of ammonia in water is given by



In a water solution, ammonia dissolves into hydroxide ions, thus an ammonia solution is alkaline. The relationship between ammonia concentration and pH can be obtained from the equilibrium constant, K. In general, K can be calculated from reaction equilibrium:



$$K = \frac{[e]^e [F]^f \dots [H]^h}{[A]^a [B]^b \dots [D]^d}, \quad (4.4)$$

For the case of ammonia dissolution, K at 25°C can be calculated based on equation (4.4):

$$K = \frac{[NH_4^+][OH^-]}{[NH_3]} = 1.76 \times 10^{-5} \quad (\text{at } 25^\circ\text{C}). \quad (4.5)$$

If ammonia concentration is assumed to be 1 M ( $[NH_3]=1$ ),  $[NH_4^+]$  and  $[OH^-]$  have the same concentration of  $4.2 \times 10^{-3}$  M as obtained from equation (4.5). By substituting  $[OH^-]$  into the ion product of water,  $[H^+][OH^-]=10^{-14}$  at 25°C, the concentration of  $[H^+]$  could be found and the pH of the solution is obtained as 11.62 according to equation (4.2) [163]. Thus, with different concentrations of ammonia, the pH of the solution is varied accordingly.

As discussed in Chapter 2 regarding the growth and nucleation of ZnO, the ionization of hydroxyl groups determines the surface charge of ZnO. In the presence of water, the surface groups can be ionized in the following manner:



In solution, the dehydration process of  $Zn^{2+}$  cations is completed via the adsorption of  $H_2O$ . Due to the strong attraction of the electrons in  $H_2O$  by the positively charged  $Zn^{2+}$ , the  $H^+$  ions become loosely bonded in  $H_2O$  and under certain conditions, one  $H^+$  dissociates and an  $OH^-$  is remained on the  $Zn^{2+}$  surface. The remaining  $H^+$  in the  $OH^-$  requires a higher energy to dissociate from the O-H bond, depending highly on the pH of the solution. In an acidic solution with low pH,  $H^+$  in the O-H bond on the surface is more difficult to dissociate into the solution where the concentration of  $H^+$  is high. In contrast, under a higher pH, the concentration of  $H^+$  drops in the

solution and it is much easier for the  $H^+$  to dissociate from the  $OH^-$  into the solution, leaving  $O^{2-}$  alone with  $Zn^{2+}$ . Another  $Zn^{2+}$  from the solution is attached to the remaining  $O^{2-}$  through charge attraction. Then the new round of dehydration process takes place. As a result, a higher pH can promote the growth rate of ZnO with a higher rate of the  $Zn^{2+}$  adsorption and the related  $OH^-$  dissociation [164]. Depending on the pH of solution, the net surface charge of the ZnO can be positive, neutral and negative. The particular pH at which ZnO surface has a net neutral charge is defined as the point of zero charge (PZC) as shown in **Figure 4.5**. The value of PZC has been reported to be in the range of 8.7 - 9.7 [160, 161]. It has been found that as the pH moves far away from PZC, the interface energy  $\gamma$  becomes small, which leads to a minimal  $\Delta G_{crit}$  for nucleation of ZnO to take place according to equation (2.2) [160, 161].

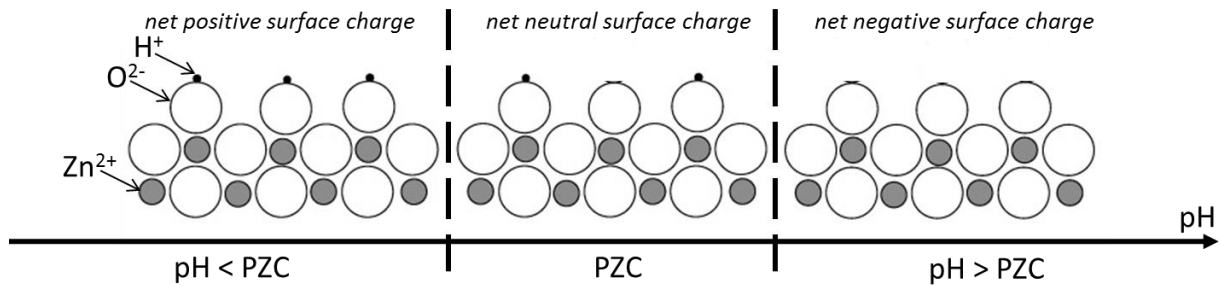


**Figure 4.5** pH determines the surface charge of ZnO, adopted from reference [168].

### (a) pH and defects

Akhavan et al. has studied the effect of pH in the range of 7.5 to 11.44 using zinc nitrate and NaOH as precursors. They found that the ZnO nanorod diameter increased with pH but a blue shift of the bandgap emission was observed as the pH increased due to the higher defects density through fast growth rate [162]. Tay C.B et al. studied the correlation between pH, growth rate

and defects of ZnO nanorods grown by the aqueous solution method with the same precursors zinc acetate and ammonia as we used here [169]. With a higher ammonia concentration, the higher pH leads to a higher concentration of  $\text{OH}^-$  and more negatively charged growth units in the solution. A much stronger attraction between  $\text{H}^+$  ions and the solution pulls  $\text{H}^+$  ions away from the ZnO surface, which results in fewer  $\text{H}^+$  defects and higher growth rate since more free sites are available for zinc cations. In addition, the higher growth rate cannot provide sufficient time for dehydration of excess hydroxyl groups. As a result, excess oxygen from the hydroxyl groups contributes to the oxygen interstitials and zinc vacancies [170]. A verification of such defect creation hypothesis will be discussed in the following sections of this chapter and extended to the microwave assisted synthesis.

### **4.3 Sample preparation and experimental procedure**

The ZnO nanorods were grown on Si (100) substrates using two different aqueous solution routes: microwave synthesis and heated water bath. Due to the large lattice mismatch between ZnO and Si, the seed layer is needed to promote the secondary nucleation to take place. Thus, all the four steps of the growth procedure (a)-(d) listed below, which were introduced in Chapter 2, are compulsory here. Since this is a comparison experiment, the details of the experiment control and the specific parameters of growth, such as ammonia concentration, are emphasized below.

- a) Bare Si (100) substrates were cleaned with acetone, IPA and deionized (DI) water, followed by spin-coating of a ZnO seed layer and rapid thermal annealing for 20 minutes in air at 350 °C.
- b) The substrates were submerged facing downwards into 20 ml of stock aqueous synthesis solution, which consist of 0.02 M ZnAc<sub>2</sub> with varying concentrations of ammonia ([NH<sub>3</sub>]).
- c) The different [NH<sub>3</sub>] used were 0.255, 0.503, 0.748, 0.988 and 1.222 M. A stock solution was prepared for each [NH<sub>3</sub>] to ensure that the chemical composition of the growth solutions for microwave and heated water bath are the same.
- d) In microwave and heated water bath setups, growth temperature and duration were kept constant at 90°C and 20 min. After the growth, the samples were cooled down to room temperature naturally, rinsed thoroughly in DI water and blown dry with nitrogen gas.

The morphology of samples was characterized by field emission scanning electron microscopy. XPS measurements were also performed on the as-grown and post-growth annealed samples. The as-grown samples were annealed in-situ under the high vacuum conditions ( $<1 \times 10^{-8}$  Torr) in the XPS chamber at 500°C for 10mins. Low temperature photoluminescence measurements (LTPL) were performed at 20 K using the micro-PL system.

## 4.4 Results and discussion

### 4.4.1 Comparison of microwave and waterbath growth

Early studies show that the solubility of Zn in aqueous solution is strongly pH dependent and influences the growth rate, morphology and type of native defects in the ZnO nanorods [167]. Good coverage of ZnO nanorods on a variety of substrates has been routinely obtained in the pH range of 10.07 to 10.9, where the pH is larger than the known PZC of ZnO. In this growth regime, surface adsorbed H<sub>2</sub>O molecules readily hydrolyzes to release H<sup>+</sup> into OH<sup>-</sup> rich environment, allowing the negatively charged major growth units Zn(OH)<sub>4</sub><sup>2-</sup> to be adsorbed onto

the positively charged polar Zn face, leading to a fast anisotropic growth rate along the c-axis of ZnO. With higher  $[\text{NH}_3]$ , the higher pH leads to an increased solubility of Zn ( $C_{\text{Zn}}^*$ ) according to the ionic equilibrium [164, 167], which results in two effects. The first effect is the lowering of the supersaturation degree of ZnO ( $S$ , where  $S = \frac{C}{C^*}$ ), leading to a lower initial nucleation rate as discussed in section 2.2.1.1, which is typically visualized as a lower areal density of nanorods on the substrate. The second effect is the availability of a larger reservoir of soluble Zn growing on fewer nucleation sites, which leads to longer nanorods with larger diameters [171]. **Figure 4.6** (a) to (e) show the top views of the nanorods from samples M1 to M5 which were obtained using a microwave synthesizer with the microwave power of 100W while **Figure 4.6** (f) to (j) show samples W1 to W5 which were obtained using a heated water bath under  $[\text{NH}_3]$  of 0.255 M, 0.503 M, 0.748 M, 0.988 M and 1.222 M. It is observed that both heated water bath and microwave synthesized samples show a similar trend of decreasing areal density of nanorods, increasing diameter and lengths with the increase of  $[\text{NH}_3]$  from 0.255 to 1.222 M. This suggests the underlying chemistry and interface properties remains intact as expected.

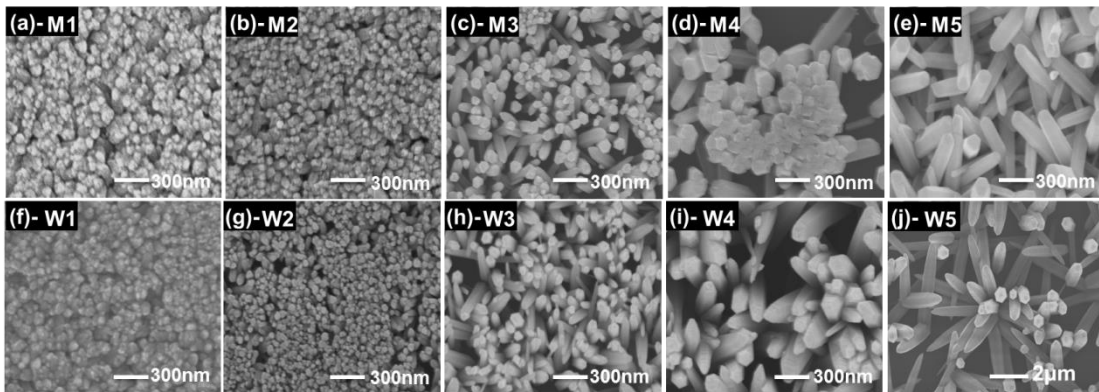


**Figure 4.6** Top-view SEM images of the as-grown ZnO nanorods samples by microwave synthesizer (first row samples: M1 to M5) and heated water bath (second row samples: W1 to W5) respectively at 90°C for 20 minutes with different  $[\text{NH}_3]$  (0.255 M, 0.503 M, 0.748 M, 0.988 M and 1.222 M) and 0.02 M  $\text{ZnAc}_2$ .



Close comparison of the SEM images of M1-M5 against W1-W5 respectively shows that microwave synthesized samples M1-M5 have a slightly higher density and smaller diameter than heated water bath samples W1-W5. **Figure 4.7** statistically compares the average diameter of the nanorods as a function of  $[\text{NH}_3]$ . Particularly, the diameters of samples M4 and M5 from microwave synthesizer are much smaller than the corresponding samples W4 and W5 grown in heated water bath at a high ammonia concentration.

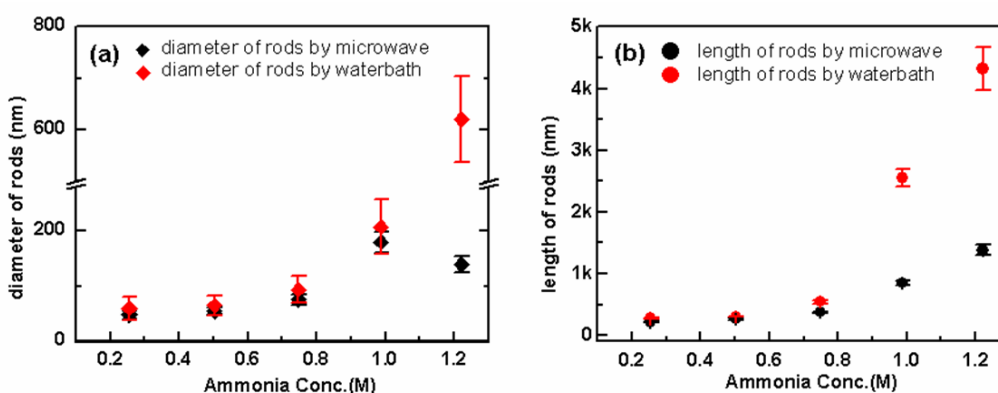


**Figure 4.7** The summary of statistical analysis of ZnO nanorods diameter and length grown by microwave synthesis and heated water bath (samples M1 to M5 and W1 to W5).

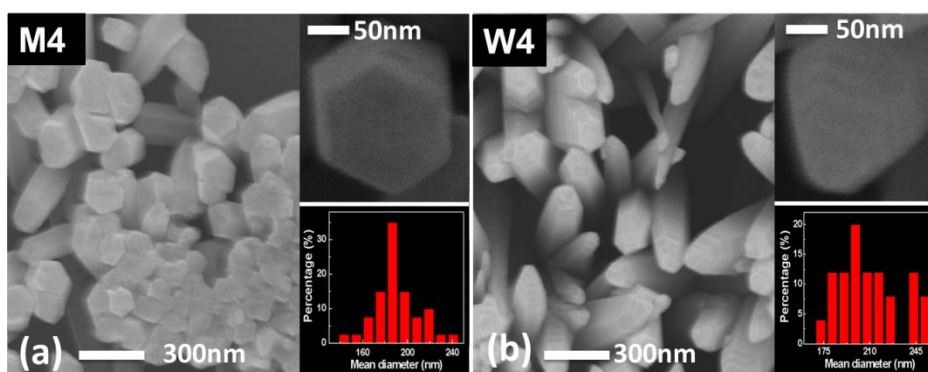
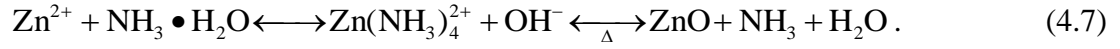


**Figure 4.8** The top view of the ZnO nanorods grown with (a) microwave synthesis (M4) and (b) heated water bath (W4). The inset is the high magnification of the tip of the nanorods (top right) and the statistics of the nanorods diameter for sample M4 and W4 (bottom right) respectively.

Furthermore, as shown in Figure 4.6 and **Figure 4.8**, the tips of the M4 - M5 nanorods were flat in comparison to the tapered ends of W4-W5. The tapering of the top of the ZnO nanorods grown from solution is attributed to the faster growth rate along the [0001] direction than those along other directions. One possible explanation is that growth proceeded at a much faster rate in microwave synthesis than heated water bath, leading samples M4-M5 to undergo dissolution in the presence of high concentrations of OH<sup>-</sup>. The following chemical reactions could take place in the solution, which leads to a simultaneous deposition and dissolution of ZnO,



In this reaction, the Zn(NH<sub>3</sub>)<sub>4</sub><sup>2+</sup> ions react with OH<sup>-</sup> to form ZnO, pushing the equilibrium in the above equation (4.7) to the right hand side at a higher temperature above 75°C. At the end-of-growth, the concentration of Zn(NH<sub>3</sub>)<sub>4</sub><sup>2+</sup> is reduced, pulling the above equilibrium (4.7) back towards the left and resulting in the dissolution of ZnO, thus the ends of the microwave synthesized nanorods becoming flat [172]. The result reveals that the microwave heating is able to achieve end-of-growth condition faster than that with conventional heated water bath method due to the fast growth rate.

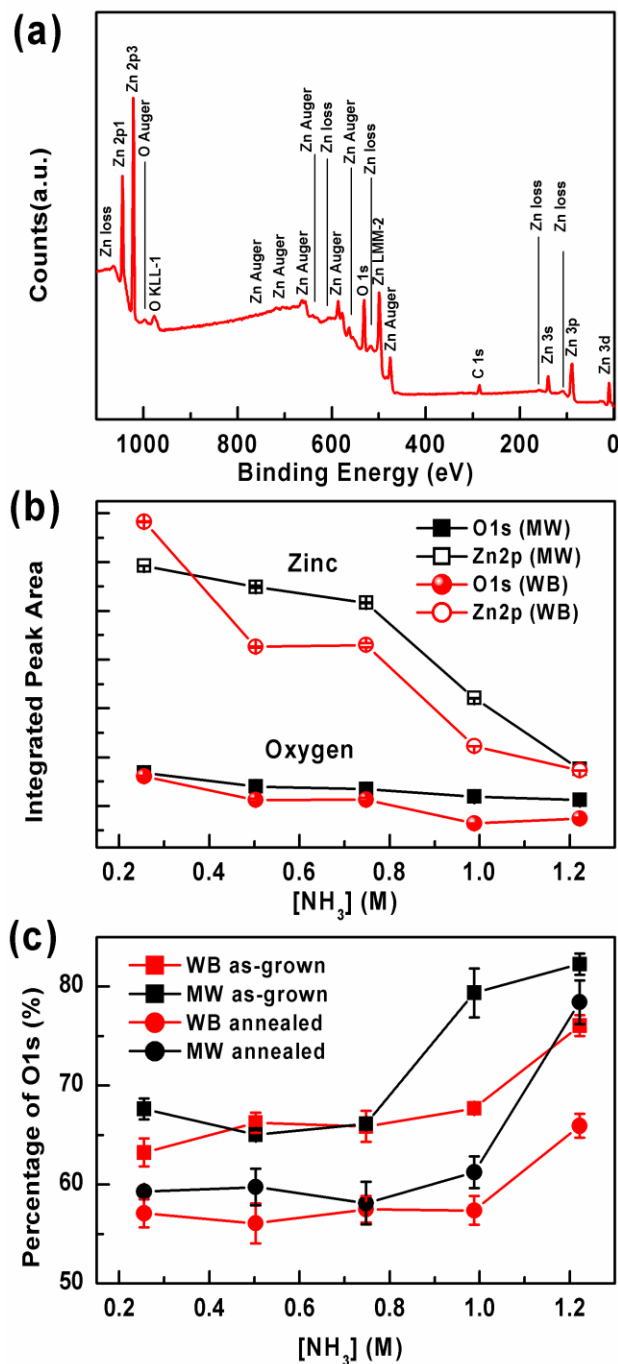


**Figure 4.9** (a) XPS survey spectrum of ZnO nanorods. (b) The integrated peak area of O 1s and Zn 2p for as-grown samples under different ammonia concentration. (c) The quantified percentage of O 1s in ZnO of as-grown and annealed samples grown by microwave synthesis and heated water bath.

The XPS spectra of samples M1-M5 and W1-W5 show the high purity of the grown ZnO nanorods, with the presence of carbon impurity only shown in **Figure 4.9(a)**. In Figure 4.9(c), for the as-grown samples the percentage of oxygen in ZnO rises from 60-70% to 80% as the  $[\text{NH}_3]$  increases from 0.255 to 1.222 M for as-grown samples. The trend of increasing O ratio relative to Zn with respect to the  $[\text{NH}_3]$  can be attributed to the increased concentration of oxygen interstitials ( $\text{O}_i$ ) or zinc vacancies ( $\text{V}_{\text{Zn}}$ ). As mentioned in section 4.2.2, with a higher  $[\text{NH}_3]$ , the higher pH leads to a higher concentration of  $\text{OH}^-$  and more negatively charged growth units in the solution. A much stronger attraction between  $\text{H}^+$  ions and the solution pulls  $\text{H}^+$  ions away from the ZnO surface, which provides more available sites for  $\text{Zn}^{2+}$  cations due to fast dissociation of  $\text{H}^+$  ions. In addition, the higher growth rate cannot provide sufficient time for  $\text{Zn}^{2+}$  to occupy every available site or dehydration of excess hydroxyl groups. As a result, the lack of zinc in the lattice formation and excess oxygen from the hydroxyl groups contribute to  $\text{O}_i$  and  $\text{V}_{\text{Zn}}$ . Regarding the annealed samples, the O ratio is much lower compared to that of the as-grown samples and tends towards the stoichiometric 50%. Since the reported migration barriers of  $\text{V}_{\text{Zn}}$  and  $\text{O}_i$  are 1.4 eV, and 0.23-1.98 eV respectively, depending on the migration paths and defect charge states [170, 171], the presence of low migration paths with low migration barrier energies for both  $\text{V}_{\text{Zn}}$  and  $\text{O}_i$  intrinsic defects leads to the out-diffusion of  $\text{O}_i$  and  $\text{V}_{\text{Zn}}$  after a thermal anneal at 500°C and thus the observed improvement in stoichiometric ratio.

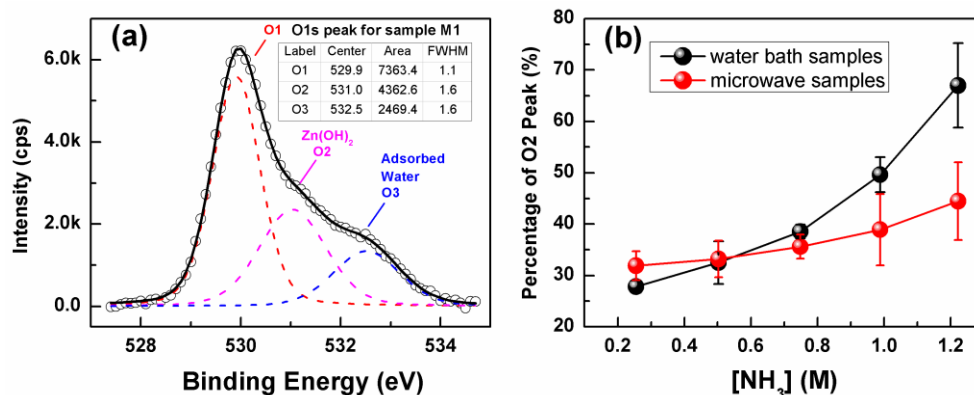


**Figure 4.10** (a) O 1s peak from XPS deconvoluted into three Gaussian-Lorentz peaks (O1, O2 and O3 assigned in the plot) for sample M1. (b) Percentage of O2 in the total O 1s peak for as-grown microwave and water bath assisted heating samples.

A closer examination of the asymmetric O 1s peak shows three Gaussian components as shown in **Figure 4.10(a)** for sample M1. The lowest binding energy component O1 at 530 eV is related to the O<sup>2-</sup> ions in the ZnO lattice. The second component O2 at 531 eV is assigned to O-related defects such as O<sub>i</sub>. Finally, the third component O3 at 532.3 eV is usually attributed to adsorbed water [172, 173, 174]. The ratio of the second component O2 to the entire O 1s peak is plotted in **Figure 4.10(b)**. It is shown that both microwave and water bath grown samples have an increasing ratio of O2 peak with a higher [NH<sub>3</sub>], which means more O<sub>i</sub> defects at a higher pH. This is in agreement with results presented in **Figure 4.9** and also reported results by others [167], which explained the role of higher pH in accelerating the growth rate, leading to higher incorporation of O-defects in an O<sup>-</sup>-rich environment as we discussed in section 4.2.2. Interestingly, **Figure 4.10(b)** also suggests that the use of microwave results in a lower concentration of O-related defects, possibly due to the higher rotational kinetic energy leading to reorientation of Zn(OH)<sub>4</sub><sup>2-</sup> growth units.

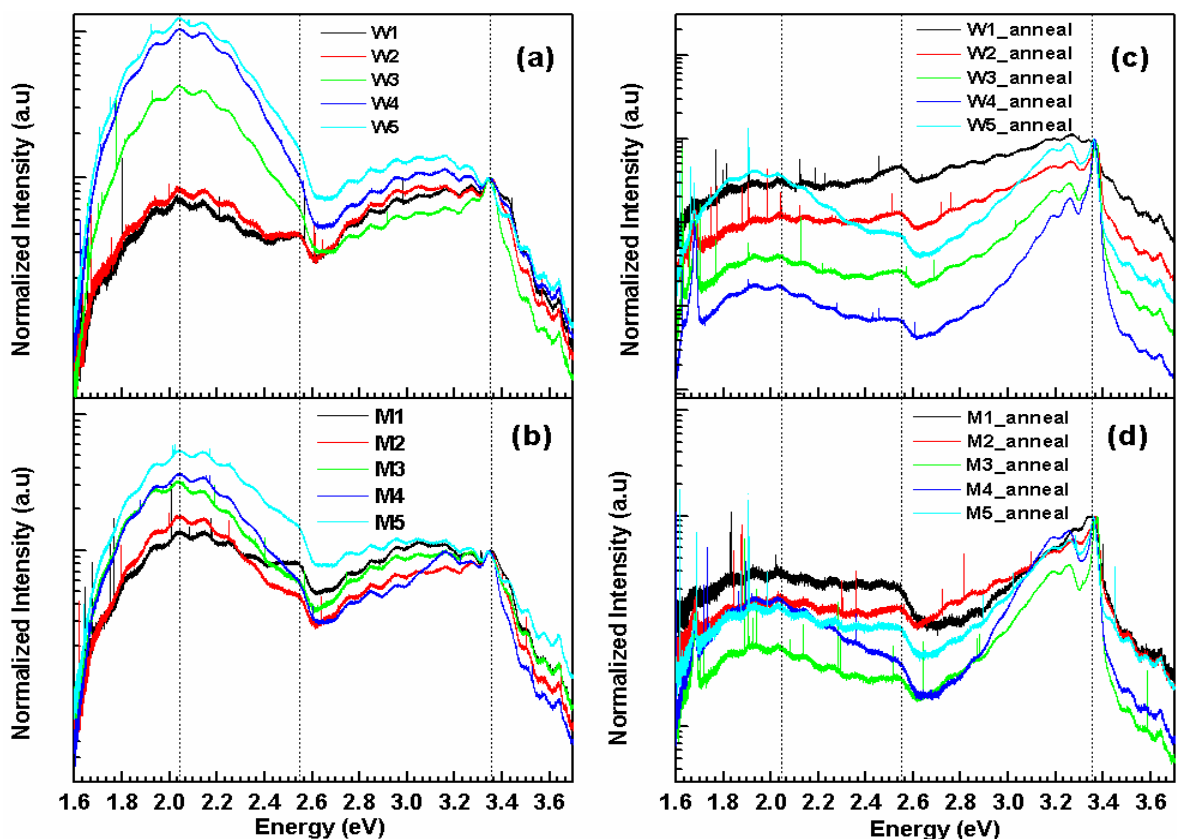


**Figure 4.11** Low temperature photoluminescence spectra of ZnO nanorods normalized to band edge peak at 3.37 eV at 20 K for (a) as-grown heated water bath samples (b) as-grown microwave synthesis samples (c) annealed heated water bath samples and (d) annealed microwave synthesis samples as a function of  $[\text{NH}_3]$ .

When optical measurement conditions are kept as constants, the ratio of visible to UV PL emission is a useful gauge to compare defect concentrations between different growth conditions. **Figure 4.11(a-b)** show the LTPL spectra of as-grown water bath and microwave samples respectively, while **Figure 4.11(c-d)** present the corresponding annealed samples. There are three peaks of interest: the UV band edge at 3.37 eV (368 nm), the green emission at 2.55 eV (486 nm) due to  $V_{\text{Zn}}$  [178] and the orange emission at 2.04 eV (608 nm) due to  $O_i$  [179]. The dependence of the orange and green emission ratio is plotted in **Figure 4.12 (a)** and **(b)** respectively.

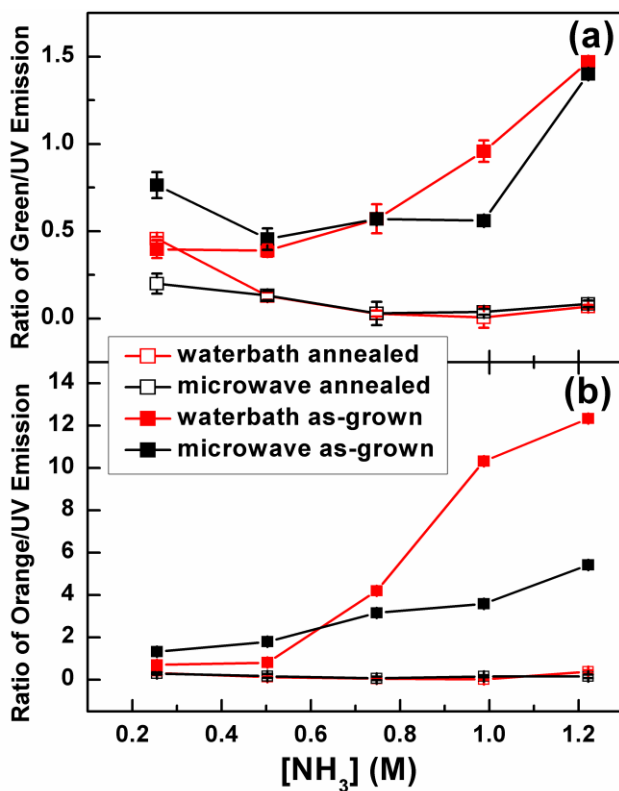


**Figure 4.12** The ratio of (a) orange and (b) green emission to the band-edge emission for as-grown and annealed samples by both microwave and water bath assisted heating.

The ratio of orange emission to that of the band edge emission for both microwave and water bath increases with pH. In addition, the microwave synthesized ZnO has a weaker orange emission (lower density of  $O_i$ ) compared to the heated water bath which is in good agreement with the XPS data, reinforcing the conclusions from the component fitting of O 1s peak in Figure 4.10 (b). It is important to note that the green emission also increases with pH, thus suggesting that  $V_{Zn}$  is the cause of the high O to Zn ratio, consistent with the XPS data shown in Figure 4.9(b) displaying the integrated peak area of O and Zn for as-grown samples under different  $[NH_3]$ . After annealing, the ratios of orange and green PL emission are reduced significantly with respect to the as-grown samples, suggesting out-diffusion of  $O_i$  and  $V_{Zn}$  and thus leading to a

more stoichiometric ratio of Zn to O as seen earlier in Figure 4.9(c). The above two findings agree with the trend of XPS O2 peak with  $[\text{NH}_3]$  shown in Figure 4.10(b).

The samples were further studied by ultraviolet Raman scattering. The result was shown in **Figure 4.13(a)** and the Lorentzian peak fitting was employed to extract  $A_1(\text{LO})$  phonon, which records the vibration of atomic displacements of Zn-O bond along the c-axis [179]. The peak at the lower frequency is recognized as surface optical phonon mode which is due to the columnar nature of the film [180]. As the absorption of 325 nm laser in ZnO is strong, the effect of the surface layer (a few mono-layers) on Raman scattering is enhanced due to the Frohlich interaction.

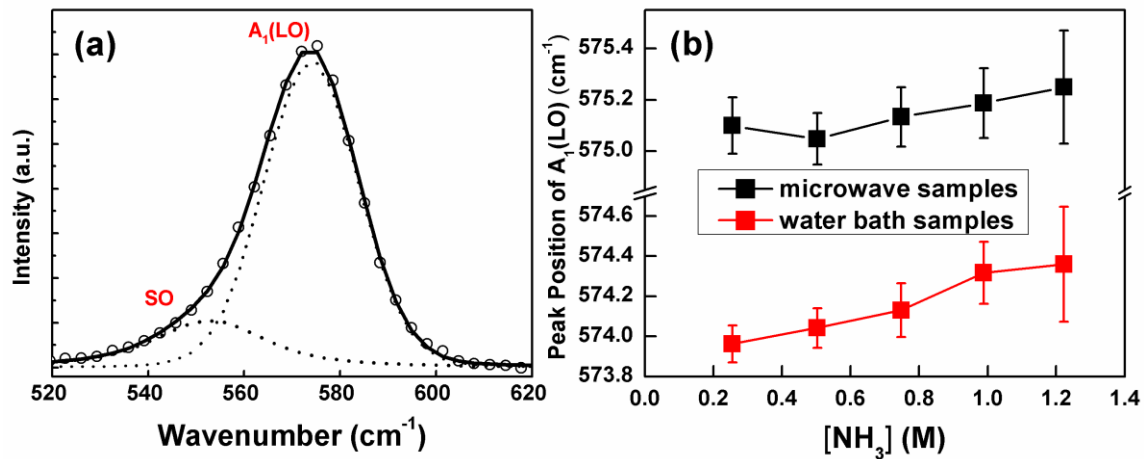


**Figure 4.13** (a) The  $A_1(\text{LO})$  and SO peak of Raman scattering for as-grown W1 measured at room temperature. (b) The actual measured (scattered) and fitted (line)  $A_1(\text{LO})$  peak position for both microwave synthesized and heated water bath samples in different  $[\text{NH}_3]$ .

It is noticed that the peak shift of Raman  $A_1(\text{LO})$  against the  $[\text{NH}_3]$  is plotted in **Figure 4.13(b)**. The  $A_1(\text{LO})$  frequency increases (blue shift) with the  $[\text{NH}_3]$  for both microwave synthesized and heated water bath samples, which is most possibly ascribed to the phonon localization by defects or impurities. Correlating with the oxygen and zinc defects analysis of the XPS O 1s and Zn 2p3



spectra as well as the LTPL orange and blue emission peaks, it is apparent that the dominant mechanism for the shift in  $A_1(\text{LO})$  peak is because of the presence of  $O_i$  and  $V_{\text{Zn}}$ . As  $O_i$  and  $V_{\text{Zn}}$  both lead to a shorter Zn-O bond length, it results in a larger compressive strain, and thus a blue shift of  $A_1(\text{LO})$  peak frequency as  $[\text{NH}_3]$  increases [180]. This applies to both microwave and water bath grown ZnO samples. However, there is a difference about  $0.9\text{cm}^{-1}$  between microwave and waterbath sample, which may be due to the faster growth rate with microwave synthesisor resulting in a higher compressive strain compared to those grown by the water bath. Further investigation is needed to confirm the results.

In order to make an in-depth comparison of the defects and crystal quality between microwave and water bath samples from Raman, the FWHM of the  $A_1(\text{LO})$  peak of ZnO samples were examined, since the FWHM of the  $A_1(\text{LO})$  peak is a good indicator of the crystal quality of the material. The broader  $A_1(\text{LO})$  linewidth implies poorer the crystal quality which was attributed to more intrinsic defects incorporated into the lattice [181]. As shown in **Figure 4.14**, the FWHM of the  $A_1(\text{LO})$  phonon for microwave synthesized samples are smaller than those of the heated water bath samples using the same  $[\text{NH}_3]$ , which indicated that the microwave synthesized samples have fewer defects and better crystal quality as compared to the heated water bath samples grown using the same precursors.

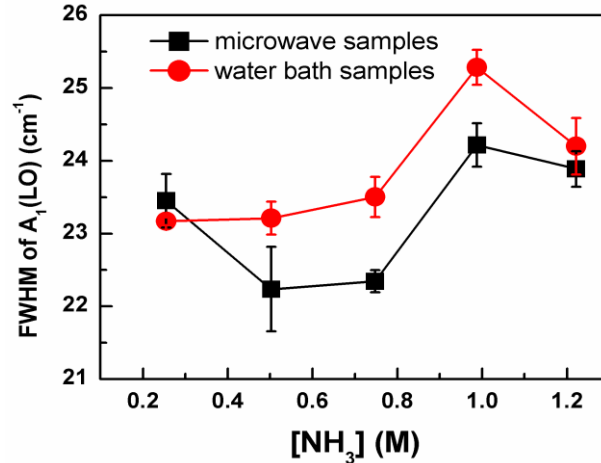


**Figure 4.14** The FWHM of the A<sub>1</sub>(LO) peak from Raman scattering measurement for the as-grown ZnO samples by microwave synthesis and heated water bath with different [NH<sub>3</sub>].

## 4.5 Summary

A detailed comparative study between the microwave synthesis and heated water bath for the growth of ZnO nanorods has been carried out. Compared to the heated water bath, the microwave synthesis produces a faster growth with more uniform size distribution of nanorods due to the unique ability of simultaneously heating the entire volume of solution. Due to the fast growth rate, the dissolution of the nanorods also occurs earlier (within 20 minutes). The rotational energy delivered by the 2.45 GHz microwaves allows the growth units to orientate themselves on the surface, leading to lower intrinsic doping such as O<sub>i</sub> and V<sub>Zn</sub>, which can be easily removed by a post-growth thermal anneal at 500°C in vacuum. Microwave synthesis presents a promising new approach to grow ZnO with low defects level at a low temperature. It is attractive to the applications where low-cost polymer substrates are favorable as they cannot withstand high temperature process. It also leads to new growth strategies for controlling the functionalities and morphologies of a wide range of metal oxide nanostructures.

## **Chapter 5 Optimized route towards stable p-type potassium doped ZnO by low temperature solution growth method**

### **5.1 Introduction**

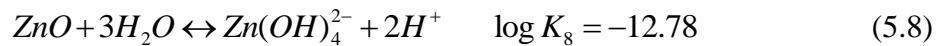
This chapter starts with the calculation of the ionic equilibrium concentration of the dominant ionic species present in the  $\text{ZnAc}_2$  and  $\text{KAc}$  system. Five ZnO samples with different potassium doping concentrations were fabricated, followed by the study of the structural, optical, and electrical characteristics of the ZnO films to demonstrate the influence of the chemistry of the growth environment on the type and nature of the incorporated K defects. Finally, the effect of thermal annealing from  $200^\circ\text{C}$  to  $700^\circ\text{C}$  on the optical and electrical properties of the film is investigated and the doping mechanism is elucidated.

### **5.2 Ionic equilibrium model of $\text{KAc-ZnAc}_2$**

As discussed in detail in section 2.2.1.3 on the growth procedure for ZnO films, the ZnO films fabricated in this work were grown in two phases. The first growth phase produced a thin layer of nanorods on the substrate, typically with lengths of about 400 to 500 nm and diameters of about 80 to 150 nm. This thin layer of nanorods formed an important template that allowed the secondary growth to continue and eventually coalesced into a film, typically 1 - 2  $\mu\text{m}$  thick, in the second growth phase. The precursor solution used in the second growth phase consisted of only  $\text{ZnAc}_2$  and  $\text{KAc}$ , resulting in a typical pH of less than 7, depending on the relative amounts of  $\text{ZnAc}_2$  and  $\text{KAc}$  that were added. The choice of a relatively low pH compared to the “standard” growth pH of 10 - 11 was deliberate [182], as it has been proved that this range of pH

produces a slow growth rate of ZnO that results in a lower concentration of native defects and better optical properties [183].

In order to determine the types of majority species in the growth solution, the ionic equilibrium of the ZnAc<sub>2</sub>-KAc solution was computed for a range of KAc concentrations using temperature dependent equilibrium rate constants K<sub>1</sub>-K<sub>9</sub> shown in the following reaction equations (5.1) to (5.9) [184].



In addition, the total amount of acetate added into the solution is equal to the amount of acetate in the solution for mass balance:

$$C_{Ac} = [Ac^-] + [Zn(Ac)^+] + 2[Zn(Ac)_2] + [K(Ac)]. \quad (5.10)$$

In the solution, the charge should also be balanced or neutral which means that the total number of positive charges should be equal to the total number of negative charges:

$$\begin{aligned} & 2[Zn^{2+}] + [Zn(OH)^+] + [Zn(Ac)^+] + [K^+] + [H^+] \\ & = [Zn(OH)_3^-] + 2[Zn(OH)_4^{2-}] + [(Ac)^-] + [(OH)^-]. \end{aligned} \quad (5.11)$$

The ionic equilibrium for the solution can be obtained by solving simultaneously the reaction equations (5.1) to (5.9), the mass and charge balance equations (5.10) to (5.11). There are in total eleven unknowns ( $K^+$ ,  $Zn^{2+}$ ,  $Ac^-$ ,  $Zn(Ac)^+$ ,  $ZnO$ ,  $Zn(OH)_2$ ,  $Zn(OH)_3^-$ ,  $Zn(OH)^+$ ,  $Zn(OH)_4^{2-}$ ,  $H^+$ ,  $OH^-$ ) which can be solved by the eleven equations. The known quantities are  $KAc$  and  $ZnAc_2$  in molar concentration.

Using the model described above, the ionic equilibrium of the  $ZnAc_2$ - $KAc$  in solution can be calculated for various  $KAc$  precursor concentrations and temperatures by keeping the  $ZnAc_2$  concentration at 0.03M.

An important process parameter in solution growth is the solubility of zinc, denoted as  $C_{Zn}^*$ , which is defined as the total amount of zinc ions in the precursor solution and can be easily obtained by the sum of all the zinc species in the solution:

$$C_{Zn}^* = [Zn^{2+}] + \sum_1^4 [Zn(OH)_m^{(2-m)+}] + \sum_1^2 [Zn(Ac)_p^{(2-p)+}]. \quad (5.12)$$

**Figure 5.1(a)** shows the  $C_{Zn}^*$  and the pH ( $[H^+]$ ) as a function of the concentration of  $KAc$ .  $C_{Zn}^*$  decreases with  $KAc$ . For a low value of  $C_{Zn}^*$ , the growth does not take place on the pre-coated substrate, but precipitates in the solution make it cloudy. This is explained in section 2.2.1.1. Thus, the  $KAc$  concentration must not be too high and in the experiment  $KAc$  was chosen to be less than 0.24M.

As discussed in section 4.2.2, the charge on the oxide surface in solution depends on the pH. **Figure 5.1(a)** shows that the pH increases towards the PZC at a pH of 8.7 - 9.7 with  $KAc$

concentration. At the same time, as seen in Figure 5.1(b), with the increase of concentration of KAc, there is a rapid increase in the ratio of  $K^+/Zn^{2+}$ . This corresponds to a change from a H-rich growth environment to K-rich growth environment. For the case of the low concentration ratios of  $K^+/Zn^{2+}$  where the pH is less than 6, which is far from the PZC, the hydrated ZnO surface has a positive net charge and a highly saturated surface concentration of hydrogen. This case of low pH represents a growth environment that is H-rich and K-poor, which theoretically favors the formation of neutral  $K_{Zn}-H_i$  complexes. On the other hand, at a high concentration ratio of  $K^+/Zn^{2+}$  that is about 2 orders of magnitude larger than the first case, the pH is closer to the PZC, leading to a less positive net surface charge and a lower surface concentration of hydrogen on ZnO surface. This case of high pH represents an H-poor and K-rich environment, which theoretically favors the formation of neutral  $K_{Zn}-K_i$  complexes. With the objective of demonstrating the critical influence of  $K^+/Zn^{2+}$  concentration ratio and the growth pH, five different concentrations of KAc (0, 0.03, 0.05, 0.08, 0.13, and 0.18 M) were chosen and the samples were labeled A-E, respectively.

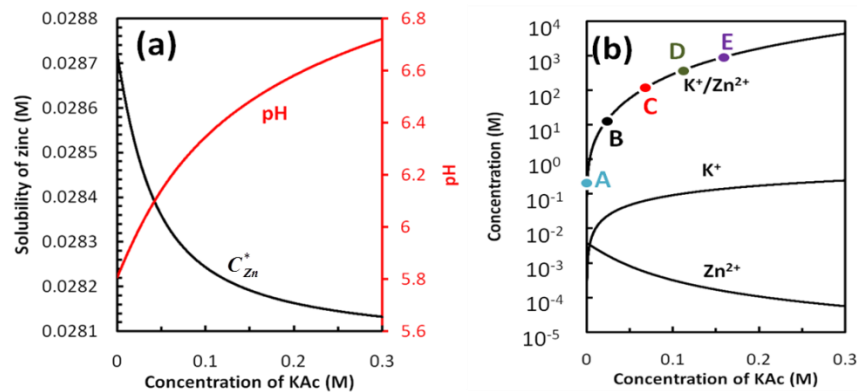


**Figure 5.1** (a) Plot of growth solution pH and  $C_{Zn}^*$  against the concentration of KAc. (b) Plot of concentration of  $K^+$ ,  $Zn^{2+}$  and the ratio of  $K^+/Zn^{2+}$  against the concentration of KAc. The concentration ratios of  $K^+/Zn^{2+}$  for samples A, B, C, D, and E, which correspond to 0, 0.03, 0.05, 0.13, and 0.18 M KAc, are marked accordingly in the plot.

### 5.3 Experimental procedure

The growth was conducted using single-side polished c-plane sapphire substrates and the growth procedure listed below follows the one discussed in section 2.2.1.3.

- i. Sapphire substrates were ultrasonically-cleaned sequentially in acetone, methanol, and deionized water.
- ii. The clean substrates were spin coated three times with a thin layer of ZnO nanoparticles at 3000 rpm for 30 s.
- iii. To improve film adhesion and promote formation of ZnO, the substrates were subjected to a thermal annealing in air at temperatures 350°C for 20 minutes.
- iv. Densely-packed short nanorods of lengths less than 1 $\mu$ m, were grown in the solution consisting of 0.03 M ZnAc<sub>2</sub>, 0.4 M NH<sub>4</sub>OH, and a certain amount of KAc for 30 minutes at 90°C in water bath.
- v. Coalesced flat-topped nanorods were grown in the solution consisting of 0.03 M ZnAc<sub>2</sub> and a specified amount of KAc.
- vi. The film step was repeated three times to allow the rods to coalesce and form a continuous film. Between each step, the substrate was rinsed thoroughly with deionized water.

In the steps (v) and (vi) of the procedure listed above for preparing ZnO films, five different concentrations of KAc (0, 0.03, 0.08, 0.13 and 0.18 M) were used. They spanned across these two extreme cases, with the growth environment transitioning from a lower K<sup>+</sup>/Zn<sup>2+</sup> with a high hydrogen concentration attached to ZnO surface to a higher K<sup>+</sup>/Zn<sup>2+</sup> ratio with a lower hydrogen concentration attached to ZnO surface. The five samples are labeled as A, B, C, D and E for KAc concentrations of 0, 0.03, 0.08, 0.13 and 0.18 M, respectively.

In order to study the dependence of the post-growth thermal treatment on the doping concentration, annealing was carried out in an ULVAC RTA system. The annealing chamber was pumped down to a vacuum pressure of less than  $5 \times 10^{-5}$  mTorr before a steady flow of nitrogen at 20 sccm was flowed into the chamber. The samples were annealed at temperatures of 200, 300 and 700°C for a duration of 10 minutes and 700°C for 30 minutes. The rate of

temperature rise and fall were kept constants at 100°C/minute. The flow of nitrogen was maintained until the samples are cooled down completely to room temperature.

Hall measurements were carried out using a 4 inch electromagnet from Newport Instruments. The magnetic field was measured by a calibrated magnetic sensor attached to an Empire Scientific Corp Gaussmeter model 904. Current injection and voltage measurement were carried out using Keithley Model 6430 sub-femtoamp sourcemeter and HP 34401A digital multimeter. The transient waveform of the Hall voltage for highly resistive samples was monitored to ensure that steady state conditions have been reached before readings were taken. In/Zn dots were used to make ohmic contacts at the corners of the samples, typically 1 cm by 1 cm, to form Van der Pauw configurations.

Resonance Raman scattering measurements were recorded in a backscattering configuration using a Renishaw Ramascope 2000 with a He-Cd laser as excitation source. A SIMS depth profile was obtained using TOF-SIMS IV, with a high current Ga ion beam for surface sputtering, and a low current Ar ion beam for surface analysis. The film morphology was observed using a JOEL 6700 FE-SEM as described in Chapter 2. Crystal structures were examined by the XRD technique using Bruker D8 Discover (CuK $\alpha$  = 1.54060 Å) system.

In-situ XPS measurements and thermal annealing under UHV were performed in XPS analysis chamber as described in the Chapter 2. All XPS spectra were obtained in a constant pass energy mode where only electrons of a given energy can pass through the electric field of the hemispherical analyzer and reach the detector slits with high sensitivity survey scans (pass energy of 150 eV) and high resolution narrow scans (pass energy of 10 eV), respectively.



## 5.4 Results and discussion

The ZnO films, grown on sapphire, were formed upon the coalescence of nanorods as shown in **Figure 5.2**. A maximum thickness of 2.8  $\mu\text{m}$  was obtained for 0.03 M KAc. The solutions from which samples A, B and C are grown decrease in solubility. With reduction in solubility, the driving force for nucleation is larger, thus resulting in a faster growth rate. Since the samples were grown for the same duration, thickness decreases from samples A to C. However, as mentioned earlier, when the solubility drops too much, homogeneous nucleation takes place, leading to the precipitation of ZnO powders in the solution. Thus, the film thickness began to decrease from samples D to E.

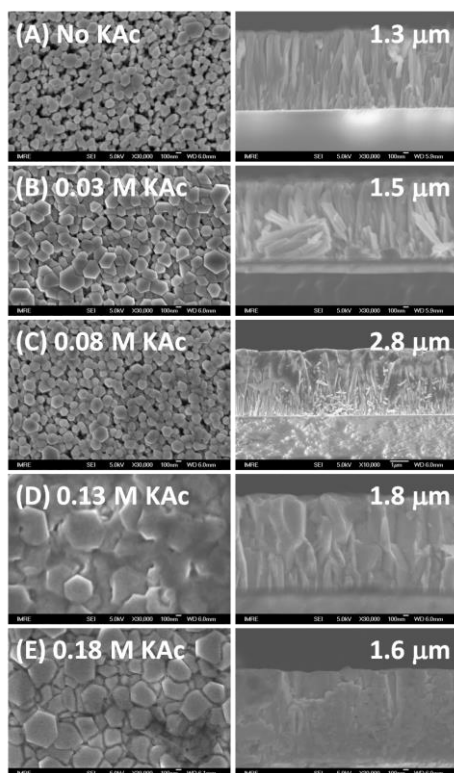


**Figure 5.2** SEM images showing the top and cross-sectional views of samples A, B, C, D and E which were grown in 0, 0.03, 0.08, 0.13 and 0.18 M KAc respectively. The thickness of each ZnO film is shown on the upper right corner of the cross-sectional image.

**Figure 5.3** shows the XRD  $2\theta$  scan of the films. The dominant peaks belonged to ZnO (002) and (004) at  $34.32^\circ$  and  $72.59^\circ$  respectively (JCPDS Card No 36-1451). Observation of (00 $l$ ) peaks indicated that the film has a c-axis orientation. The (002) peak was the strongest at 0.13 M KAc probably due to the best coalescence of columns as seen in the SEM cross-section in Figure 5.2.

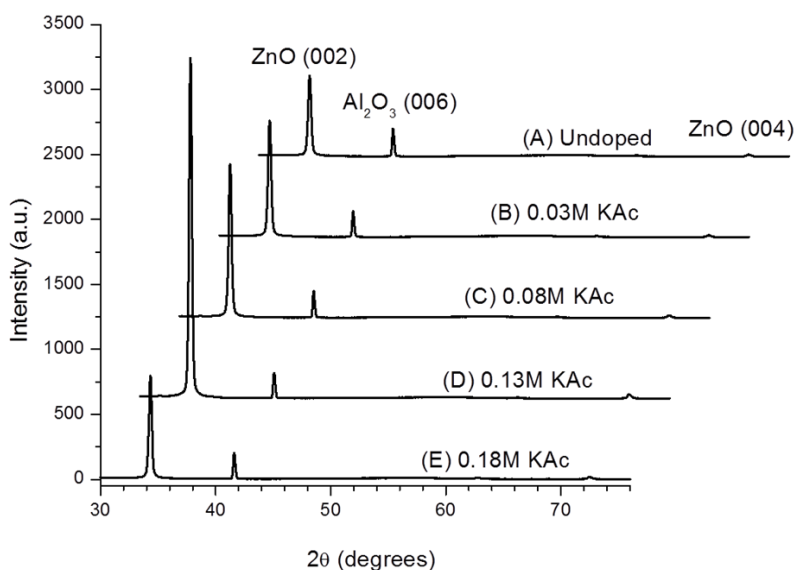


**Figure 5.3** XRD spectra of as-grown samples A, B, C, D and E which were grown in 0, 0.03, 0.08, 0.13 and 0.18 M KAc respectively.

A comparison of the K concentrations in the as-grown samples A, B, C, D and E is shown from the SIMS depth profile of **Figure 5.4**. The increase of K in ZnO films for samples A to C corresponds to the increase in  $K^+$  ion concentration from 0 to 0.08 M KAc in the precursor growth solution. Above 0.08 M KAc, the concentration of K in the film was saturated. This suggests an upper limit to the amount of K that can be incorporated into the film using aqueous solution method. Due to the fact that K is highly soluble in the aqueous solution, this limit is likely to be related to the maximum surface concentration of K that can be adsorbed onto the oxide surface during the growth.

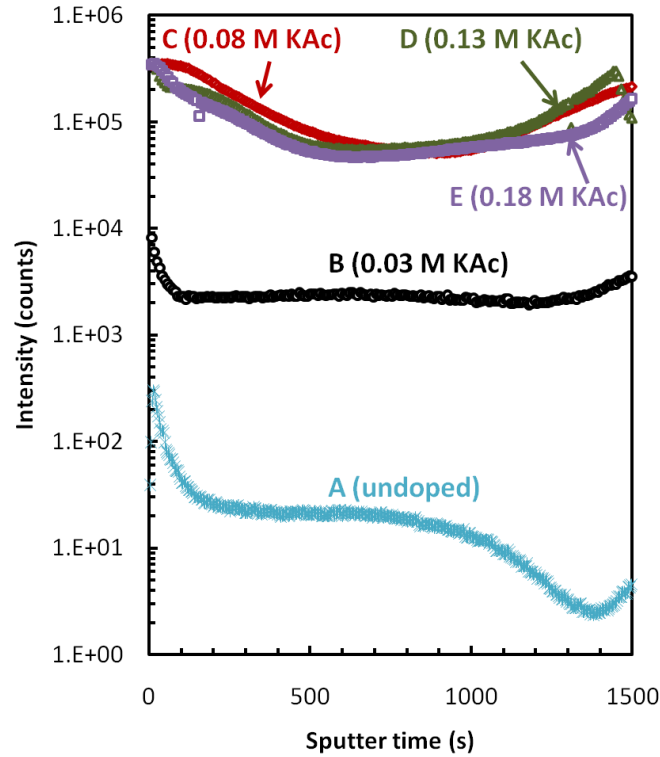


**Figure 5.4** SIMS depth profile of potassium concentrations in the as-grown samples A, B, C, D and E which are grown in 0, 0.03, 0.08, 0.13 and 0.18 M KAc respectively. Although the concentration ratio of  $K^+/Zn^{2+}$  increases from C to E, the amount of K incorporated in the ZnO lattice is relatively unchanged.

The carrier concentrations of the as-grown A to E films obtained from Hall measurements are shown in **Figure 5.5**. An optimum hole concentration of  $4 \times 10^{16} \text{ cm}^{-3}$  is obtained for sample B (0.03 M KAc) with a lower concentration of K in the lattice as shown by SIMS compared to that of samples C, D and E. Although the SIMS depth profile shows that films grown in 0.08, 0.13 and 0.18 M KAc have roughly the same concentration of K incorporated in the ZnO film, their effective hole concentrations measured by Hall decreased with the KAc concentration in the solution.

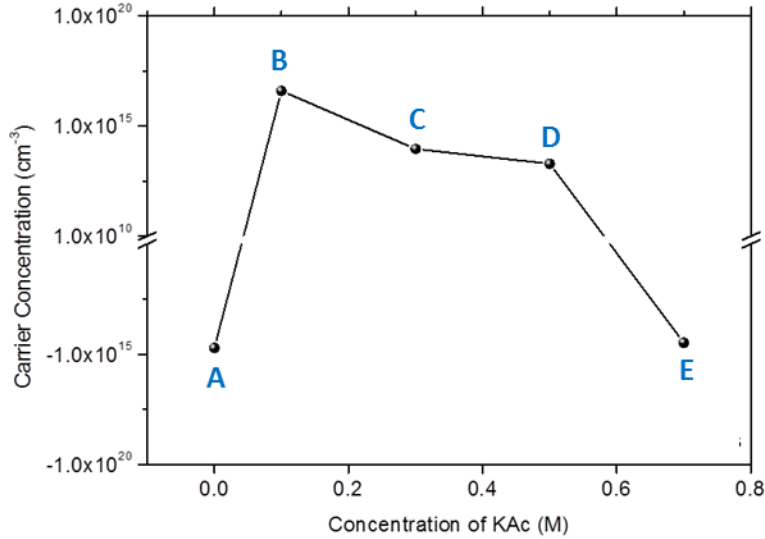


**Figure 5.5** Hall effect carrier concentrations for as-grown samples A, B, C, D and E which were grown in 0, 0.03, 0.08, 0.13 and 0.18 M KAc respectively. A break at  $10^{10} \text{ cm}^{-3}$  is inserted along the vertical axis in order to improve clarity of the plot at higher carrier concentrations.

It is known that K can be incorporated as an acceptor, donor or as an electrically neutral complex in the form the substitutional, interstitial site or stable complex such as  $\text{K}_{\text{Zn}}\text{-K}_i$  and  $\text{K}_{\text{Zn}}\text{-H}_i$  respectively [183, 185, 186], depending on the growth environment. The schematic diagrams of  $\text{K}_{\text{Zn}}\text{-K}_i$  and  $\text{K}_{\text{Zn}}\text{-H}_i$  complexes are shown in **Figure 5.6**. For Sample B with a lower concentration of K in the film, a majority of K was incorporated as  $\text{K}_{\text{Zn}}$ , leading to net p-type conductivity. From samples B to E, with the increase of KAc concentration, the growth environment changed from H-rich/K-poor to H-poor/K-rich. Although the concentration of K in the film increased from B to C and saturated for D and E as seen in Figure 5.4, an increasing proportion of it was incorporated as  $\text{K}_i$ , instead of  $\text{K}_{\text{Zn}}$ . This caused the transition from p-type in B to a highly compensated films in C and D, and finally an n-type film in E. Similar trends can be observed from direct Hall effect measurements of 1 - 5% sputtered Li-doped [187] and 0 - 30% sol-gel deposited Na-doped ZnO films [188].

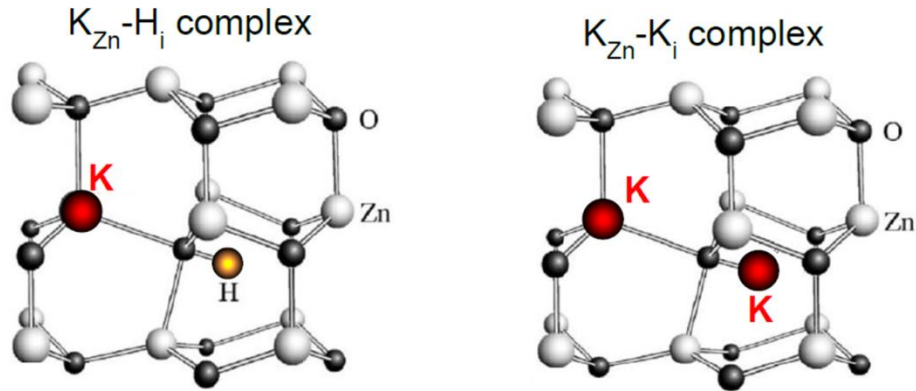


**Figure 5.6** Schematic diagram of  $K_{Zn}$ - $H_i$  complex and  $K_{Zn}$ - $K_i$  complex in ZnO.

Further evidence for the K transition from  $K_{Zn}$  to  $K_i$  sites was provided by resonance Raman Scattering data of the as-grown samples as shown in **Figure 5.7(a)**. The inset of Figure 5.7(b) shows the  $A_1(LO)$  peak which is typically asymmetrical and consists of two components: the main  $A_1(LO)$  component and a lower frequency surface mode component which has been attributed to the columnar nature of the film [189]. After subtracting a linear background and fitting the lower frequency shoulder as a surface mode component, the peak positions of the  $A_1(LO)$  against the concentrations of K are plotted in Figure 5.7(b). Since the  $A_1(LO)$  reflects the vibration of the Zn-O bond along the c-axis [190], a lower wavenumber indicates a longer bond length, i.e. an expansion along the c-axis. The undoped ZnO film had its  $A_1(LO)$  peak centered at  $574\text{ cm}^{-1}$  while the K-doped films had their  $A_1(LO)$  peaks in the range of  $562\text{-}565\text{ cm}^{-1}$ . The significant decrease in frequency implies an expansion of the lattice to accommodate the larger K atoms which are incorporated in the film (bond length is  $0.242\text{ nm}$  for K-O compared to  $0.193\text{ nm}$  for Zn-O [191]).

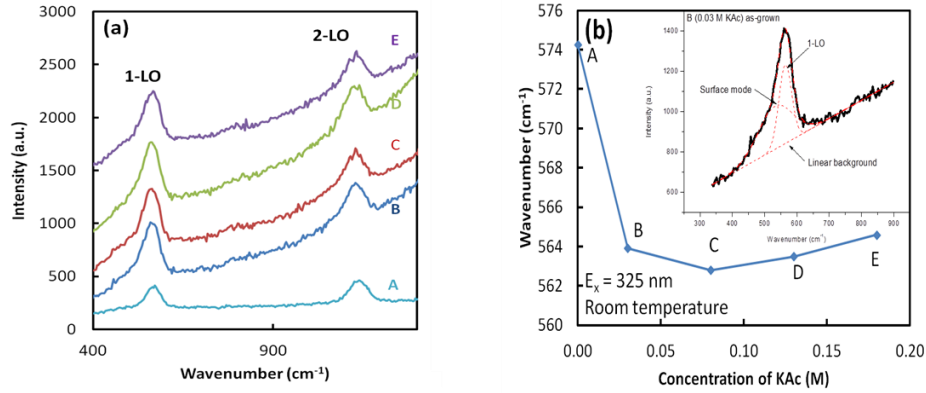


**Figure 5.7** (a) Room temperature resonance Raman scattering spectra and (b) plot of peak positions of  $A_1(\text{LO})$  against the concentration of KAc for as-grown samples A, B, C, D and E which are grown in 0, 0.03, 0.08, 0.13 and 0.18 M KAc respectively. The inset of (b) shows the fitted components consisting of the  $A_1(\text{LO})$  peak and its surface mode for sample C.

Examination of the  $A_1(\text{LO})$  peak positions from B, C, D to E showed a trend with a minimum point at C (0.08 M KAc) where maximum lattice strain occurred. The likely scenario involves the increased incorporation of  $K_{\text{Zn}}$  from B to C, leading to the increased strain and reduced  $A_1(\text{LO})$  peak frequency. Thereafter, the proportion of  $K_i$  relative to  $K_{\text{Zn}}$  increased although the concentration of incorporated K remains as constant. Since the ZnO lattice is relatively open, the strain due to  $K_i$  is less than that of  $K_{\text{Zn}}$ , and thus slightly relieves the strain and leads to increase in  $A_1(\text{LO})$  peak frequency from samples C, D to E. This scenario agrees with both the growth environment as well as the measured carrier concentrations from Hall and SIMS. From samples B to E, the grown environment transits from being K-poor/H-rich to K-rich/H-poor, with the former favoring the formation of  $K_{\text{Zn}}$  and  $H_i$  and the latter  $K_{\text{Zn}}$  and  $K_i$ . This explains why, although sample C had a higher concentration of K than sample B, it did not lead to a higher hole concentration. Similarly, from samples C to E, with the same concentration of K in their lattices,

the conductivity became less p-type in D and eventually n-type in E. These results underline the critical role of the growth environment toward realizing the p-type conductivity.

## 5.5 Effect of thermal annealing

In order to understand the effect of thermal annealing on the evolution of K atoms in the ZnO film, sample C was placed in an annealing chamber where its XPS spectra were measured in-situ. The typical XPS spectra of the ZnO film grown on GaN substrate in 0.08 M KAc is shown in **Figure 5.8(a)**. The annealing temperature was varied from room temperature to 600°C. **Figure 5.8(b)** shows the detailed XPS scan of the K 2p peak for 300°C and 600°C. From the narrow scan of the K 2p peak, the atomic percentage of K was quantified for various annealing temperatures and plotted in **Figure 5.8(c)**. At low temperatures up to 200°C, a slight dip in the K atomic percentage from 0.5 to 0.3% was detected, suggesting depletion by out-diffusion of K atoms from the surface of the film. At 300°C, a sharp increase in the atomic percentage of K from 0.3% to 1.0% was attributed to the thermal dissociation of  $K_{Zn}-K_i$  complex in the bulk of the film followed by thermal diffusion of free  $K_i$  to the surface, where its accumulation showed up as a sharp increase in atomic percentage. Extrapolating from Wardle's estimation of dissociation temperatures of Li and Na complexes at 450°C and 119°C respectively [186], the dissociation temperature of K-based complexes ( $K_{Zn}-K_i$  and  $K_{Zn}-H_i$ ) was expected to be well below 120°C. The migration barrier of  $K_i$  along the c-axis was estimated to be about 1.49 eV [192] and appeared to be the limiting factor that prevents the removal of  $K_i$  at temperatures below 300°C.

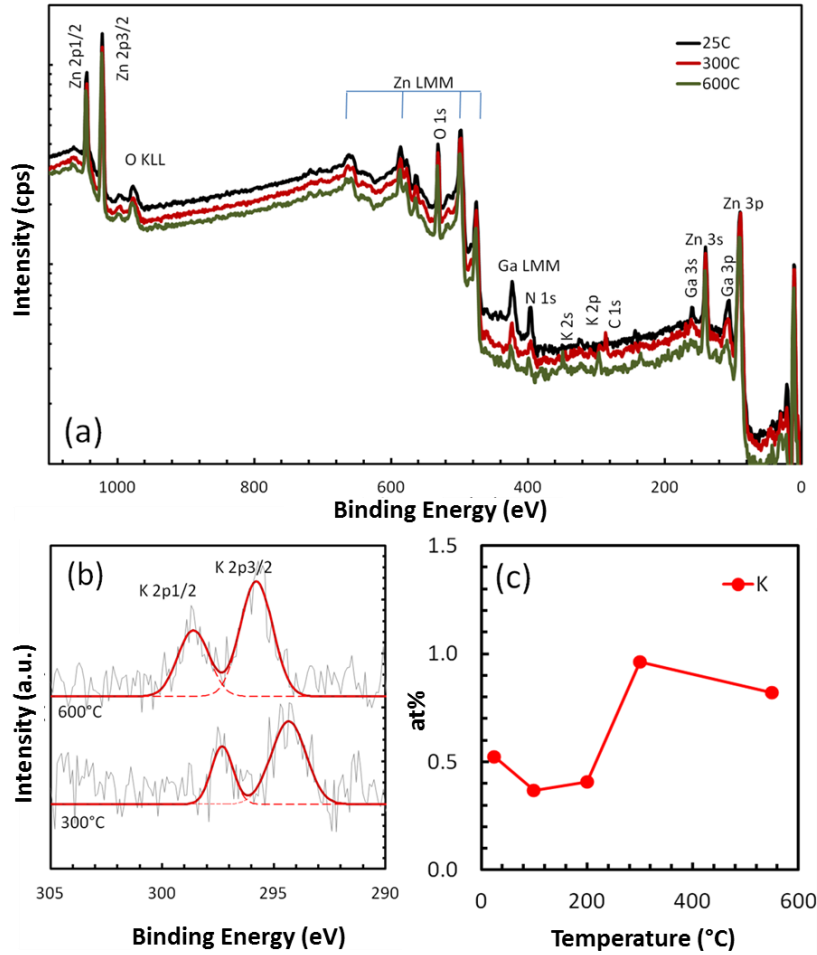


**Figure 5.8** (a) XPS survey scan spectra of as-grown sample C (0.08 M KAc) at 25, 300 and 600°C. (b) The narrow scan of K 2p peaks at 300 and 600°C. (c) The plot of quantified atomic percentage of K from the narrow scan XPS spectra against the annealing temperature.

The reduction in lattice strain arising from the out-diffusion of K at 300°C was observed in the shifts in the  $A_1(\text{LO})$  peak positions after the thermal annealing as shown in **Figure 5.9**. A clear blue shift of the  $A_1(\text{LO})$  peak positions from 562 - 565  $\text{cm}^{-1}$  to 568 - 572  $\text{cm}^{-1}$  in all K-doped samples (B, C, D and E) towards that of the undoped film (A) highlighted in red was observed upon heat treatment at 300°C. After extended heat treatment at 700°C for 30 min, the  $A_1(\text{LO})$



peak position of the K-doped ZnO film remained lower in value than that of the undoped film, indicating that the residual lattice strain arising from  $K_{Zn}$  and  $K_i$  are still remained in the lattice.

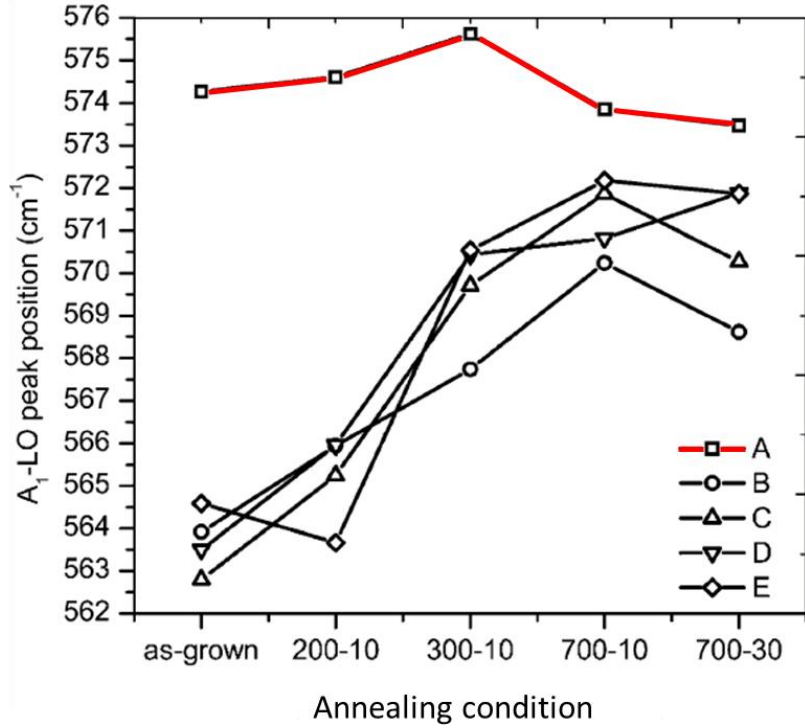


**Figure 5.9** Plot of peak positions of  $A_1(LO)$  against various annealing temperatures for samples A, B, C, D and E. The samples were subjected to annealing temperatures of 100, 200, 300 and 700°C for 10 minutes, and a final 700°C for 30 minutes, indicated at 700-30 in the plot. The sample plotted in red was without K-doped sample.

The measured Hall carrier concentrations with respect to annealing temperature, shown in **Figure 5.10**, provided information on the electrically-active K dopants in the film. The corresponding values of carrier concentration and mobility are summarized in **Table 5.1**. The as-grown K-doped films (B, C, D and E) are highly intrinsic in the range of  $10^{14} - 10^{16} \text{ cm}^{-3}$ , reflecting the high degree of compensation resulting from the presence of both acceptors ( $K_{Zn}$ ) and donors ( $H_i$  or  $K_i$ ). It is only after the heat treatment at 300°C that the dissociated  $K_i$  are

driven out of the film and a clear p-type conductivity is established in samples B and C with hole concentrations of  $1.03 \times 10^{16}$  and  $1.98 \times 10^{15} \text{ cm}^{-3}$ , and hole mobilities of  $56$  and  $44 \text{ cm}^2\text{V}^{-1}\text{s}^{-1}$  respectively. Samples D and E remain as n-type possibly due to a higher concentration of  $\text{K}_i$  which could not be fully diffused out of the film after 10 minutes of annealing.

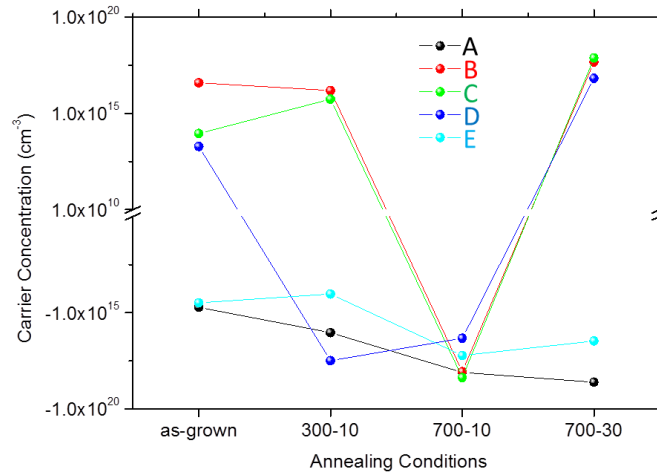


**Figure 5.10** Plot of Hall carrier concentrations for as-grown samples A, B, C, D and E after annealing treatment. The horizontal axis indicates the heat treatment: as-grown, 300°C 10 minutes, 700°C 10 minutes and 700°C 30 minutes.

When annealed at 700°C for 10 min, a high n-type conductivity on the order of  $10^{18} \text{ cm}^{-3}$  was obtained in undoped sample A and was attributed to the activation of the hydrogen donor [193]. These donors are known to originate from the dehydration of adjacent hydroxyl groups incorporated during growth in aqueous solution [194]. In K-doped films, these hydroxyl groups were present together with the  $\text{K}_{\text{Zn}}\text{-H}_i$  complexes. While the  $\text{K}_{\text{Zn}}\text{-H}_i$  complexes can be dissociated and the  $\text{H}_i$  donors can be out-diffused at 300°C, the hydroxyl groups were only removed after the thermal annealing at temperatures of 700°C and above. The removal of hydroxyl groups and the subsequent activation of the hydrogen donors led to overcompensation

and inversion from p-type to n-type as seen in samples B and C with electron concentrations in the order of  $7 - 9 \times 10^{17} \text{ cm}^{-3}$ .

**Table 5.1** Summary of the measured Hall carrier concentrations for samples A, B, C, D and E for various thermal annealing treatments. A positive and negative sign indicates hole and electron concentration ( $\text{cm}^{-3}$ ) respectively, while numbers in parentheses indicate the mobility ( $\text{cm}^2\text{V}^{-1}\text{s}^{-1}$ ).

<b>Annealing treatment</b>	<b>A (No KAc)</b>	<b>B (0.03 M)</b>	<b>C (0.08 M)</b>	<b>D (0.13 M)</b>	<b>E (0.18 M)</b>
<b>As-grown</b>	$-3.99 \times 10^{14}$ (14)	$+2.64 \times 10^{16}$ (0.29)	$+3.23 \times 10^{13}$ (117)	$+1.07 \times 10^{13}$ (85)	$-1.89 \times 10^{14}$ (56)
<b>300°C 10 min</b>	$-8.28 \times 10^{15}$ (31)	$+1.03 \times 10^{16}$ (56)	$+1.98 \times 10^{15}$ (44)	$-1.70 \times 10^{17}$ (110)	$-6.65 \times 10^{13}$ (198)
<b>700°C 10 min</b>	$-9.79 \times 10^{17}$ (13)	$-7.68 \times 10^{17}$ (8.9)	$-8.41 \times 10^{17}$ (5.6)	$-1.18 \times 10^{16}$ (172)	$-1.04 \times 10^{17}$ (17)
<b>700°C 30 min</b>	$-3.09 \times 10^{18}$ (0.74)	$+3.18 \times 10^{17}$ (1.7)	$+2.72 \times 10^{17}$ (3.5)	$+3.70 \times 10^{16}$ (9.7)	$-1.82 \times 10^{16}$ (9.0)

Extending annealing duration at 700°C from 10 to 30 minutes drove out the  $H_i$  and  $K_i$ , and recovered the p-type conductivity with B and C with hole concentrations of  $3.2$  and  $2.8 \times 10^{17} \text{ cm}^{-3}$ , and mobilities of 1.7 and 3.5, respectively. The carrier concentrations for both D and E also shifted from n-type towards p-type as a result of extended annealing duration, but at a slower rate than B and C. The difference in p-type recovery rate could also be understood from the difference in type of K complexes arising from the initial growth conditions. As mentioned earlier, the main form of neutral K complexes changed from  $K_{Zn}\text{-}H_i$  to  $K_{Zn}\text{-}K_i$  for samples from B to E. When these neutral K complexes dissociated, they formed compensating donor and

acceptor states, resulting in highly compensated films. The p-type conductivity could only be observed when these  $H_i$  or  $K_i$  donors were driven out.  $K_i$  only began diffusing at about 300°C while  $H_i$ , is very small in size, diffused at a much lower temperature. This resulted in the first onset at 300°C of p-type conductivity in sample B, which has the lowest concentration of  $K_i$ , and last at in sample D which has the higher  $K_i$  concentration.

Quantification of XPS spectra from as-grown K-doped ZnO films has routinely shown that the atomic percentage of K is less than 0.5%. The XPS atomic percentage is larger than the percentage derived from measured Hall-effect hole concentrations which is usually in the mid  $10^{17} \text{ cm}^{-3}$ , corresponding to an atomic percentage of around 0.05% which is an order of magnitude lower. This suggests that a majority of the K atoms incorporated into the film were electrically inactive, and/or they existed in compensating forms such as  $K_{Zn}$  and  $K_i$ . Therefore, the key to p-type conductivity is to successfully dissociate the neutral K complexes and drive out the  $K_i$  atoms while preserving the K at the substitutional sites. Our results indicate that the best way to achieve these is to use a growth environment that has a low  $K^+/Zn^{2+}$  concentration ratio, followed by a thermal annealing step of 300°C for 10 minutes to dissociate K-based neutral complexes and out-diffused  $K_i$  from the film. Alternatively, if a higher annealing temperature is required, for example for the formation of an ohmic contact on the p-type film, an annealing step at 700°C for an extended duration of 30 min is needed to out-diffuse the H-donors created from the removal of hydroxyl groups.

Finally, it is interesting to note a recently published result, using calibrated SIMS on hydrothermally grown ZnO which has been grown in a high concentrations of KOH and LiOH, typically above 1 M, has also demonstrated moderate dopant concentrations in the range of  $1 \times$

$10^{17}$  to  $1 \times 10^{18} \text{ cm}^{-3}$  [195]. In our work, the saturation of K concentration in the film began when at least 0.08 M KAc was added into the growth solution. After the thermal annealing for extended periods at  $700^\circ\text{C}$ , the final hole concentrations were in the middle range of  $10^{17} \text{ cm}^{-3}$ , which is in the same range of the calibrated SIMS measurements. This suggests a fundamental limit for K incorporation using the aqueous solution route where the maximum concentration of K that can be incorporated is about  $10^{17} - 10^{18} \text{ cm}^{-3}$ .

## 5.5 Summary

A model for the ionic equilibrium concentrations of different species was presented for the aqueous growth solution using  $\text{ZnAc}_2$  and KAc as precursors. The concentration ratio of  $\text{K}^+/\text{Zn}^{2+}$  and solution pH affects the type of dominant K defects incorporated in the lattice. For low  $\text{K}^+/\text{Zn}^{2+}$ , K is incorporated predominantly as  $\text{K}_{\text{Zn}}$  and  $\text{K}_{\text{Zn}}\text{-H}_i$  while for high  $\text{K}^+/\text{Zn}^{2+}$ , K is incorporated predominantly as  $\text{K}_{\text{Zn}}$  and  $\text{K}_{\text{Zn}}\text{-K}_i$ . Both  $\text{K}_{\text{Zn}}\text{-H}_i$  and  $\text{K}_{\text{Zn}}\text{-K}_i$  complexes dissociate at low temperatures below  $300^\circ\text{C}$ , but the  $\text{K}_i$  larger in size only begins to diffuse at  $300^\circ\text{C}$ . Due to the lower diffusion barriers for  $\text{H}_i$  compared to  $\text{K}_i$ , the p-type conductivity of the low  $\text{K}^+/\text{Zn}^{2+}$  samples can be obtained at a lower annealing temperature of  $300^\circ\text{C}$  compared to that of high  $\text{K}^+/\text{Zn}^{2+}$  samples which requires an annealing temperature of  $700^\circ\text{C}$ .

The p-type conductivity is obtained in the range of 0.03 - 0.08 M KAc for both as-grown and  $700^\circ\text{C}$  30 minutes annealed samples. The best as-grown hole concentration of  $2.6 \times 10^{16} \text{ cm}^{-3}$  is obtained for 0.03 M KAc while for  $700^\circ\text{C}$  at 30 min annealed samples, hole concentrations of  $3.2 \times 10^{17} \text{ cm}^{-3}$  for 0.08 M KAc. Results also suggested that the upper limit for p-type doping using this route is about mid- $10^{17} \text{ cm}^{-3}$ .

The best conditions for obtaining p-type conductivity is to use a low  $K^+/Zn^{2+}$  growth environment followed by a thermal annealing of 300°C for 10 minutes to dissociate K-based neutral complexes and diffuse out  $K_i$  from the film. Alternatively for a higher annealing temperature of 700°C, a longer duration of 30 minutes is needed to out-diffuse the H-donors created from the removal of hydroxyl groups.

## Chapter 6 Conclusions and outlook

In this thesis, we have studied in detail the various dopings (intrinsic and foreign, p-type and n-type) and their effects on the properties of ZnO films and nanorods through three explicit examples, which are summarized as following:

Firstly, Ga doped n-type ZnO films with different doping levels have been studied by a simple and widely accessible approach combining THz-TDS and Hall measurement techniques. It is found that doping concentration (carrier concentration) has substantial influence on the effective mass and carrier scattering time. Drude model and its derivatives have been used to extract the effective mass and carrier scattering time from the measured transmission spectra of ZnO films by THz-TDS in the range of 0.1-2 THz. The result shows that electron effective mass varies from  $0.23m_0$  to  $0.26m_0$  when the electron concentration changes from  $5.9 \times 10^{17} \text{ cm}^{-3}$  to  $4.0 \times 10^{19} \text{ cm}^{-3}$ . The carrier concentration dependent characteristic is ascribed to the non-parabolicity of conduction band. It is also noticed that the electron mobility determined by THz-TDS can be 7 times higher than that obtained by Hall measurement, which was explained by free carrier localization mechanism. This work is the first to demonstrate that the effective mass can be obtained from a combine THz-TDS and Hall measurement.

Secondly, the intrinsic doping and their effects on the optical properties of ZnO nanorods grown by low temperature ( $90^\circ\text{C}$ ) solution method have been studied. Two heating methods, i.e. conventional water bath and microwave heating are used and compared. The morphology, intrinsic doping and optical properties of the nanorods obtained within the pH range of 10.07 to 10.9 is investigated in detail using scanning-electron microscopy, photoluminescence, and X-ray photoelectron spectroscopy. It is found that the microwave synthesized ZnO nanorods grow

faster with a more uniform size distribution, which is the result of the instantaneous and uniform heating by microwave. For both microwave and water bath assisted synthesis, the dominant native defects are  $O_i$  and  $V_{Zn}$ . Through 500°C post annealing treatment in vacuum, the out-diffusion of  $O_i$  and  $V_{Zn}$  take place, which leads to the improvement in stoichiometric ratio of oxygen to zinc from 70% - 80% to 55% - 65%. The results show that intrinsic defects density is effectively reduced by microwave assisted synthesis. Together with the fast growth rate, it provides an attractive approach to fabricate less defective and more uniform size distribution of ZnO nanorods on various substrates with high throughput, especially on those substrates that can only survive in low temperature growth environment, such as plastics, polymer and paper. In addition, it has the potential to achieve higher p-type doping concentration, since the self-compensation effect is minimized with lower intrinsic doping level.

Thirdly, a stable p-type ZnO film doped by potassium is presented. The growth condition is optimized through varying the growth parameters like precursor concentration, pH and annealing temperature. It is shown that the concentration ratio of  $K^+/Zn^{2+}$  and the solution pH determine the dominant potassium defects incorporated into the ZnO lattice, where low ratio of  $K^+/Zn^{2+}$  leads to the formation of  $K_{Zn}$  and  $K_{Zn}-H_i$  while high ratio leads to  $K_{Zn}$  and  $K_{Zn}-K_i$ . The result also shows that the post thermal annealing at 300°C is decisive in obtaining stable p-type doping as it helps to dissociate the  $K_{Zn}-H_i$  neutral complexes and out-diffuse  $H_i$  and  $K_i$  from the ZnO film. With a higher annealing temperature at 700°C for 30 minutes, the H-donors originating from the hydroxyl groups are also out-diffused. The p-type conductivity was obtained in the KAc concentration range of 0.03 - 0.08 M for both as-grown samples and samples annealed at 700°C for 30 minutes. For the as-grown samples, the highest hole concentration obtained is  $2.6 \times 10^{16}$



$\text{cm}^{-3}$  with 0.03 M KAc. While, for samples annealed at  $700^\circ\text{C}$  for 30 minutes, the highest hole concentration was  $3.2 \times 10^{17} \text{ cm}^{-3}$  with 0.08 M KAc.

To conclude, this work provides a comprehensive study on the doping of ZnO films and nanorods by targeting on the current challenges and issues facing each doping type. The results obtained in the n-type ZnO films provide an effective way in obtaining carrier concentration dependent effective mass, which has not been measured before and which are important for accurate design of optoelectronic devices. Another contribution is the systematic comparison of the properties of ZnO nanorods prepared by conventional water bath synthesis and novel microwave synthesis in solution which is done for the first time. The p-type ZnO doped by potassium in solution suggests a simple, robust, and low-cost method for stable p-type doping in ZnO films, with good promise for use in optoelectronic device.

Finally, some of the possible directions for the future work of this study are recommended:

- Microwave assisted synthesis has been proven to be able to grow ZnO with lower defect density. As the microwave system is equipped with a pump, which can provide good circulation of air and it is able to cool down the solution from  $90^\circ\text{C}$  to  $60^\circ\text{C}$  in less than three minutes. As it can heat up and cool down fast, multi-cycles of growth by alternating the growth temperature between high and low will be an effective way to lower the defect density and further improve the crystal quality, as the low temperature promotes the growth while high temperature growth helps to decrease the defect density.
- The solubility of  $\text{K}^+$  in solution is only mid- $10^{18} \text{ cm}^{-3}$ , which is not sufficient to provide a good p-type conductive layer for device application. Co-doping with sodium is a good approach

to obtain ZnO film with a higher hole concentration. Sodium citrate as well as potassium acetate and zinc acetate will be chosen as the precursors. Sodium citrate not only provides the promising p-type acceptor Na to the ZnO film but also serves as a surfactant which promotes lateral growth of ZnO. So a high quality p-type ZnO film with high carrier concentration is expected to be obtained, which will be desirable for device application.

- The ultimate goal of the community in investigating p-type doped ZnO is to achieve fascinating electronic and photonic devices. With the potassium and sodium co-doped p-type ZnO film in hand, it is attractive to fabricate p-n junction based photonics devices such as light emitting diodes to examine the performance. The success of our group in demonstrating homojunction ZnO nanorods LEDs with K-doped ZnO as p-layer on GaN substrate makes the ZnO film based LEDs more appealing and promising.

## Bibliography

- [1] U. Özgür, Y. I. Alivov, C. Liu, A. Teke, M. A. Reshchikov, S. Doğan, V. Avrutin, S.-J. Cho, and H. Morkoç, “A comprehensive review of ZnO materials and devices,” *J. Appl. Phys.*, vol. 98, no. 4, p. 041301, Aug. 2005.
- [2] Cole W. Litton, Thomas C. Collins, Donald C. Reynolds, *Zinc Oxide Materials for Electronic and Optoelectronic Device Applications*. ISBN: 978-0-470-51971-4, John Wiley & Sons, Mar. 2011.
- [3] Y. Liu, M. Zhong, G. Shan, Y. Li, B. Huang, and G. Yang, “Biocompatible ZnO/Au nanocomposites for ultrasensitive DNA detection using resonance Raman scattering,” *J. Phys. Chem. B*, vol. 112, no. 20, pp. 6484–9, May 2008.
- [4] H. Morkoç and Ü. Özgür, *Zinc Oxide: Fundamentals, Materials and Device Technology*. ISBN: 9783527623945, John Wiley & Sons, Sep. 2009.
- [5] A. Di Trollo, C. Veroli, A. M. Testa, and D. Fiorani, “Ferromagnetism above room temperature in Mn-doped ZnO thin films,” *Superlattices Microstruct.*, vol. 46, no. 1–2, pp. 101–106, Jul. 2009.
- [6] Y.-S. Choi, J.-W. Kang, D.-K. Hwang, and S.-J. Park, “Recent Advances in ZnO-Based Light-Emitting Diodes,” *IEEE Trans. Electron Devices*, vol. 57, no. 1, pp. 26–41, Jan. 2010.
- [7] M. Willander, O. Nur, J. R. Sadaf, M. I. Qadir, S. Zaman, A. Zainelabdin, N. Bano, and I. Hussain, “Luminescence from Zinc Oxide Nanostructures and Polymers and their Hybrid Devices,” *Materials (Basel)*, vol. 3, no. 4, pp. 2643–2667, Apr. 2010.
- [8] C. Klingshirn, J. Fallert, H. Zhou, J. Sartor, C. Thiele, F. Maier-Flaig, D. Schneider, and H. Kalt, “65 years of ZnO research - old and very recent results,” *Phys. status solidi*, vol. 247, no. 6, pp. 1424–1447, Apr. 2010.
- [9] Z. C. Feng, *Handbook of Zinc Oxide and Related Materials: Volume One, Materials*. Taylor & Francis, Sep. 2012.
- [10] William M. Haynes, *CRC Handbook of Chemistry and Physics, 93rd Edition*. CRC Press, Jun. 2012.
- [11] J. C. Phillips, *Bonds and bands in semiconductors*. Academic Press, 1973.
- [12] C. Klingshirn, “ZnO: material, physics and applications,” *Chemphyschem*, vol. 8, no. 6, pp. 782–803, Apr. 2007.

- [13] W. Lu, P. Yang, W. D. Song, G. M. Chow, and J. S. Chen, "Control of oxygen octahedral rotations and physical properties in SrRuO<sub>3</sub> films," *Phys. Rev. B*, vol. 88, no. 21, p. 214115, Dec. 2013.
- [14] J. B. Yi, C. C. Lim, G. Z. Xing, H. M. Fan, L. H. Van, S. L. Huang, K. S. Yang, X. L. Huang, X. B. Qin, B. Y. Wang, T. Wu, L. Wang, H. T. Zhang, X. Y. Gao, T. Liu, A. T. S. Wee, Y. P. Feng, and J. Ding, "Ferromagnetism in Dilute Magnetic Semiconductors through Defect Engineering: Li-Doped ZnO," *Phys. Rev. Lett.*, vol. 104, no. 13, p. 137201, Mar. 2010.
- [15] C. G. Van de Walle, "Defect analysis and engineering in ZnO," *Phys. B Condens. Matter*, vol. 308–310, pp. 899–903, Dec. 2001.
- [16] E.-C. Lee and K. Chang, "Possible p-type doping with group-I elements in ZnO," *Phys. Rev. B*, vol. 70, no. 11, p. 115210, Sep. 2004.
- [17] M. Willander, O. Nur, J. R. Sadaf, M. I. Qadir, S. Zaman, A. Zainelabdin, N. Bano, and I. Hussain, "Luminescence from Zinc Oxide Nanostructures and Polymers and their Hybrid Devices," *Materials (Basel)*, vol. 3, no. 4, pp. 2643–2667, Apr. 2010.
- [18] C. Kittel, *Introduction to solid state physics*. New York: Wiley, 2005.
- [19] C. G. Van de Walle, "First-principles calculations for defects and impurities: Applications to III-nitrides," *J. Appl. Phys.*, vol. 95, no. 8, p. 3851, Mar. 2004.
- [20] C. H. Ahn, Y. Y. Kim, D. C. Kim, S. K. Mohanta, and H. K. Cho, "A comparative analysis of deep level emission in ZnO layers deposited by various methods," *J. Appl. Phys.*, vol. 105, no. 1, p. 013502, Jan. 2009.
- [21] Z. Fang, Y. Wang, D. Xu, Y. Tan, and X. Liu, "Blue luminescent center in ZnO films deposited on silicon substrates," *Opt. Mater. (Amst)*, vol. 26, no. 3, pp. 239–242, Aug. 2004.
- [22] K. Vanheusden, C. H. Seager, W. L. Warren, D. R. Tallant, and J. A. Voigt, "Correlation between photoluminescence and oxygen vacancies in ZnO phosphors," *Appl. Phys. Lett.*, vol. 68, no. 3, p. 403, Jan. 1996.
- [23] Q. X. Zhao, P. Klason, M. Willander, H. M. Zhong, W. Lu, and J. H. Yang, "Deep-level emissions influenced by O and Zn implantations in ZnO," *Appl. Phys. Lett.*, vol. 87, no. 21, p. 211912, Nov. 2005.
- [24] T. M. Borseth, B. G. Svensson, A. Y. Kuznetsov, P. Klason, Q. X. Zhao, and M. Willander, "Identification of oxygen and zinc vacancy optical signals in ZnO," *Appl. Phys. Lett.*, vol. 89, no. 26, p. 262112, Dec. 2006.

- [25] D. Zwingel, "Trapping and recombination processes in the thermoluminescence of Li-doped ZnO single crystals," *J. Lumin.*, vol. 5, no. 6, pp. 385–405, Dec. 1972.
- [26] O. F. Schirmer and D. Zwingel, "The yellow luminescence of zinc oxide," *Solid State Commun.*, vol. 8, no. 19, pp. 1559–1563, Oct. 1970.
- [27] X. L. Wu, G. G. Siu, C. L. Fu, and H. C. Ong, "Photoluminescence and cathodoluminescence studies of stoichiometric and oxygen-deficient ZnO films," *Appl. Phys. Lett.*, vol. 78, no. 16, p. 2285, Apr. 2001.
- [28] M. Gomi, N. Oohira, K. Ozaki, and M. Koyano, "Photoluminescent and Structural Properties of Precipitated ZnO Fine Particles," *Jpn. J. Appl. Phys.*, vol. 42, no. Part 1, No. 2A, pp. 481–485, Feb. 2003.
- [29] C. B. Tay, "*Growth Of Zinc Oxide Nanostructures and Films and p-Doping Of Films In Aqueous Solution*," p. 8, 2009.
- [30] T. Minami, H. Sato, K. Ohashi, T. Tomofuji, and S. Takata, "Conduction mechanism of highly conductive and transparent zinc oxide thin films prepared by magnetron sputtering," *J. Cryst. Growth*, vol. 117, no. 1–4, pp. 370–374, Feb. 1992.
- [31] Y. Ma, "Control of conductivity type in undoped ZnO thin films grown by metalorganic vapor phase epitaxy," *J. Appl. Phys.*, vol. 95, no. 11, p. 6268, May 2004.
- [32] D. Andeen, J. H. Kim, F. F. Lange, G. K. L. Goh, and S. Tripathy, "Lateral Epitaxial Overgrowth of ZnO in Water at 90 °C," *Adv. Funct. Mater.*, vol. 16, no. 6, pp. 799–804, Apr. 2006.
- [33] D. Ehrentraut, H. Sato, Y. Kagamitani, H. Sato, A. Yoshikawa, and T. Fukuda, "Solvothermal growth of ZnO," *Prog. Cryst. Growth Charact. Mater.*, vol. 52, no. 4, pp. 280–335, Dec. 2006.
- [34] M. Lorenz, E. M. Kaidashev, H. von Wenckstern, V. Riede, C. Bundesmann, D. Spemann, G. Benndorf, H. Hochmuth, A. Rahm, H.-C. Semmelhack, and M. Grundmann, "Optical and electrical properties of epitaxial (Mg,Cd)<sub>x</sub>Zn<sub>1-x</sub>O, ZnO, and ZnO:(Ga,Al) thin films on c-plane sapphire grown by pulsed laser deposition," *Solid. State. Electron.*, vol. 47, no. 12, pp. 2205–2209, Dec. 2003.
- [35] H. Morkoç and Ü. Özgür, *Zinc Oxide: Fundamentals, Materials and Device Technology*. Wiley, 2009.
- [36] M. Gabás, A. Landa-Cánovas, J. Luis Costa-Krämer, F. Agulló-Rueda, A. R. González-Elipe, P. Díaz-Carrasco, J. Hernández-Moro, I. Lorite, P. Herrero, P. Castellero, A. Barranco, and J. Ramón Ramos-Barrado, "Differences in n-type doping efficiency between Al- and Ga-ZnO films," *J. Appl. Phys.*, vol. 113, no. 16, p. 163709, Apr. 2013.

- [37] A. Teke, Ü. Özgür, S. Doğan, X. Gu, H. Morkoç, B. Nemeth, J. Nause, and H. Everitt, “Excitonic fine structure and recombination dynamics in single-crystalline ZnO,” *Phys. Rev. B*, vol. 70, no. 19, p. 195207, Nov. 2004.
- [38] D. C. Look and B. Claflin, “P-type doping and devices based on ZnO,” *Phys. status solidi*, vol. 241, no. 3, pp. 624–630, Mar. 2004.
- [39] H. Alves, D. Pfisterer, A. Zeuner, T. Riemann, J. Christen, D. M. Hofmann, and B. K. Meyer, “Optical investigations on excitons bound to impurities and dislocations in ZnO,” *Opt. Mater. (Amst.)*, vol. 23, no. 1–2, pp. 33–37, Jul. 2003.
- [40] S. Y. Myong, S. J. Baik, C. H. Lee, W. Y. Cho, and K. S. Lim, “Extremely Transparent and Conductive ZnO:Al Thin Films Prepared by Photo-Assisted Metalorganic Chemical Vapor Deposition (photo-MOCVD) Using  $\text{AlCl}_3(6\text{H}_2\text{O})$  as New Doping Material,” *Jpn. J. Appl. Phys.*, vol. 36, no. Part 2, No. 8B, pp. L1078–L1081, Aug. 1997.
- [41] H. Agura, A. Suzuki, T. Matsushita, T. Aoki, and M. Okuda, “Low resistivity transparent conducting Al-doped ZnO films prepared by pulsed laser deposition,” *Thin Solid Films*, vol. 445, no. 2, pp. 263–267, Dec. 2003.
- [42] H. J. Ko, Y. F. Chen, S. K. Hong, H. Wensch, T. Yao, and D. C. Look, “Ga-doped ZnO films grown on GaN templates by plasma-assisted molecular-beam epitaxy,” *Appl. Phys. Lett.*, vol. 77, no. 23, p. 3761, Dec. 2000.
- [43] B. M. Ataev, A. M. Bagamadova, A. M. Djabrailov, V. V. Mamedov, and R. A. Rabadanov, “Highly conductive and transparent Ga-doped epitaxial ZnO films on sapphire by CVD,” *Thin Solid Films*, vol. 260, no. 1, pp. 19–20, May 1995.
- [44] D. H. Kim, N. G. Cho, H. G. Kim, and W.-Y. Choi, “Structural and Electrical Properties of Indium Doped ZnO Thin Films Fabricated by RF Magnetron Sputtering,” *J. Electrochem. Soc.*, vol. 154, no. 11, p. H939, Nov. 2007.
- [45] B. K. Meyer, J. Sann, D. M. Hofmann, C. Neumann, and A. Zeuner, “Shallow donors and acceptors in ZnO,” *Semicond. Sci. Technol.*, vol. 20, no. 4, pp. S62–S66, Apr. 2005.
- [46] J. Hu and R. G. Gordon, “Textured fluorine-doped ZnO films by atmospheric pressure chemical vapor deposition and their use in amorphous silicon solar cells,” *Sol. Cells*, vol. 30, no. 1–4, pp. 437–450, May 1991.
- [47] S. Zhang, S.-H. Wei, and A. Zunger, “Intrinsic n-type versus p-type doping asymmetry and the defect physics of ZnO,” *Phys. Rev. B*, vol. 63, no. 7, p. 075205, Jan. 2001.
- [48] E. Chikoidze, M. Nolan, M. Modreanu, V. Sallet, and P. Galtier, “Effect of chlorine doping on electrical and optical properties of ZnO thin films,” *Thin Solid Films*, vol. 516, no. 22, pp. 8146–8149, Sep. 2008.

- [49] J. D. Ye, S. L. Gu, S. M. Zhu, S. M. Liu, Y. D. Zheng, R. Zhang, and Y. Shi, “Fermi-level band filling and band-gap renormalization in Ga-doped ZnO,” *Appl. Phys. Lett.*, vol. 86, no. 19, p. 192111, May 2005.
- [50] T. Minami, T. Yamamoto, and T. Miyata, “Highly transparent and conductive rare earth-doped ZnO thin films prepared by magnetron sputtering,” *Thin Solid Films*, vol. 366, no. 1–2, pp. 63–68, May 2000.
- [51] T. Minami, H. Sato, H. Nanto, and S. Takata, “Highly Conductive and Transparent Silicon Doped Zinc Oxide Thin Films Prepared by RF Magnetron Sputtering,” *Jpn. J. Appl. Phys.*, vol. 25, no. Part 2, No. 9, pp. L776–L779, Sep. 1986.
- [52] R. Wang, L. L. H. King, and A. W. Sleight, “Highly conducting transparent thin films based on zinc oxide,” *J. Mater. Res.*, vol. 11, no. 07, pp. 1659–1664, Jan. 2011.
- [53] B. Ataev, A. Bagamadova, V. Mamedov, A. Omaev, and M. Rabadanov, “Highly conductive and transparent thin ZnO films prepared in situ in a low pressure system,” *J. Cryst. Growth*, vol. 198–199, pp. 1222–1225, Mar. 1999.
- [54] J. G. Reynolds and C. L. Reynolds, “Progress in ZnO Acceptor Doping: What Is the Best Strategy?,” *Adv. Condens. Matter Phys.*, vol. 2014, 2014.
- [55] T. Yamamoto and H. Katayama, “Solution Using a Codoping Method to Unipolarity for the Fabrication of p-Type ZnO,” *Jpn. J. Appl. Phys.*, vol. 38, no. Part 2, No. 2B, pp. L166–L169, Feb. 1999.
- [56] S. J. Pearton, D. P. Norton, K. Ip, Y. W. Heo, and T. Steiner, “Recent advances in processing of ZnO,” *J. Vac. Sci. Technol. B Microelectron. Nanom. Struct.*, vol. 22, no. 3, p. 932, Apr. 2004.
- [57] V. Avrutin, D. J. Silversmith, and H. Morkoç, “Doping Asymmetry Problem in ZnO: Current Status and Outlook,” *Proc. IEEE*, vol. 98, no. 7, pp. 1269–1280, Jul. 2010.
- [58] V. Avrutin, D. J. Silversmith, and H. Morkoç, “Doping Asymmetry Problem in ZnO: Current Status and Outlook,” *Proc. IEEE*, vol. 98, no. 7, pp. 1269–1280, Jul. 2010.
- [59] C. H. Park, S. B. Zhang, and S.-H. Wei, “Origin of p-type doping difficulty in ZnO: The impurity perspective,” *Phys. Rev. B*, vol. 66, no. 7, p. 073202, Aug. 2002.
- [60] Y. J. Zeng, Z. Z. Ye, J. G. Lu, W. Z. Xu, L. P. Zhu, B. H. Zhao, and S. Limpijumnong, “Identification of acceptor states in Li-doped p-type ZnO thin films,” *Appl. Phys. Lett.*, vol. 89, no. 4, p. 042106, Jul. 2006.
- [61] S. S. Lin, J. G. Lu, Z. Z. Ye, H. P. He, X. Q. Gu, L. X. Chen, J. Y. Huang, and B. H. Zhao, “p-type behavior in Na-doped ZnO films and ZnO homojunction light-emitting diodes,” *Solid State Commun.*, vol. 148, no. 1–2, pp. 25–28, Oct. 2008.

- [62] Y. Yan, M. M. Al-Jassim, and S.-H. Wei, "Doping of ZnO by group-IB elements," *Appl. Phys. Lett.*, vol. 89, no. 18, p. 181912, Oct. 2006.
- [63] E. Mollwo, G. Müller, and P. Wagner, "Energetische lage des Cu-akzeptorniveaus in ZnO-Einkristallen," *Solid State Commun.*, vol. 13, no. 8, pp. 1283–1287, Oct. 1973.
- [64] F. Reuss, "Optical investigations on the annealing behavior of gallium- and nitrogen-implanted ZnO," *J. Appl. Phys.*, vol. 95, no. 7, p. 3385, Mar. 2004.
- [65] F. X. Xiu, Z. Yang, L. J. Mandalapu, J. L. Liu, and W. P. Beyermann, "p-type ZnO films with solid-source phosphorus doping by molecular-beam epitaxy," *Appl. Phys. Lett.*, vol. 88, no. 5, p. 052106, Jan. 2006.
- [66] W.-J. Lee, J. Kang, and K. J. Chang, "Electronic structure of phosphorus dopants in ZnO," *Phys. B Condens. Matter*, vol. 376–377, pp. 699–702, Apr. 2006.
- [67] Y. R. Ryu, T. S. Lee, and H. W. White, "Properties of arsenic-doped p-type ZnO grown by hybrid beam deposition," *Appl. Phys. Lett.*, vol. 83, no. 1, p. 87, Jul. 2003.
- [68] S. Limpijumnong, S. Zhang, S.-H. Wei, and C. Park, "Doping by Large-Size-Mismatched Impurities: The Microscopic Origin of Arsenic- or Antimony-Doped p-Type Zinc Oxide," *Phys. Rev. Lett.*, vol. 92, no. 15, p. 155504, Apr. 2004.
- [69] C. H. Park, S. B. Zhang, and S.-H. Wei, "Origin of p-type doping difficulty in ZnO: The impurity perspective," *Phys. Rev. B*, vol. 66, no. 7, p. 073202, Aug. 2002.
- [70] F. X. Xiu, Z. Yang, L. J. Mandalapu, D. T. Zhao, and J. L. Liu, "Photoluminescence study of Sb-doped p-type ZnO films by molecular-beam epitaxy," *Appl. Phys. Lett.*, vol. 87, no. 25, p. 252102, Dec. 2005.
- [71] J. Wu, J. Hu, L. Shao, J. Xu, K. Song, and P. Zheng, "First-principle investigation of K–N dual-acceptor codoping for p-ZnO," *Mater. Sci. Semicond. Process.*, Apr. 2014.
- [72] Y. R. Ryu, J. A. Lubguban, T. S. Lee, H. W. White, T. S. Jeong, C. J. Youn, and B. J. Kim, "Excitonic ultraviolet lasing in ZnO-based light emitting devices," *Appl. Phys. Lett.*, vol. 90, no. 13, p. 131115, Mar. 2007.
- [73] K. Nakahara, S. Akasaka, H. Yuji, K. Tamura, T. Fujii, Y. Nishimoto, D. Takamizu, A. Sasaki, T. Tanabe, H. Takasu, H. Amaike, T. Onuma, S. F. Chichibu, A. Tsukazaki, A. Ohtomo, and M. Kawasaki, "Nitrogen doped  $Mg_xZn_{1-x}O/ZnO$  single heterostructure ultraviolet light-emitting diodes on ZnO substrates," *Appl. Phys. Lett.*, vol. 97, no. 1, p. 013501, Jul. 2010.
- [74] X. S. Nguyen, C. B. Tay, E. A. Fitzgerald, and S. J. Chua, "ZnO Coaxial Nanorod Homojunction UV Light Emitting Diodes Prepared by Aqueous Solution Method," *small*, vol. 8, no. 8, pp. 1204–1208, 2012.



- [75] A. S aedi, R. Yousefi, F. Jamali-Sheini, M. Cheraghizade, A. Khorsand Zak, and N. M. Huang, "Optical and electrical properties of p-type Li-doped ZnO nanowires," *Superlattices Microstruct.*, vol. 61, pp. 91–96, Sep. 2013.
- [76] G.-Y. Huang, C.-Y. Wang, and J.-T. Wang, "First-principles study of extensive dopants in wurtzite ZnO," *Phys. B Condens. Matter*, vol. 405, no. 1, pp. 158–160, Jan. 2010.
- [77] M. A. Verges, A. Mifsud, and C. J. Serna, "Formation of rod-like zinc oxide microcrystals in homogeneous solutions," *J. Chem. Soc. Faraday Trans.*, vol. 86, no. 6, p. 959, Jan. 1990.
- [78] B. Weintraub, Z. Zhou, Y. Li, and Y. Deng, "Solution synthesis of one-dimensional ZnO nanomaterials and their applications," *Nanoscale*, vol. 2, no. 9, pp. 1573–87, Sep. 2010.
- [79] C. B. Tay, S. J. Chua, and K. P. Loh, "Investigation of morphology and photoluminescence of hydrothermally grown ZnO nanorods on substrates pre-coated with ZnO nanoparticles," *J. Cryst. Growth*, vol. 311, no. 5, pp. 1278–1284, Feb. 2009.
- [80] Z. Wang, X.-F. Qian, J. Yin, and Z.-K. Zhu, "Large-scale fabrication of tower-like, flower-like, and tube-like ZnO arrays by a simple chemical solution route.," *Langmuir*, vol. 20, no. 8, pp. 3441–8, Apr. 2004.
- [81] D. P. Norton, Y. W. Heo, M. P. Ivill, K. Ip, S. J. Pearton, M. F. Chisholm, and T. Steiner, "ZnO: growth, doping & processing", *Mater. today*, vol. 7, no. 6, pp. 34–40, 2004.
- [82] A. Ko odziejczak-Radzimska and T. Jesionowski, "Zinc Oxide—From Synthesis to Application: A Review," *Materials (Basel)*, vol. 7, no. 4, pp. 2833–2881, Apr. 2014.
- [83] L. Schmidt-Mende and J. L. MacManus-Driscoll, "ZnO-nanostructures, defects, and devices", *Mater. today*, vol. 10, no. 5, pp. 40–48, 2007.
- [84] G. Hodes, *Chemical Solution Deposition Of Semiconductor Films*. Rehovot, Israel, pp. 12–14, 2002.
- [85] M. Bishop, *An Introduction to Chemistry*. Chiral Publishing Company, p. 836, 2006.
- [86] W. Beckmann, Ed. *Crystallization: Basic Concepts and Industrial Applications*, John Wiley & Sons, 2013.
- [87] A. Mersmann, *Crystallization Technology Handbook*, Second. Garcbing, Germany: CRC Press, p. 840, 2001.
- [88] I. Sunagawa, *Crystals: Growth, Morphology & Perfection*. Cambridge University Press, 2005.

- [89] S. Xu and Z. L. Wang, "One-dimensional ZnO nanostructures: Solution growth and functional properties," *Nano Res.*, vol. 4, no. 11, pp. 1013–1098, Aug. 2011.
- [90] K. Govender, D. S. Boyle, P. B. Kenway, and P. O. Brien, "Understanding the factors that govern the deposition and morphology of thin films of ZnO from aqueous solution" pp. 2575–2591, 2004.
- [91] A. Kawska, P. Duchstein, O. Hochrein, and D. Zahn, "Atomistic mechanisms of ZnO aggregation from ethanolic solution: ion association, proton transfer, and self-organization.," *Nano Lett.*, vol. 8, no. 8, pp. 2336–40, Aug. 2008.
- [92] M. Dhanaraj, Govindhan and Byrappa, Kullaiah and Prasad, Vishwanath and Dudley, *Handbook of Crystal Growth*. Springer, 2010.
- [93] L. N. Dem, D. V Kostomarov, and I. P. Kuz, "Chemistry and Kinetics of ZnO Growth from Alkaline Hydrothermal Solutions," *Inorganic Materials*, vol. 38, no. 2, pp. 124–131, 2002.
- [94] A. Ohtomo and A. Tsukazaki, "Pulsed laser deposition of thin films and superlattices based on ZnO," *Semicond. Sci. Technol.*, vol. 20, no. 4, pp. S1–S12, Apr. 2005.
- [95] L. E. Greene, M. Law, D. H. Tan, M. Montano, J. Goldberger, G. Somorjai, and P. Yang, "General route to vertical ZnO nanowire arrays using textured ZnO seeds," *Nano Lett.*, vol. 5, no. 7, pp. 1231–1236, 2005.
- [96] C. Pacholski, A. Kornowski, and H. Weller, "Self-assembly of ZnO: from nanodots to nanorods.," *Angew. Chem. Int. Ed. Engl.*, vol. 41, no. 7, pp. 1188–91, Apr. 2002.
- [97] H. M. Smith and A. F. Turner, "Vacuum Deposited Thin Films Using a Ruby Laser," *Appl. Opt.*, vol. 4, no. 1, p. 147, Jan. 1965.
- [98] D. Dijkkamp, T. Venkatesan, X. D. Wu, S. a. Shaheen, N. Jisrawi, Y. H. Min-Lee, W. L. McLean, and M. Croft, "Preparation of Y-Ba-Cu oxide superconductor thin films using pulsed laser evaporation from high T<sub>c</sub> bulk material," *Appl. Phys. Lett.*, vol. 51, no. 8, p. 619, 1987.
- [99] J. a Greer, "History and current status of commercial pulsed laser deposition equipment," *J. Phys. D. Appl. Phys.*, vol. 47, no. 3, p. 034005, Jan. 2014.
- [100] Carl E. Patton, "Magnetization Dynamics Group - PLD System." Available: [http://www2.physics.colostate.edu/groups/PattonGroup/systems/pld\\_desc.html](http://www2.physics.colostate.edu/groups/PattonGroup/systems/pld_desc.html). Colorado State University
- [101] R. Eason, "Pulsed Laser Deposition of Thin Films: Applications-Led Growth of Functional Materials" John Wiley & Sons, Inc., 2006.

- [102] D. B. Chrisey and G. K. Hubler, Pulsed Laser Deposition of Thin Films. Wiley-VCH, 2003.
- [103] M. Lorenz, Chapter 7 Pulsed Laser Deposition of ZnO–Based Thin Films in *Transparent Conductive Zinc Oxide: Basics and Applications in Thin Film Solar Cells*. Springer, 2008.
- [104] J. S. Horwitz, Film Nucleation and Film Growth in Pulsed Laser Deposition in *Pulsed Laser Deposition of Thin Films*. Wiley, 1994.
- [105] M. Lorenz, Transparent Conductive Zinc Oxide, vol. 104. Berlin, Heidelberg: Springer Berlin Heidelberg, 2008.
- [106] Anders Werner Bredvei Skilbred Harald Fjeld, Scanning Electron Microscopy, Lecture notes (MENA3100), University of Oslo, Feb. 2009.
- [107] B. K. Meyer, H. Alves, D. M. Hofmann, W. Kriegseis, D. Forster, F. Bertram, J. Christen, A. Hoffmann, M. Straßburg, M. Dworzak, U. Haboeck, and A. V. Rodina, “Bound exciton and donor–acceptor pair recombinations in ZnO,” *Phys. status solidi*, vol. 241, no. 2, pp. 231–260, Feb. 2004.
- [108] C. F. Klingshirn, A. Waag, A. Hoffmann, and J. Geurts, Zinc Oxide: From Fundamental Properties Towards Novel Applications. Springer Science & Business Media, p. 313, 2010.
- [109] M. R. Wagner, G. Callsen, J. S. Reparaz, J.-H. Schulze, R. Kirste, M. Cobet, I. A. Ostapenko, S. Rodt, C. Nenstiel, M. Kaiser, A. Hoffmann, A. V. Rodina, M. R. Phillips, S. Lautenschläger, S. Eisermann, and B. K. Meyer, “Bound excitons in ZnO: Structural defect complexes versus shallow impurity centers,” *Phys. Rev. B*, vol. 84, no. 3, p. 035313, Jul. 2011.
- [110] R. Elliott, “Intensity of Optical Absorption by Excitons,” *Phys. Rev.*, vol. 108, no. 6, pp. 1384–1389, Dec. 1957.
- [111] C. F. Klingshirn, *Semiconductor Optics*. Springer Science & Business Media, p. 837, 2007.
- [112] A. Teke, Ü. Özgür, S. Doğan, X. Gu, H. Morkoç, B. Nemeth, J. Nause, and H. Everitt, “Excitonic fine structure and recombination dynamics in single-crystalline ZnO,” *Phys. Rev. B*, vol. 70, no. 19, p. 195207, Nov. 2004.
- [113] A. B. Djurisić and Y. H. Leung, “Optical properties of ZnO nanostructures,” *Small*, vol. 2, no. 8–9, pp. 944–61, Aug. 2006.
- [114] J. F. Muth, R. M. Kolbas, A. K. Sharma, S. Oktyabrsky, and J. Narayan, “Excitonic structure and absorption coefficient measurements of ZnO single crystal epitaxial films deposited by pulsed laser deposition,” *J. Appl. Phys.*, vol. 85, no. 11, p. 7884, Jun. 1999.

- [115] A. Einstein, “Über einen die Erzeugung und Verwandlung des Lichtes betreffenden heuristischen Gesichtspunkt,” *Ann. Phys.*, vol. 322, no. 6, pp. 132–148, 1905.
- [116] B. V. Crist, *Handbook of Monochromatic XPS Spectra: The elements and native oxides*. Wiley, p. 548, 2000.
- [117] S. J. Wang, A. C. H. Huan, Y. L. Foo, J. W. Chai, J. S. Pan, Q. Li, Y. F. Dong, Y. P. Feng, and C. K. Ong, “Energy-band alignments at  $\text{ZrO}_2/\text{Si}$ ,  $\text{SiGe}$ , and  $\text{Ge}$  interfaces,” *Appl. Phys. Lett.*, vol. 85, no. 19, p. 4418, Nov. 2004.
- [118] F. Bart, M. J. Guitteta, M. Henriot, N. Thromata, M. Gautier, and J. P. Duraud, “Surface analysis of wide gap insulators with XPS,” *J. Electron Spectros. Relat. Phenomena*, vol. 69, no. 3, pp. 245–258, Oct. 1994.
- [119] “CASAXPS software user manual,” Casa Software Ltd., 2006.
- [120] D. Briggs and M. P. Seah, *Practical Surface Analysis: Auger and X-ray photoelectron spectroscopy*. Wiley, p. 657, 1990.
- [121] B. Ferguson and X.-C. Zhang, “Materials for terahertz science and technology.,” *Nat. Mater.*, vol. 1, no. 1, pp. 26–33, Sep. 2002.
- [122] M. Tonouchi, “Cutting-edge terahertz technology,” *Nat. Photonics*, vol. 1, no. 2, pp. 97–105, Feb. 2007.
- [123] W. Kaiser, *Ultrashort laser pulses and applications*. Springer, p. 424, 1988.
- [124] G. Mourou, “Picosecond microwave pulses generated with a subpicosecond laser-driven semiconductor switch,” *Appl. Phys. Lett.*, vol. 39, no. 4, p. 295, Aug. 1981.
- [125] G. Grüner, *Millimeter and submillimeter wave spectroscopy of solids*. Springer, p. 286, 1998.
- [126] C. A. Schmuttenmaer, “Exploring dynamics in the far-infrared with terahertz spectroscopy.,” *Chem. Rev.*, vol. 104, no. 4, pp. 1759–79, Apr. 2004.
- [127] B. Ferguson and X.-C. Zhang, “Materials for terahertz science and technology.,” *Nat. Mater.*, vol. 1, no. 1, pp. 26–33, Sep. 2002.
- [128] M. Tonouchi, “Cutting-edge terahertz technology,” *Nat. Photonics*, vol. 1, no. 2, pp. 97–105, Feb. 2007.
- [129] Y.-S. Lee, *Principles of Terahertz Science and Technology: Proceedings of the International Conference, Held in Mainz, Germany, June 5-9, 1979*. Springer Science & Business Media, p. 352, 2009.

- [130] X. H. Zhang, H. C. Guo, A. M. Yong, J. D. Ye, S. T. Tan, and X. W. Sun, "Terahertz dielectric response and optical conductivity of n-type single-crystal ZnO epilayers grown by metalorganic chemical vapor deposition," *J. Appl. Phys.*, vol. 107, no. 3, p. 033101, Feb. 2010.
- [131] J. B. Baxter and C. A. Schmuttenmaer, "Conductivity of ZnO nanowires, nanoparticles, and thin films using time-resolved terahertz spectroscopy," *J. Phys. Chem. B*, vol. 110, no. 50, pp. 25229–39, Dec. 2006.
- [132] M. Lim, S.-J. Choi, G.-S. Lee, M.-L. Seol, Y. Do, Y.-K. Choi, and H. Han, "Terahertz time-domain spectroscopy of anisotropic complex conductivity tensors in silicon nanowire films," *Appl. Phys. Lett.*, vol. 100, no. 21, p. 211102, May 2012.
- [133] A. Gauthier-Brun, J. H. Teng, E. Dogheche, W. Liu, A. Gokarna, M. Tonouchi, S. J. Chua, and D. Decoster, "Properties of In<sub>x</sub>Ga<sub>1-x</sub>N films in terahertz range," *Appl. Phys. Lett.*, vol. 100, no. 7, p. 071913, Feb. 2012.
- [134] N. Katzenellenbogen and D. Grischkowsky, "Electrical characterization to 4 THz of N- and P-type GaAs using THz time-domain spectroscopy," *Appl. Phys. Lett.*, vol. 61, no. 7, p. 840, Aug. 1992.
- [135] L. Hongwei, S. Cheng, L. Junpeng, Z. Minrui, L. K. Yong, N. Mathews, S. G. Mhaisalkar, T. S. Hai, Z. Xinhai, and S. C. Haur, "Improved electrical property of Sb-doped SnO<sub>2</sub> nanonets as measured by contact and non-contact approaches," *RSC Adv.*, vol. 2, no. 25, p. 9590, Sep. 2012.
- [136] K. Yokota, J. Takeda, C. Dang, G. Han, D. N. McCarthy, T. Nagao, S. Hishita, M. Kitajima, and I. Katayama, "Surface metallic states in ultrathin Bi(001) films studied with terahertz time-domain spectroscopy," *Appl. Phys. Lett.*, vol. 100, no. 25, p. 251605, Jun. 2012.
- [137] B. Ferguson and X.-C. Zhang, "Materials for terahertz science and technology," *Nat. Mater.*, vol. 1, no. 1, pp. 26–33, Sep. 2002.
- [138] P. Y. Yu and M. Cardona, *Fundamentals of Semiconductors: Physics And Materials Properties, Volume 3*. Springer Science & Business Media, p. 639, 2005.
- [139] K. Yatsugi, N. Matsumoto, T. Nagashima, and M. Hangyo, "Transport properties of free carriers in semiconductors studied by terahertz time-domain magneto-optical ellipsometry," *Appl. Phys. Lett.*, vol. 98, no. 21, p. 212108, May. 2011.
- [140] E. Bellotti and R. Paiella, "Numerical Simulation of ZnO-Based Terahertz Quantum Cascade Lasers," *J. Electron. Mater.*, vol. 39, no. 7, pp. 1097–1103, May. 2010.

- [141] J. Petzelt, P. Kužel, I. Rychetský, A. Pashkin, and T. Ostapchuk, “Dielectric Response of Soft Modes in Ferroelectric Thin Films,” *Ferroelectrics*, vol. 288, no. 1, pp. 169–185, Jan. 2003.
- [142] W. Z. Jianguang Han, Wei Chen, Jun Zhang, Mingxia He, Abul K. Azad, S. Ray, Y. Zhao, “Terahertz Response of Bulk and Nanostructured ZnO,” *PIERS Online*, vol. 4, no. 3, pp. 391–395, 2008.
- [143] J. B. Baxter and C. A. Schmuttenmaer, “Carrier dynamics in bulk ZnO. II. Transient photoconductivity measured by time-resolved terahertz spectroscopy,” *Phys. Rev. B*, vol. 80, no. 23, p. 235206, Dec. 2009.
- [144] Z. Mics, A. D’Angio, S. A. Jensen, M. Bonn, and D. Turchinovich, “Density-dependent electron scattering in photoexcited GaAs in strongly diffusive regime,” *Appl. Phys. Lett.*, vol. 102, no. 23, p. 231120, Jun. 2013.
- [145] B. K. Meyer, H. Alves, D. M. Hofmann, W. Kriegseis, D. Forster, F. Bertram, J. Christen, A. Hoffmann, M. Straßburg, M. Dworzak, U. Habocek, and A. V. Rodina, “Bound exciton and donor–acceptor pair recombinations in ZnO,” *Phys. status solidi*, vol. 241, no. 2, pp. 231–260, Feb. 2004.
- [146] W. Baer, “Faraday Rotation in ZnO: Determination of the Electron Effective Mass,” *Phys. Rev.*, vol. 154, no. 3, pp. 785–789, Feb. 1967.
- [147] J. Lloyd-Hughes and T.-I. Jeon, “A Review of the Terahertz Conductivity of Bulk and Nano-Materials,” *J. Infrared, Millimeter, Terahertz Waves*, vol. 33, no. 9, pp. 871–925, May 2012.
- [148] H. Němec, P. Kužel, and V. Sundström, “Charge transport in nanostructured materials for solar energy conversion studied by time-resolved terahertz spectroscopy,” *J. Photochem. Photobiol. A Chem.*, vol. 215, no. 2–3, pp. 123–139, Sep. 2010.
- [149] Y.-J. Zhu and F. Chen, “Microwave-assisted preparation of inorganic nanostructures in liquid phase,” *Chem. Rev.*, vol. 114, no. 12, pp. 6462–555, Jun. 2014.
- [150] M. J. Collins, “Chapter 1 Introduction to microwave Chemistry, Microwave Synthesis,” in *Chemistry at the Speed of light*, B. L. Hayes, Ed. CEM publishing, 2010.
- [151] M. J. Neas, E.D. , Collins, *Introduction to Microwave Sample Preparation: Theory and Practice*. American Chemical Society, pp. Ch.2,pp.7–32, 1988.
- [152] B. L. Hayes, *Microwave synthesis: chemistry at the speed of light*. CEM Pub., 2002.
- [153] M. Baghbanzadeh, L. Carbone, P. D. Cozzoli, and C. O. Kappe, “Microwave-assisted synthesis of colloidal inorganic nanocrystals,” *Angew. Chem. Int. Ed. Engl.*, vol. 50, no. 48, pp. 11312–59, Nov. 2011.

- [154] D. M. P. Mingos and D. R. Baghurst, "Tilden Lecture. Applications of microwave dielectric heating effects to synthetic problems in chemistry," *Chem. Soc. Rev.*, vol. 20, no. 1, p. 1, Jan. 1991.
- [155] C. Gabriel, S. Gabriel, E. H. Grant, B. S. J. Halstead, and D. Michael P. Mingos, "Dielectric parameters relevant to microwave dielectric heating," *Chem. Soc. Rev.*, vol. 27, no. 3, p. 213, 1998.
- [156] D. Q. M. Craig, *Dielectric Analysis of Pharmaceutical Systems*; London, UK: Taylor and Francis, 1995.
- [157] J. Jacob, L. H. L. Chia, and F. Y. C. Boey, "Thermal and non-thermal interaction of microwave radiation with materials," *J. Mater. Sci.*, vol. 30, no. 21, pp. 5321–5327, 1995.
- [158] J. M. Patete, X. Peng, C. Koenigsmann, Y. Xu, B. Karn, and S. S. Wong, "Viable methodologies for the synthesis of high-quality nanostructures," *Green Chem.*, vol. 13, no. 3, p. 482, Mar. 2011.
- [159] H. Katsuki, S. Furuta, and S. Komarneni, "Semi-continuous and fast synthesis of nanophase cubic BaTiO<sub>3</sub> using a single-mode home-built microwave reactor," *Mater. Lett.*, vol. 83, pp. 8–10, Sep. 2012.
- [160] I. Bilecka, P. Elser, and M. Niederberger, "Kinetic and thermodynamic aspects in the microwave-assisted synthesis of ZnO nanoparticles in benzyl alcohol.," *ACS Nano*, vol. 3, no. 2, pp. 467–77, Feb. 2009.
- [161] J. J. Richardson and F. F. Lange, "Rapid synthesis of epitaxial ZnO films from aqueous solution using microwave heating," *J. Mater. Chem.*, vol. 21, no. 6, p. 1859, Jan. 2011.
- [162] O. Akhavan, M. Mehrabian, K. Mirabbaszadeh, and R. Azimirad, "Hydrothermal synthesis of ZnO nanorod arrays for photocatalytic inactivation of bacteria," *J. Phys. D: Appl. Phys.*, vol. 42, no. 22, p. 225305, Nov. 2009.
- [163] G. Hodes, Chemical solution deposition of semiconductor films. Rehovot, Israel, pp. 12–14, 2002.
- [164] C. B. Tay, "Section 2.3 Temperature-dependent ionic equilibrium," in *Growth Of Zinc Oxide Nanostructures and Films and p-doping Of Films In Aqueous Solution*, 2009.
- [165] D. Andeen, J. H. Kim, F. F. Lange, G. K. L. Goh, and S. Tripathy, "Lateral Epitaxial Overgrowth of ZnO in Water at 90 °C," *Adv. Funct. Mater.*, vol. 16, no. 6, pp. 799–804, Apr. 2006.
- [166] J. P. Brunelle, "Preparation of catalysts by metallic complex adsorption on mineral oxides," *Pure Appl. Chem.*, vol. 50, no. 9–10, pp. 1211–1229, Jan. 1978.

- [167] C. B. Tay, S. J. Chua, and K. P. Loh, "Investigation of morphology and photoluminescence of hydrothermally grown ZnO nanorods on substrates pre-coated with ZnO nanoparticles," *J. Cryst. Growth*, vol. 311, no. 5, pp. 1278–1284, 2009.
- [168] W. Stumm, *Aquatic Surface Chemistry: Chemical Processes at the Particle-Water Interface*. John Wiley & Sons, p. 520, 1987.
- [169] C. B. Tay, S. J. Chua, and K. P. Loh, "Investigation of morphology and photoluminescence of hydrothermally grown ZnO nanorods on substrates pre-coated with ZnO nanoparticles," *J. Cryst. Growth*, vol. 311, no. 5, pp. 1278–1284, Feb. 2009.
- [170] S. J. Chua, C. B. Tay, J. Tang. "ZnO Nanostructures and Thin Films Grown in Aqueous Solution: Growth, Defects, and Doping" in *Handbook of Zinc Oxide and Related Materials*, vol. 1. C. F. Zhe, Ed. CRC Press, 2012.
- [171] C. B. Tay, H. Q. Le, S. J. Chua, and K. P. Loh, "Empirical Model for Density and Length Prediction of ZnO Nanorods on GaN Using Hydrothermal Synthesis," *J. Electrochem. Soc.*, vol. 154, no. 9, p. K45, Sep. 2007.
- [172] A. Wei, X. W. Sun, C. X. Xu, Z. L. Dong, Y. Yang, S. T. Tan, and W. Huang, "Growth mechanism of tubular ZnO formed in aqueous solution," *Nanotechnology*, vol. 17, no. 6, pp. 1740–1744, Mar. 2006.
- [173] P. Erhart and K. Albe, "First-principles study of migration mechanisms and diffusion of oxygen in zinc oxide," *Phys. Rev. B*, vol. 73, no. 11, 2006.
- [174] P. Erhart and K. Albe, "Diffusion of zinc vacancies and interstitials in zinc oxide," *Appl. Phys. Lett.*, vol. 88, no. 20, p. 201918, 2006.
- [175] S. Jiang, Z. Ren, S. Gong, S. Yin, Y. Yu, X. Li, G. Xu, G. Shen, and G. Han, "Tunable photoluminescence properties of well-aligned ZnO nanorod array by oxygen plasma post-treatment," *Appl. Surf. Sci.*, vol. 289, pp. 252–256, 2014.
- [176] P.-T. Hsieh, Y.-C. Chen, K.-S. Kao, and C.-M. Wang, "Luminescence mechanism of ZnO thin film investigated by XPS measurement," *Appl. Phys. A*, vol. 90, no. 2, pp. 317–321, 2008.
- [177] S. Bang, S. Lee, Y. Ko, J. Park, S. Shin, H. Seo, and H. Jeon, "Photocurrent detection of chemically tuned hierarchical ZnO nanostructures grown on seed layers formed by atomic layer deposition," *Nanoscale Res. Lett.*, vol. 7, no. 1, pp. 1–11, 2012.
- [178] A. Janotti and C. G. Van de Walle, "Native point defects in ZnO," *Phys. Rev. B*, vol. 76, no. 16, p. 165202, Oct. 2007.



- [179] D. Li, Y. H. Leung, A. B. Djurišić, Z. T. Liu, M. H. Xie, S. L. Shi, S. J. Xu, and W. K. Chan, “Different origins of visible luminescence in ZnO nanostructures fabricated by the chemical and evaporation methods,” *Appl. Phys. Lett.*, vol. 85, no. 9, pp. 1601–1603, 2004.
- [180] G. Irmer, “Raman scattering of nanoporous semiconductors,” *J. Raman Spectrosc.*, vol. 38, no. 6, pp. 634–646, Jun. 2007.
- [181] W. K. Bianca Schreder, Chapter 12 Raman Spectroscopy on II–VI Semiconductor in *Handbook of Raman Spectroscopy: From the Research Laboratory to the Process Line*. Taylor & Francis, 2001.
- [182] J. P. Brunelle, *Preparation of Catalysts II, Proceedings of the Second International Symposium*, vol. 3. Elsevier, pp. 211–232, 1979.
- [183] E.-C. Lee and K. J. Chang, “P-type doping with group-I elements and hydrogenation effect in ZnO,” *Phys. B Condens. Matter*, vol. 376–377, pp. 707–710, Apr. 2006.
- [184] P. Bénézech, D. A. Palmer, D. J. Wesolowski, and C. Xiao, “New Measurements of the Solubility of Zinc Oxide from 150 to 350°C,” *J. Solution Chem.*, vol. 31, no. 12, pp. 947–973, Dec. 2002.
- [185] E.-C. Lee and K. Chang, “Possible p-type doping with group-I elements in ZnO,” *Phys. Rev. B*, vol. 70, no. 11, p. 115210, Sep. 2004.
- [186] M. G. Wardle, J. P. Goss, and P. R. Briddon, “Theory of Li in ZnO: A limitation for Li-based p -type doping,” *Phys. Rev. B*, vol. 71, no. 15, p. 155205, Apr. 2005.
- [187] L. Tang, B. Wang, Y. Zhang, and Y. Gu, “Structural and electrical properties of Li-doped p-type ZnO thin films fabricated by RF magnetron sputtering,” *Mater. Sci. Eng. B*, vol. 176, no. 7, pp. 548–551, Apr. 2011.
- [188] J.-J. Lai, Y.-J. Lin, Y.-H. Chen, H.-C. Chang, C.-J. Liu, Y.-Y. Zou, Y.-T. Shih, and M.-C. Wang, “Effects of Na content on the luminescence behavior, conduction type, and crystal structure of Na-doped ZnO films,” *J. Appl. Phys.*, vol. 110, no. 1, p. 013704, Jul. 2011.
- [189] G. Irmer, “Raman scattering of nanoporous semiconductors,” *J. Raman Spectrosc.*, vol. 38, no. 6, pp. 634–646, Jun. 2007.
- [190] H. Morko and M. Zgr, Chapter 1. General Properties of ZnO in *Zinc Oxide*. Weinheim, Germany: Wiley-VCH Verlag GmbH & Co. KGaA, 2009.
- [191] C. H. Park, S. B. Zhang, and S.-H. Wei, “Origin of p-type doping difficulty in ZnO: The impurity perspective,” *Phys. Rev. B*, vol. 66, no. 7, p. 073202, Aug. 2002.
- [192] G.-Y. Huang, C.-Y. Wang, and J.-T. Wang, “First-principles study of diffusion of Li, Na, K and Ag in ZnO,” *J. Phys. Condens. Matter*, vol. 21, no. 34, p. 345802, Aug. 2009.

- [193] X. H. Huang, C. B. Tay, Z. Y. Zhan, C. Zhang, L. X. Zheng, T. Venkatesan, and S. J. Chua, "Universal photoluminescence evolution of solution-grown ZnO nanorods with annealing: important role of hydrogen donor," *CrystEngComm*, vol. 13, no. 23, p. 7032, Dec. 2011.
- [194] J. P. Jolivet, and M. Henry, and J. Livage, *Metal Oxide Chemistry and Synthesis: From Solution to Solid State*, John Wiley& Sons, ISBN 9780471970569, 1. Edition, August 2000.
- [195] A. Laufer, N. Volbers, S. Eisermann, K. Potzger, S. Geburt, C. Ronning, and B. K. Meyer, "Determination of secondary ion mass spectrometry relative sensitivity factors for polar and non-polar ZnO," *J. Appl. Phys.*, vol. 110, no. 9, p. 094906, Nov. 2011.

## Appendices

### List of Publication

#### Book Chapter

S. J. Chua, C. B. Tay, **J. Tang**, “ZnO nanostructures and thin films grown in aqueous solution: growth, defects and doping,” vol. 1, Chapter 5, *Handbook of Zinc Oxide and Related Materials*, CRC Press, 2013.

#### Journal Publications

1. **J. Tang**, L. Y. Deng, C. B. Tay, X. H. Zhang, J. W. Chai, H. Qin, H. W. Liu, T. Venkatesan, and S. J. Chua, “Determination of Carrier Concentration Dependent Electron Effective Mass and Scattering Time of n-ZnO Thin Film by Terahertz Time Domain Spectroscopy,” *J. Appl. Phys.*, vol. 115, no. 3, pp 033111, Jan. 2014.
2. **J. Tang**, J. W. Chai, J. Huang, L. Y. Deng, T. Venkatesan, C. B. Tay, S. J. Chua, “ZnO Nanorods with Low Intrinsic Defects and High Optical Performance Grown by Facile Microwave-Assisted Solution Method”. *ACS Appl. Mater. Interfaces*, vol. 7, no. 8, pp 4737–4743, Feb. 2015.
3. **J. Tang**, L. Y. Deng, I. P. Seetoh, K. K. Ansah-Antwi, P. Yang, T. Venkatesan, S. J. Chua, “Large Enhancement In Photoluminescence of ZnO Grown on Strain Relaxed Nanoporous GaN Template by Pulsed Laser Deposition”. (to be submitted)
4. C. B. Tay, **J. Tang**, X. S. Nguyen, X. H. Huang, J. W. Chai, V. T. Venkatesan, and S. J. Chua, “Low Temperature Aqueous Solution Route to Reliable p-Type Doping in ZnO with K: Growth Chemistry, Doping Mechanism, and Thermal Stability,” *J. Phys. Chem. C*, vol. 116, no. 45, pp. 24239–24247, Nov. 2012.

5. X. S. Nguyen, C. B. Tay, **J. Tang**, E. A. Fitzgerald, and S. J. Chua, "Fabrication of p-Type ZnO Nanorods/n-GaN Film Heterojunction Ultraviolet Light-Emitting Diodes By Aqueous Solution Method," *Phys. status solidi*, vol. 210, no. 8, pp. 1618–1623, Aug. 2013.
6. J. Huang, K. H. P. Tung, **J. Tang**, H. Liu, N. Xiang, A. J. Danner, and J. Teng, "Effect of SiO<sub>2</sub>–Metal–SiO<sub>2</sub> Plasmonic Structures on InGaAs/GaAs Quantum Well Intermixing," *Appl. Phys. A*, pp. 1–5, Aug. 2014.
7. L. Deng, J. Teng, H. Liu, Q. Y. Wu, **J. Tang**, X. Zhang, S. A. Maier, K. P. Lim, C. Y. Ngo, S. F. Yoon, and S. J. Chua, "Direct Optical Tuning of the Terahertz Plasmonic Response of InSb Subwavelength Gratings," *Adv. Opt. Mater.*, vol. 1, no. 2, pp. 128–132, Feb. 2013.

#### Conference (presentation and posters)

1. **J. Tang**, C. B. Tay, X. S. Nguyen, J. W. Chai, L. Ke and S. J. Chua, "Breaking the ZnO p-Doping Barrier with Low Temperature Aqueous Solution Chemistry". IMRE Postgraduate Students Poster Competition, Aug, 2011.  
→**Best Poster Award (1st Prize, Category A) with book prize**
2. C. B. Tay, X. S. Nguyen, **J. Tang**, X. H. Huang, T. Venkatesan and S. J. Chua, "Zinc Oxide: A Promising Material for Optoelectronic Applications". NUSNNI-Nanocore Workshop 2012, NUS, 19-20 November 2012.  
→**Best Poster Award**
3. **J. Tang**, L. Y. Deng, I. P. Seetoh, K. K. Ansah-Antwi, T. Venkatesan, S. J. Chua, "Large Enhancement in Photoluminescence of ZnO Grown on Strain Relaxed Nanoporous GaN Template by Pulsed Laser Deposition," Oral Presentation, paper No. KNOJ4, session J.VI, 10:30am, May 27, 2014, E-MRS 2014 Spring Meeting, Congress Center - Lille, France.  
→ **Awarded S\$1000 from Lee Foundation to attend E-MRS, Lille, France, 2014**

4. **J. Tang**, C. B. Tay, J. W. Chai, X. S. Nguyen, S. J. Chua, “Tailor Photoluminescence Wavelength by Controlling the Surface Stoichiometry of ZnO Nanorods Grown by Microwave Assisted and Traditional Water Bath Assisted Aqueous Solution Synthesis,” Oral Presentation, paper No. F3U5R, session I. IV, 17:15pm, May 26, 2014, E-MRS 2014 Spring Meeting, Congress Center - Lille, France.  
→**Shortlisted for graduate student award**
  
5. **J. Tang**, L. Y. Deng, J. Huang, S. J. Chua, T. Venkatesan, “Surface Plasmon Enhanced Photoluminescence of ZnO nanorods by 1D and 2D Metal Gratings,” paper No. L9.85, Hynes, Level 1, Hall B, Dec 5, 2013, MRS Fall Meeting, Boston, USA.
  
6. **J. Tang**, L. Y. Deng, J. W. Chai, C. B. Tay, X. H. Zhang, H. Qin, S. J. Chua, “Determination of Effective Mass from ZnO Thin Film by Terahertz Time Domain Spectroscopy,” paper No. Tu4-41, Kyoto Terrsa, April 02, 2013, International Workshop on Optical Terahertz Science and Technology (OTST 2013), Kyoto, Japan.  
→**Awarded S\$1000 from Lee Foundation to attend OTST 2013, Kyoto, Japan**
  
7. **J. Tang**, L. Y. Deng, C. B. Tay, X. S. Nguyen, X. H. Zhang, T. Venkatesan, S. J. Chua. “Investigation of Carrier Mobility and Conductivity of Potassium Doped p-type ZnO Thin Films by Terahertz Time Domain Spectroscopy,” paper No.FF4.11, Hynes, Level 2, Hall D, Nov 26, 2012, MRS Fall, Boston, U.S.A.